Towards integrated magneto-photonic devices for all-optical reading of non-volatile memories

THESIS

ter verkrijging van de graad van doctor aan de Technische Universiteit Eindhoven, op gezag van de rector magnificus prof.dr.ir. F.P.T. Baaijens,
voor een commissie aangewezen door het College voor Promoties, in het openbaar te verdedigen op donderdag 1 december 2022 om 16:00 uur

door

Figen Ece Demirer

geboren te Bartın, Turkiye

Dit proefschrift is goedgekeurd door de promotoren en de samenstelling van de promotiecommissie is als volgt:

voorzitter: prof.dr.ir. G.M.W. Kroesen

promotoren: prof.dr. B. Koopmans

                dr. J.J.G.M. van der Tol

copromotor: dr.ir. R. Lavrijsen

leden: prof.dr. A. Fiore

                prof.dr. A.I. Kirilyuk (Raboud University, The Netherlands)

                prof.dr.ir. S. van Dijken (Aalto University, Finland)

                prof.dr. B. Dagens (CNRS (C2N), France)

adviseur: dr. Y. Jiao

Het onderzoek of ontwerp dat in dit thesis wordt beschreven is uitgevoerd in overeenstemming met de TU/e Gedragscode Wetenschapsbeoefening.

Contents

Chapter 1

Introduction

The aim of this chapter is to provide the reader with a short motivation that lies at the basis of the work presented in this Thesis. The chapter starts with a general introduction, thereafter the fields of integrated photonics, spintronics, and magneto-optics are introduced. At the end of this chapter, an outline of the rest of this thesis is presented.

1.1   Background

Over the past decades, the field of electronics experienced immense miniaturization efforts for its components, mainly motivated by performance improvement needs [1]. Currently, the downsizing of components has reached such a level that the further shrinking is not favorable due to heat dissipation [2]. Often referred as the heat wall, the effect implies that the electronic circuitry simply gets too hot to perform operations [3]. An 'easy' fix to the over-heating circuitry problem is to continuously cool it down, which leads to a sizable energy consumption. To exemplify, in a conventional data center half of the total energy consumption is spent in cooling operations [4]. Furthermore, an ever-increasing number of devices is connected to the internet, i.e. the internet of things, is making the energy consumption considerations even more crucial. Reports indicate that the total energy footprint is expected to increase exponentially with time [5]. In 2020, amongst all the communication related activities, data centers dominated the electricity consumption with approximately 200 TWh [6]. This is a significant amount, corresponding to approximately 1 % of the total electricity consumption over the globe [7]. This problem requires attention from multiple disciplines with the common aim of delivering technological advancements for more energy-efficient computational operations. With the work presented in this thesis, we take a step towards improving the speed of memory operations by introducing on-chip optical reading of non-volatile magnetic memory components. When combined with parallel efforts on all-optical writing of magnetic information [8], the research is expected to lead to more energy efficient memory operations. The reason we focus on non-volatile memory is due to its intrinsic property of maintaining stored information without the need for constant feed of electric charge. This is highly valuable when the energy consumption and heating are considered. Prior to describing our work, let us depict the current situation including the recent advancements around this field.

A data center is a great example to depict the computational processes that involve non-volatile memory since the majority of operations include communications with e.g., hard drives. Depicting the current status and the recent advancements will allow us to spot areas that long for innovation. A computer in a data center frequently retrieves and delivers information to the non-volatile memory from its Central Processing Unit (CPU). These two areas are often realized in different chips and the conventional communication channel between them is an electrical 'bus'. Recently, products utilizing integrated photonic waveguides as buses in their computer architecture were shown to increase the speed of communication

[9]. This makes the overall system more energy-efficient by reducing the idle time that consumes energy. The handled data was carried into different parts of the electronic circuitry in the optical form, taking advantage of the optical communication speeds. In addition to the field of photonics, the field of spintronics is also providing solutions that increase the energy efficiency of such computational processes. To exemplify, recent advancements demonstrating novel phenomena [10] in multi-layered thin-film interfaces [11] are starting to be utilized as products for high-performance data-handling (read, write and transport) [12]. So far we have mentioned the improvements provided by the fields of photonics or spintronics alone. On top of that, at the intersection of the two fields, the interaction between light and magnetized matter is enabling higher speeds and increased energy efficiencies. To exemplify, there are engineered thin-film magnetic materials whose magnetization direction (thus the memory state) can be changed via ultrafast (femtosecond) laser pulses. This leads to faster memory writing processes [8, 13] what is referred in the literature as the All-Optical Switching (AOS) of the magnetization direction.
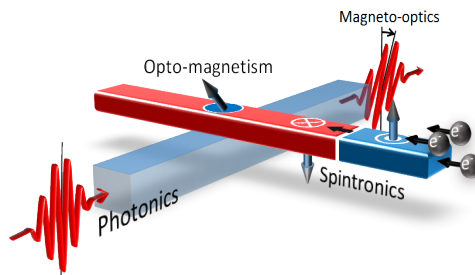
Figure 1.1: A schematic depicting the proposed magneto-photonic device that has all-optical reading and writing of magnetic memory. Figure by Bert Koopmans.

We position our work at the strategic cross-section of the integrated photonics and spintronics fields. The work utilizes the interaction between light and magnetized matter, more specifically the Magneto-Optical Kerr Effect (MOKE) to deliver the memory reading functionality. As depicted in Fig. 1.1, the dream is to combine all-optical magnetic memory writing with reading and deliver fast and energy efficient memory processes.

1.2 Integrated photonics

An integrated photonic circuit can be described as an analogue to an electronic circuit

where photons replace electrons as the information carriers [14]. Photonic waveguides connect optical components to one another and serve a similar functionality as the conductive printed connections in electronic circuits. Unlike the behavior of light in a free-space optics, in photonic circuits the light is bound to the medium, thus follow its boundaries when propagating (e.g. in sharp turns).

Let us take a look at the relatively brief history of integrated photonics. Demonstration of the world's first semiconductor laser in 1960s [15] inspired the concept of integrating optical components on a chip [16]. Today, the field of integrated photonics spans such a great range of applications that we all rely on this technology, e.g. for the high-speed internet we use. Despite the fact that it had been addressed for its faster data transmission and bandwidth capabilities in the early 1970s, the field progressed rather slowly until the mid-1980s [14]. It was the demonstration of superior performance (when compared with electronics) in long-distance data communication that gave the field its long-anticipated momentum [17, 18]. Presently, the photonic circuitry serves a broad range of applications. What was previously possible only by using an entire laboratory of optical components is now realized on a small area of a semiconductor wafer (known as a chip) in a photonic circuit setting. The applications are not only limited to fiber-optic communication, but include biomedical [19], agricultural [20], automotive [21], defense [22], aerospace [23] and quantum computing [24] fields. One specific use case is photonic interconnects. Such on-chip photonic structures replace the slow and heat-dissipating electronic current based connections (buses) in modern computer architectures. They serve as an optical communication channel between the spatially distanced chips that are fabricated in different material stacks such as the non-volatile memory chip and the CPU. It was shown that photonic interconnects decrease the memory latency tremendously and contribute to more energy-efficient computations [9, 25]. Adoption of the integrated photonic technology is rapidly increasing. This is thanks to the modular design possibility with on-demand added functionalities, as well as the reduction in production costs via Multi-Project Wafer (MPW) runs offered by multiple foundries. Figure 1.2 (a) depicts a component library with some optical components, the so-called building blocks. These blocks are readily optimized in terms of certain design parameters while some parameters are variable to be adjusted on-demand. The top-part of Fig. 1.2 (a) indicates that the cross-sections of the building blocks may differ from one another despite having been realized in the same material platform. The bottom part shows the 3-D appearances (artist's impressions) and the 2-D design masks. Typical building blocks include lasers, detectors, polarization converters, modulators and filters. Availability of a
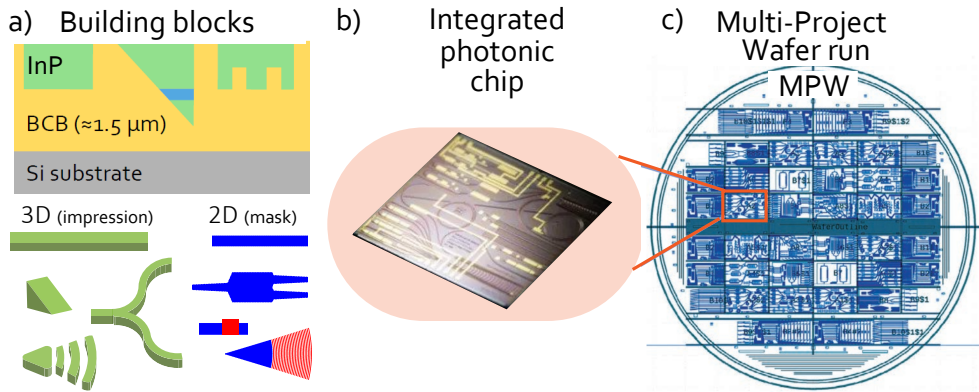
Figure 1.2: (a) Schematic depicting some of the optical components (building blocks) available in the IMOS fabrication platform. Cross-section views, as well as 3-D impressions and 2-D mask layouts are provided. (b) Image of an example integrated photonic cell. (c) Depiction of a full wafer for Multi-Project Wafer (MPW) run where each participant contributes to the cost of the cleanroom fabrication. Image retrieved from [26].

building block library allows users to compose circuits in a modular fashion for a desired functionality [27]. Figure 1.2 (b) shows a readily fabricated integrated photonic chip. This is a single cell from the overall wafer (MPW). Figure 1.2 (c) depicts a full-wafer design in a MPW run where each participant reserves a defined area (cell) on the full wafer surface. This feature enables smaller scale enterprises to access the integrated photonic circuit technology since it drastically decreases the production (e.g. prototype) costs. In the framework of this thesis, we submitted our dedicated designs and benefited from such a service.

For integrated photonics there are fabrication platforms with different substrate materials. The substrate material is of great importance since the design parameters and certain functionalities depend on it [28, 29]. To exemplify, silica-based integrated photonic platforms, such as silica on silicon, silicon on insulator (SOI) and silicon nitride (Si_3N_4), have comparatively low losses and thermal sensitivity; however, they cannot deliver lasing components due to Si being an indirect bandgap semiconductor. The InP-based platforms on the other hand can provide the so-called active components such as lasers and amplifiers [30] thanks to the direct bandgap of the InP material [31]. One of these platforms is the InP Membrane On Silicon (IMOS) platform, in which we base the photonic components utilized in this work [32]. As will be discussed further in Chapter 3, the platform is preferred due to the strong interaction of guided light with the cladding in a mambrane configuration and

due to the availability of polarization rotator components and the possibility of integration with electronic circuits.

Despite the large selection of building blocks and the application areas, there is room for improvement within the field of integrated photonics. One such area is the optical memory. Currently, there are optical memories based on phase-change [33] and liquid crystal materials [34], as well as optical cavities [35] and materials that have induced opacity/transparency [36]. All these optical memory alternatives are currently outperformed by their electronic counterparts, thus require a performance boost to stay competitive.

Zooming out and looking at the outlook of integrated photonic components, it is expected that novel physical phenomena, such as the ones that stem from the interaction between light and magnetized matter, will provide new functionalities and increase performance. There are currently available photonic components that use such interactions. To exemplify, time-reversal symmetry breaking introduced by the magneto-optical effects is used to deliver optical isolator [37] and circulator [38] functionalities. However, using magneto-optic effects in integrated photonics is not straightforward due to the birefringence problem which arises when the light is confined to a geometry (i.e. waveguides) [39]. This simply causes the guided light modes to acquire a phase difference relative to one another and causes (often undesirable) mode beating phenomena. A solution to this is to use a quasi phase matching method as demonstrated in earlier works [40, 41]. Another challenge is the magneto-optically active material of choice. When the Faraday effect is utilized (which occurs while propagating in a magneto-optically active medium), transparent and low propagation loss garnet materials are used as the magneto-optically active medium [42]. However, these crystalline materials often cannot be grown directly on top of the photonic waveguides due to a lattice mismatch [43] or the growth conditions should be engineered with strict temperature requirements considering the compatibility with the photonic waveguide material itself [44]. Therefore, garnet materials are often bonded/glued to the waveguides [45–47]. The material selection criteria changes for applications that utilize MOKE. Since the effect occurs upon reflection from a magneto-optically active medium, coatings/claddings that are not transparent are preferred. Up until now, the works that rely on MOKE for their functionalities used ferromagnetic thin-films [48, 49].

In this thesis, we use the mentioned often-hindering phenomena of mode beating to our advantage and utilize a magneto-optical phenomenon to deliver the novel functionality of optically-read integrated photonic memory. As will become clear later in the thesis, ultra thin-film multilayered ferromagnetic materials that were historically studied as optical

memory recording media are chosen as the magneto-optically active integrated photonic memory material.

1.3 Spintronics and non-volatile magnetic memory

The work presented in this thesis is based on the interaction between the waveguide-confined light and the non-volatile magnetic memory materials. The magnetic memory materials we utilize are extensively studied for magneto-optic recording media. Additionally, the recent developments in the field of spintronics are of great importance for the positioning of our work. Therefore, we dedicate this section to the introduction of the non-volatile magnetic memory concept and the field of spintronics.

Magnetism has its roots in the magnetic dipole moment created by electron spins. A material is considered magnetic when its response to an externally applied magnetic field is significantly different than that of the free space [50] [51]. Ferromagnetic materials respond to an externally applied field by orienting their unpaired electron spins in this direction. Additionally, ferromagnetic materials have a net magnetic moment, despite the absence of an applied magnetic field. Ferromagnets that retain magnetization orientation for significant amount of time (>10 years) can be utilized as non-volatile memory materials [52].

The field of spintronics is defined on the basis of providing device functionality using the spin property of electrons. Despite the fact that the magneto-optic memory recording technology has been using the magnetization (spin) orientation of materials to deliver functionality since 1965 [53], it was the discovery of the Giant Magneto-Resistance (GMR) effect in 1988 that marked the beginning of the field of spintronics [54, 55]. The GMR effect showed that the electrical resistance between the two magnetic layers separated by a non-magnetic (conductive) layer changes drastically when the mutual magnetization orientation of the two changes. Using the GMR effect, the magnetic sensor sensitivity in hard disk drive read heads was improved drastically. Combined with the advancements in nanofabrication techniques, the motivation of increasing performance via miniaturization had led to the realization of smaller bit-sized memory components, increasing the density of memory storage. Currently, the state-of-the-art spintronic memory products include the Magneto-resistive Random Access Memory (MRAM) [56] and the racetrack memory [57]. While MRAM is a technologically matured concept, Racetrack memory is still in its infancy.

In this thesis, the racetrack memory is of particular interest since it enables the suggested device functionalities that will be described in Chapters 5 and 6. A schematic rep-
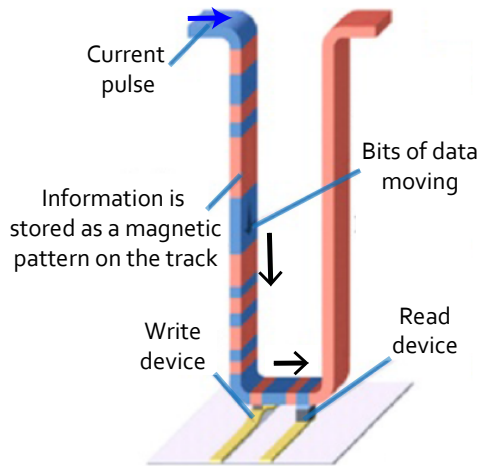
Figure 1.3: A schematic depicting the racetrack memory concept. Magnetic domains that indicate the memory type is shown with red and blue areas (bits '0' and '1'). By running a current through the wire (racing road), the memory bits (magnetic domains) are transported without physically moving parts. Sections where reading and writing take place are indicated. The figure is adapted from [57].

resentation of it is shown in Fig. 1.3, where the memory information (often referred to as the bits '1' and '0') are stored in the form of magnetic domains with opposite magnetization directions (red and blue). As the name racetrack is a metaphor for a racing road, the magnetic domains can be seen as racing cars that move over the road. When a spin current is injected into the racetrack with application of an electrical current, the domains move due to the force exerted on their domain walls [58]. Note that this is a simplification and there are aspects such as the domain wall type that are decisive for this motion [59]. Recent advancements in the racetrack memory material systems show domain wall velocities up to 2000 m/s [60]. Since the domain wall velocity correlates directly with the transfer rate of memory bits, a higher velocity is desired. As an example, for 50 nm bits, 2000 m/s would correspond to 40 Gbits/s. It is important to stress that the racetrack memory is a maturing technology with aspects of improvement requirements. Thus, there is ongoing research aimed towards its commercial success.

As described earlier in this chapter, energy efficiency of the circuitry is a crucial point awaiting improvement. In the frame of this thesis, data centers and their electricity consumption are of particular interest since many operations in data centers include communi-

cation with non-volatile memory components [61]. Therefore, an analysis of the processes that contribute to the heat dissipation is presented briefly. The focus is on the non-volatile memory components, hence, its relation to this work. In electronic circuitry, certain components require periodically (also referred as the computational cycle) supplied electric charge in order to function. Within each cycle, the supplied charge is released into the surroundings due to leakage, contributing to the heating. One might suggest that the non-volatile memory components do not take a major part in the dissipated heat since they don't need to be supplied with electric charge to retain their memory. However, the performance of the non-volatile memory components contributes to the dissipation thus the overall energy consumption in the following ways. First, since the non-volatile memory is fabricated on a different material stack, thus positioned on a different chip than that of the CPU, there exists the problem called the memory latency. This delay in the retrieval of memory causes significant heat dissipation. To describe it briefly, communication of information from non-volatile memory to CPU is conventionally mediated by electrical connections (buses). This transfer is the slowest step in all operations (i.e. Von Neumann bottleneck [62]). While the retrieval is ongoing, all other computational operations are put on hold, wasting computational cycles thus power. Second, to prevent the memory latency problem of the non-volatile memory (realized on a different chip than the CPU), the computer architecture is pushed towards accommodating volatile memory types that have faster memory retrieval (i.e. can be placed on the same chip as the CPU) but need constant supply of charge to retain memory: volatile memory alternatives (e.g. cache). Additionally, the relatively high cost of realization of non-volatile memory leads to a scenario that favors the use of volatile memory components, consequently increasing the heat dissipation.

In the light of the presented insights, the following properties of non-volatile memory components are desired.

- Faster retrieval and minimized memory latency

- Lower energy requirements for read/write operations

- Lower fabrication costs

The field of spintronics and non-volatile memory technologies are readily exploring novel methods to improve the above-mentioned points. Fruitful results come at the intersection of fields. One such example is the use of integrated photonics as vectors for sending and retrieving information from the spintronic memory. It already has been realized as a commercial product [63]. In this product, when the on-chip photonic interconnects replace the

conventional electrical buses, a faster and more energy efficient retrieval of information from the non-volatile memory is provided [9, 25]. Albeit this example brings together the two fields of spintronics and photonics, the boundaries of each field is still clear-cut without merging between the two. In this thesis we utilize the magneto-optical phenomenon and merge the fields of photonics and spintronics, providing novel functionalities with a great potential to increase energy efficiency.

1.4   Magneto-Optics

The term magneto-optics broadly refers to the interaction between light and magnetized matter. The first ever reported magneto-optic phenomenon was the Faraday effect in 1846 by Michael Faraday [64]. It was shown that the polarization plane of a linearly polarized light propagating in a transparent magnetized medium rotates by an angle (defined as the Faraday rotation), which is linearly proportional to both the magnetic field strength and the length of propagation. This was the first experimental evidence indicating the presence of a relationship between light and electromagnetism, prior to being laid out by Maxwell's equations in 1864 [65]. Nearly thirty years after the discovery of the Faraday effect, John Kerr reported the MOKE in 1877, showing that a linearly polarized light reflecting off a perpendicularly magnetized surface obtains rotation and ellipticity in its polarization state [66]. The Kerr rotation and ellipticity are intrinsically small in amplitude, which is the most probable reason behind its three decades late detection with respect to the Faraday effect. Followingly, two other effects of magneto-optical origin, namely the Cotton–Mouton [67] and the Voigt [68] effects were discovered. At the origin of all magneto-optical effects lays a symmetry breaking in optical transitions that can be mediated by light with right and left handedness. In materials with net magnetization, the exchange interaction and the spin–orbit interaction [69, 70] cause the energy levels to split in such a way that they are shifted differently for up- and downward directed spins. Macroscopically, this leads to a difference in polarizability when right- and left-handed circularly polarized light is used. Since the MOKE plays a major role in the frame of this thesis, we describe its microscopic origins, as well as its macroscopic observations and mathematical formulation in Sect. 3.1.

Historically, technological products based on the magneto-optical phenomena started to emerge after the demonstration of a magnetization compensation temperature in ferrimagnets in 1960 [71]. The concept of a thin-film magneto-optic memory was suggested for the first time in 1965 [53]. Later, the use of multi-layered films with a metallic core

sandwiched between dielectric layers [72] followed in 1967. The golden age of magneto-optic recording media was marked by the use of ferromagnetic Co/Pt multilayered thin-films in 1990s [73]. Following the rapid advancements in the field of integrated photonics, the magneto-optic phenomena have been referred to for providing novel on-chip photonic functionalities [48, 74–77]. In this work, we focused on the optical magnetic memory reading functionality in integrated photonic circuits using the MOKE. Therefore, we dedicated the following chapter to describe the state-of-the-art at the intersection of the two fields of photonics and magnetism.

1.5   This thesis

In this thesis, we explored the fruitful area at the intersection of the fields of spintronics and photonics. Chapters that make up this thesis is given below as bullet points.

- A state-of-the-art in relevant fields is given in Chapter 2.

- The fabrication techniques, characterization and measurement methods that are used throughout this thesis are discussed in Chapter 3. Additionally, optical design aspects and mathematical models are presented.

- Chapter 4 describes the research performed to investigate the enhanced magneto-optic activity at the interfaces of multi-layered Co/Pt thin-films and to quantify it in terms of a magneto-optic constant. For this, samples with continuous thickness variations are analyzed with a magneto-optical characterization technique. A mathematical model that accounts for (magneto-) optical effects in multi-layered thin films is used. As shown later in the thesis, the determined constants are shown to be effective in predicting experimental observations when used in optical simulations as inputs.

- Using the studied multi-layers as a non-volatile memory element on integrated photonic devices, Chapter 5 investigates an integrated photonic device design that allows the optical read out of the magnetic memory. Here, the results of optical simulations and mathematical models are presented.

- Chapter 6 is focused on a robust magneto-photonic device design. Combining the polarization manipulation via the MOKE and the propagation in an asymmetrical cross-section waveguide, experimental results are shown to follow the predictions of both

the mathematical models and the optical simulations. Accurate quantitative determination of the MOKE that takes place in a confined volume measured in the order of nanometers provides insights on the capabilities of the presented integrated magneto-photonic devices.

- Lastly, Chapter 7 gives a brief outlook on the possible routes the future research can take.

Chapter 2

State of the art

The work presented in this thesis is performed at the cross-section of two fields, namely spintronics and integrated photonics. The aim of this chapter is to provide the reader with a state-of-the-art in these fields, to put the presented work into context. The chapter starts by describing the types of computer memory in an effort to map the characteristics, strengths and shortcomings of each memory type.

2.1 Computer memory hierarchy

Currently types of computer memory span a broad range where each type emerged due to different needs. These types differ in terms of read/write and access/retrieval speed, volatility and non-volatility features, energy consumption during operation and in idle state. Physical locations where these types reside are also different and this is of importance due to direct impact on the access/retrieval speeds, cost and complexity of the overall chip fabrication process and the total amount of memory capacity.
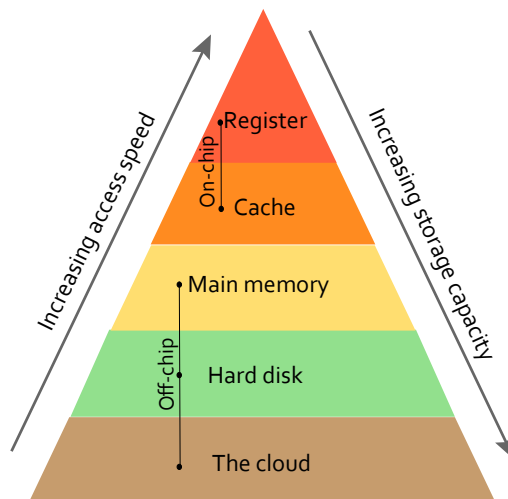
Figure 2.1: A schematic of the so-called memory pyramid which depicts the memory hierarchy in conventional computers. Memory retrieval is faster at the top of the pyramid whereas memory latency increases towards the bottom. Memory types located on the same chip as the central processing unit are marked as on-chip while the rest are off-chip. Mainly due to the physical storage location, the total storage increases towards the bottom of the pyramid. Schematic inspired by [78].

Different memory types are often visualized using a pyramid shape where the bottom layers refer to the low speed (high-latency), low energy consumption types that lie further away from the CPU, while the top layers are reserved for faster operating types that typically have higher power consumptions and lie in the close proximity of the CPU. The pyramid also implies that the total amount of stored information per memory type increases towards the bottom layers. This is partly due to the available space near the CPU. One

such memory pyramid is depicted in Fig. 2.1. Here, the bottom layers are reserved for hard disk and the cloud types that both accommodate further away from the CPU. Note that the memory pyramid is a simplistic way of describing and is valid for conventional computer memory types, thus it becomes inadequate to place the emerging, state-of-the-art memory types on a map. For more detailed comparisons between the conventional and the newer memory types about various performance parameters, we refer to the review paper by Barla *et al*. (Table 1 in [79]).

From a fundamental 'principles of operation' point of view, the computer memory can be categorized into two. The first is the CMOS electronic memory type which uses the charge property of electrons while the second is the spintronic memory and flash memory types which use both the spin and the charge property of electrons. While CMOS electronic memory types are fast and have higher retrieval speeds due to their location on electronic chips, they suffer from leakage current and require constant feeding with electric charge, thus consume more energy [3]. The non-volatile nature of the spintronic and flash memory types allows for retention of information indefinitely, cutting the costs in energy supply. The caveat for flash memory is the limited endurance [80]. Thanks to its low energy consumption and high endurance, a high potential is anticipated for spintronic memories in the fields of burgeoning big data, AI and information and communication technologies (ICT) [81, 82]. What was previously a disadvantage for the spintronic memory types is the write-speed. With new mechanisms such as spin transfer torque (STT) or spin-orbit torque (SOT), spintronics based random access memories are becoming more competitive [79]. There are ongoing challenges that prevents the use of spintronic memories for certain applications. One is the long memory retrieval times known as the memory latency [62]. Current advancements including integration with photonic waveguides [9] work towards elimination of this memory bottleneck by improving retrieval speed. Research is ongoing in the fields of spintronic memories to achieve faster and more energy efficient operations. Since the work presented in this thesis paves the way towards a spintronic memory combined with integrated photonics, the following section dives deeper into the state-of-the-art spintronic memory types.

2.2 Spintronic memory

Spintronic memories utilize the spin degree of freedom of electrons unlike CMOS electronic memory types that solely rely on the charge property of electrons to deliver func-

tionality. Research in this field is directed towards delivering more energy-efficient and faster memory operations while taking the accuracy and life-time aspects into consideration. Certain magnetic materials can maintain alignment of their spins despite the absence of an externally applied magnetic field. This feature is used to deliver non-volatile memory functionality which brings about low static energy dissipation and overall energy efficient devices [83].
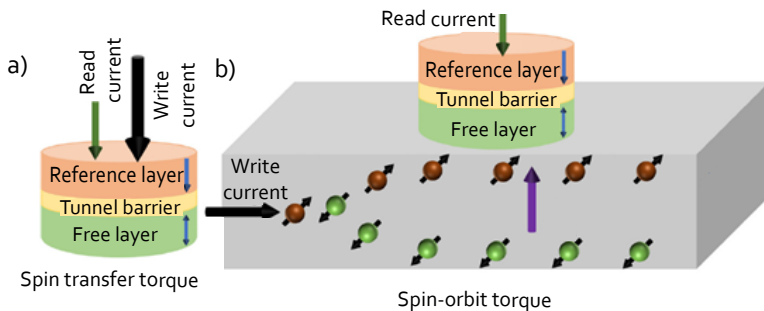
Figure 2.2: Schematic depicting the read and write mechanisms of (a) Spin transfer torque (STT) and (b) Spin-orbit torque (SOT) in Magnetic Tunnel Junctions (MTJ's). The figure is modified from [84].

Currently, the cutting-edge spintronic devices include MRAM based on Magnetic Tunnel Junctions (MTJ), domain wall motion-based racetrack memory and skyrmion-based memories. Since it plays an important role in this work, we highlighted the racetrack memory in Section 1.3. It should be noted that, amongst the mentioned memory technologies, only MRAM is in the stage of commercial availability while others are still being developed. In this regard, MRAM stands out as the most matured technology, delivering competitive performance parameters. A typical MTJ is made of ferromagnetic thin-film layers separated by a thin-film oxide layer [85]. Note that the material of ultra-thin ferromagnetic layers is used in other spintronic memories as well. Therefore, any advancement in materials science aspect of MRAM is of importance for the overall field of spintronics. MRAM technology is advantageous since its fabrication is well integrated into CMOS processing steps. The earlier versions of MRAM used in-plane magnetized thin films that were written via the Oersted fields generated by the currents passing through the addressing wires [81, 86]. The newer versions exploit out of-plane (OOP) magnetized materials since it allows for faster, more energy-efficient, and scalable read/write operations such as the spin-transfer torques (STT) and spin–orbit torques (SOT) [10, 81, 87–90]. To briefly sketch the STT and SOT, in both

mechanisms, the writing of memory is done by using the current of electrons as depicted in Fig. 2.2. Figure 2.2 (a) shows the STT where a transfer of spin angular momentum occurs between two magnetized layers across the tunnel barrier [13, 89]. Figure 2.2 (b) depict the SOT. The following phenomena of interaction of spin–orbit coupling, magnetic exchange, and symmetry breaking at the interface [13, 91] are utilized as the functioning mechanism, in addition to the flow of spin currents from the non-magnetic metal to the magnetic layer [92, 93]. In STT-MRAM devices, switching time (switching of the magnetization direction) ranges from a few nanoseconds (ns) to tens of ns depending on the write current density and pulse width. A reliable switching with write error rate less than 10^{-6} was shown with 2–3 ns switching time [94], which indicates prospect use as the last-level, on-chip cache memories [95, 96] that can be thought of as the top levels of the memory pyramid. The state-of-the-art SOT-MRAM devices are faster than the STT-MRAM, delivering sub-ns to few ns switching times [97–100] which in certain cases [93, 101, 102] are better in terms of energy-efficiency. For further details on the writing energies and times, we refer the interested reader to review articles [79, 84].

In the scientific agenda of the spintronic memory research, there are major points such as improving performance and energy efficiency while decreasing productions costs. Currently, spintronic memories deliver faster writing speed than flash memory alternatives however are slower compared to the CMOS electronic memories. This speed refers to the time it takes to change the magnetization orientation direction in a magnetic domain, and it is limited to the precessional dynamics at thermal equilibrium of ferromagnetic materials. Recent studies showed ultra-short light pulses allow for fast magnetization direction switching, increasing the writing speed of spintronic memories.

2.2.1 Spintronic memory and light

As hinted at in the previous section, spintronic memory technology benefits from ultra-short, all-optical switching mechanism using ultra-fast light pulses. Due to its ultrafast time frame, the field is referred as "femto-magnetism". The first observation within the field was made in 1996 when Beaurepaire *et al*. [103] showed that a sub-ps magnetization quenching in Ni thin-films is possible upon irradiation with ultrafast laser pulses. Scientific interest to the field grew over time due to its potential to drastically improve the writing speed of spintronic memories. The mechanisms behind this ultrafast switching (of magnetization direction), on the other hand, are still topics of scientific discussions. When Stanciu *et al*.[104]

first reported the all-optical control of magnetic orientation in amorphous ferrimagnets using circularly polarized femto-second laser pulses, the team attributed the magnetization switch to the inverse Faraday effect (IFE) [8, 105, 106]. Later, it was shown that the same material can be switched using a linearly polarized light, attributing the switch to purely thermal effects the pulse has on the media [107, 108]. Currently, the helicity dependent switching is attributed to the magnetic circular dichroism (MCD) in combination with reaching a threshold temperature where the light pulse gets absorbed differently by the memory medium depending on the polarity and orientation of the magnetization [109].
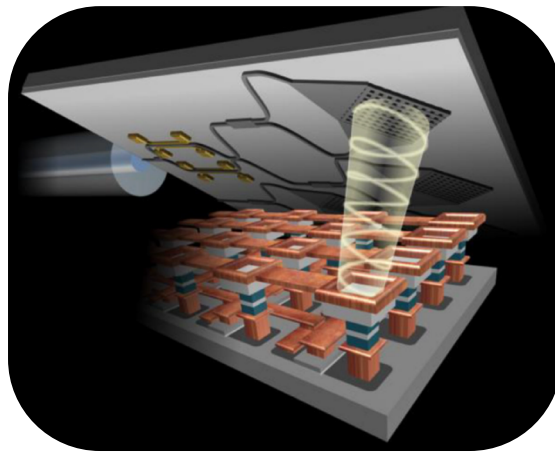
Figure 2.3: A schematic describing a photonic circuit (top-part) integrated with an electronic memory chip (bottom-part). Direct coupling-out of the guided light onto a Multi-Tunnel Junction (MTJ) memory element is shown. This design proposed by the EU SPICE network is adopted from [110].

The research efforts in the field of femto-magnetism are taking two distinct directions. One is to discover the potential spintronic memory applications that outperform other techniques due to fast and energy efficient magnetization switching, thus writing of information. The other is to use the ultrafast actions as a scientific tool to probe the spin dynamics at femto-second time scales [111, 112]. In the first category of efforts regarding the technological use of this mechanism, researchers investigate using all-optical magnetization reversal to write MTJ-based spintronic memory [110, 113]. As depicted in Fig. 2.3 adapted from [110], the European ultrafast spintronics network SPICE [114] proposed that when integrated photonic circuitry is embedded with electronics, normally material-confined light

can be used for all-optical writing of magnetic memory. The drawing shows light that is in photonic waveguides being locally extracted with help of grating couplers onto a MTJ memory elements. When combined with to the work presented in this thesis, the proposed scheme of all-optical writing of magnetic memory via integrated photonics is expected to deliver the spintronic memory products of the future.

2.3 Integrated photonics

As introduced briefly in Chapter 1, integrated photonic circuitry brings value to a variety of fields including biomedical [19], agricultural [20], automotive [21], defense [22], aerospace [23] and quantum computing [24]. Depending on the desired functionalities of each field, a photonic circuit can be composed using passive (e.g. couplers, switches, modulators, multiplexers) and active components (e.g. amplifiers, detectors, and lasers). Note that the active components require the use of direct bandgap semiconductors (III-V). Different platforms co-exist for integrated photonic circuit fabrication. Some platforms offer direct bandgap semiconductors, thus include active components in their library. Evidently, the material system is also decisive on the design and the footprint in addition to the performance and the functionality of its components. For a summary of different material platforms, the components they deliver and certain performance parameters, we refer to the Jeppix roadmap 2021-2025 [115]. Amongst different platforms, we introduce the Si and InP membrane-based ones briefly here. The choice is due to Si photonics being one of the most widely adopted platform while the latter enables the use of active components and offer easy integration with electronic circuits.

2.3.1 Si photonics

Currently, silicon photonics is the most widely adopted material platform for integrated photonic research. This is partly due to its compatibility with the mature Complementary Metal-Oxide-Semiconductor (CMOS) technology [116], and partly due to the record low losses [117] that are demonstrated within the platform. To exemplify, typical losses are between 0.1 dB/cm to 1 dB/cm [118] in silicon-based waveguides. One major set-back of the platform is that the silicon is an indirect bandgap semiconductor. To mitigate this, additional processing steps that introduce direct bandgap semiconductors are implemented during fabrication. For further details on the three methods of implementing active materi-

als in photonic circuitry, namely heterogeneous, hybrid and monolithical implementations, we refer the reader to [119]. While photodetectors [120] and modulators [121] can be realized by monolithical implementation of Ge (germanium) layers, semiconductor optical amplifiers and lasers require heterogeneous or hybrid methods [122, 123]. Until today, several techniques including transfer printing, flip-chip bonding and direct wafer bonding are successfully demonstrated [118, 119, 124].

2.3.2   Indium phosphide membrane photonics

As the platform utilized in this work, Indium phosphide membrane photonics deserves a dedicated section. The main strength of this platform is its ability to deliver laser and amplifier components, yielding fully functional and intact photonic integrated circuits. The membrane causes enhanced optical confinement which leads to compact (small footprint) devices. Additionally, it can easily be integrated with electronic chips because the membrane bonding technology does not cause disruption in the conventional CMOS processing steps. Despite the mentioned advantages of having a thin membrane, it comes at the cost of harder-to-control optical losses. An overview of the available active components and the state-of-the-art performance details can be found in [125, 126].

The components utilized in this work are purely passive. Let us provide some details on them. InP-family of membrane waveguides can be made out of InP [127], InGaAsP [128] or InGaP [129]. Single mode waveguides (with only one mode per polarization direction i.e., TE and TM) typically have 400–600 nm width and 150–300 nm height [125]. These parameters are chosen such that the single mode condition is fulfilled while assuring a low optical loss. As documented in a review paper [125], depending on the core material and the lithography processes, obtained propagation losses for the waveguides range from more than 10 dB/cm to under 2 dB/cm. The record low propagation loss of 1.8 dB/cm is on the IMOS platform [130], which is the platform of choice in this thesis. This is comparable to a typical loss value in fully etched SOI waveguides [131]. What causes propagation loss is the surface roughness of the guiding medium with respect to its surroundings. Since the top surfaces of the waveguides are defined with wet-etching utilizing the crystallographic orientation of the InP membrane, they are smooth and contribute very little to the optical losses. It is mostly the side-wall roughness that contributes to the propagation loss. To overcome side-wall roughness, several methods including using improved EBL resist [127, 132] or switching to DUV lithography [130] were demonstrated. As a disadvantage of the direct band gap of

InP, these waveguides demonstrate the undesirable two-photon absorption at elevated optical inputs [126]. Another passive component is a multi-mode interferometers (MMI) which serve as splitters. Novel design layouts of MMI that reduce detrimental back-reflections (> 10 dB reduction of the back-reflections) are used in InP [133] and IMOS platforms [134]. Additionally, passive components of polarization-selective grating couplers are common components in the IMOS platform. An improved version of regular grating coupler is the focused grating couplers with smaller footprint. This was initially demonstrated in SOI platforms [135, 136] with insertion losses of 5-8 dB. Lastly, polarization converters can also be found in the IMOS platform as passive components. Previously, examples of it that were based on mode-evolution, which typically occurs while propagating in an asymmetrical waveguide, were demonstrated in InP-based platforms [137–141]. A partial polarization converter that played a major role in this work was adapted from the work of Reniers *et al.* [141].

2.4   Optical memory

As previously highlighted, transfer of information over long distances is realized in the optical domain due to its fast speed. Despite the transfer of information is fast in the optical domain, there needs to be conversion steps from electronics to optics and vice-versa for implementing optics-based solutions to electronics. As a result, in the field of computer memory, conventional electronic components that function in the electrical domain are preferred over their optical counterparts due to speed and overall energy efficiency considerations. Advancing the field of optical memory in terms of speed, storage density and energy efficiency offers to unlock tremendous benefits. IBM stresses that using optical memory integrated into the photonic circuitry in a photonic circuit computation setting is an attractive solution to the current speed bottlenecks [142]. However, the relatively poor performance parameters of currently available optical memories are obstacles on the way to achieve efficient optical computation. Better-performing optical memories are expected to unlock faster operations and decreased energy consumption [143]. Furthermore, the potential of all-optical writing of the next-generation photonic memory devices is projected to deliver ultra-fast and energy efficient operations [144]. In this regard, the current work aims to contribute to an optical memory technology by incorporating the optical read-out functionality.

In the path to achieve the desired photonic performance parameters, let us take a brief look at the historical development of optical memory components and its state-of-the-art.

Early attempts of optical memories date back to 1997 when pulses in recirculated optical fiber loops served as the reservoir of information [145, 146]. The system was bulky, additionally the memory needed to be replenished every few hours, yielding relatively short retention times. Since then, there have been various optical memories proposed that rely on the fact that two distinct optical outputs can be encoded to store information. Among them, there are materials with induced opacity/transparency [36], liquid crystal materials [34], optical cavities and resonators [35, 147–150] in addition to injection-locking and switching between bistable laser modes [151–154]. Since they require continuous energy input to hold their memory state, they can be classified and utilized as volatile memories. To compete with electrical circuit analogues in terms of power consumption and speed, non-volatile alternatives with potentially energy efficient operations are sought after. There are a few non-volatile optical memory alternatives such as utilizing the novel property of formation/annihilation of nanoscale silver filaments inside a waveguide [155] and charge trapping inside a ring resonator [156]. However, the most well-established optical non-volatile memory is based on the phase-change materials whose atomic structure can be altered by heating [157] or other excitation process [158–161]. This change leads to a substantial change in the electrical and optical properties of these materials and allows to set the two distinct memory states [162]. There are some challenges that prevent the broader use of phase change material-based optical memories. Despite write energies at a pico-joules level can be achieved, it does not yet achieve the high sensitivity required for a reliable multibit operation since it requires a higher signal-to-noise ratio, thus higher power [163]. Additionally, the memory footprint is relatively large, preventing a high storage density.

2.5 Magneto-optics and integrated photonics

As briefly introduced in Section 1.4, magneto-optic phenomena take place when light and magnetized matter interacts. Since the work presented in this thesis is positioned at the intersection of magneto-optics and integrated photonics, we dedicated this section to mention previous works that contributed to this area. Additionally, we introduce how the previous work has set the stage for photonic waveguides with ferromagnetic claddings for memory reading functionality.

Actually, magneto-optic phenomena have found very little use within the field of integrated photonics. As to date, its use is mainly limited to integrated optical isolators. An optical isolator is a component commonly used together with a laser. It permits the light prop-

28

agation in one direction while preventing it for the other. This way, the degradation-causing back-reflections into the laser is prevented. Historically, optical isolators were realized in free-space and were made of magneto-optically active transparent media. They were used in a strong magnetic field environment and functioned thanks to the non-reciprocal phase shift that the Faraday effect causes [69]. A phase shift of $90°$ ($2\times45°$) of reflected waves enabled their elimination with orthogonally placed polarizer elements. After integration of lasers into photonic chips became mainstream and the field of integrated photonics was born, various integrated optical isolator analogues were suggested. Amongst these optical isolator designs, only some utilized the magneto-optic effect to deliver the isolation functionality [48, 164, 165]. Others functioned via non-reciprocity causing phenomena that are not of the magneto-optical origin [166–168]. Despite most of the works demonstrating optical isolators utilizing magneto-optic effects were using garnet materials, some utilized ferromagnetic metal claddings on their photonic waveguides [48, 165]. In these studies, the magnetization direction of the claddings were in-plane, perpendicular to the direction of light propagation. The resulting transverse MOKE was used as the mechanism of isolation. Both studies highlighted that within the waveguide, a quasi-phase matching condition is required to obtain an additive MOKE. For this, they suggested the use of claddings with alternating magnetization directions. This was very relevant for the work presented in this thesis, and it was studied by members of our research group in the form of optical simulations [41]. In this work we explored a configuration with out-of-plane magnetized claddings which has not been utilized before despite the advantages of an increased MOKE in this polar MOKE setting.

Chapter 3

Methodology

This chapter describes the methodology that was used to achieve the presented results in this thesis. We divide the chapter into five subsections, each describing different aspects of the methodology. Since the MOKE is used extensively throughout this thesis, we start by presenting the background on this effect, painting a microscopic and macroscopic picture of it. In the second section, we define the measurement set-up that allowed us to detect and quantify the MOKE. Since the magnetized samples used in this work are all multi-layered thin-films, we stress the MOKE that occurs in this configuration. We continue the chapter with its third section by describing the photonic design and elaborating on the design toolbox including the optical simulation tools. Then we describe the special configuration of the MOKE in waveguides and give an overall summary of the design process. On the fourth section, we describe the fabrication techniques that allowed us to realize the magneto-photonic devices. Lastly, in the fifth section, the measurement set-up used for magneto-photonic device characterization is elaborated.

3.1 Background on MOKE

The MOKE occurs upon the interaction between light and magnetized matter. It takes a central role in the frame of this thesis, since it enables reading of the magnetically stored memory. In this section, we first describe the microscopic origins of MOKE by zooming in to the optically induced electronic transitions and explain the mechanisms behind this effect. Then, we zoom out to list the macroscopic observations of the effect and represent it mathematically.

3.1.1 Microscopic origin of MOKE

Optical techniques are often used to probe the electronic band structures in materials due to the photons ability to mediate electronic transitions [169]. Probing the spin orientations (magnetism) of electrons via an optical technique however, is only possible due to the phenomenon called spin-orbit coupling [170]. In a typical ferromagnet, thanks to the coupling between the spin and the orbital motion, electronic transitions become sensitive to the magnetization direction of the material. This way, the MOKE spectroscopy indirectly probes the magnetization in materials. This is depicted in Fig. 3.1 via the relative energy level splittings of the spin-down and spin-up electrons (p and d orbitals) in a ferromagnet. The levels are split due to the spin-orbit coupling (≈ 0.05 eV [51]) and the exchange interaction (≈ 1 eV [51]). The spin-orbit coupling is formulated as

$$E_{SO}(\rho) = \xi(r) S L, \tag{3.1}$$

where $\xi(r)$ is the material specific spin-orbit coupling constant; and S and L are the spin and the orbital numbers, respectively. Since the S in Eqn. 3.1 is +1 and -1 for the spin-down and the spin-up electrons, the energy splitting occurs by opposite signs as indicated in the figure. The selection rules [171] indicate that the light with Left and Right Circular Polarizations (LCP and RCP) interact with spin-down and spin-up electrons differently. The allowed transitions between the p- and the d-orbitals of the ferromagnet are indicated in the figure for the LCP and RCP light (red and blue) and the spin-down and spin-up electrons (left and right-hand side). It is important to highlight that both the exchange interaction and spin-orbit coupling are required for the observation of MOKE. In case of absence of one, the difference in the absorption energies for spin up and down states remains present. How-

ever, RCP and LCP light get absorbed equally which results in a zero-sum for macroscopic observations. The right-most side of the figure shows the absorption spectrum for LCP and RCP light. The difference in the absorption energy is the reason behind the difference in interaction with the magnetized matter.
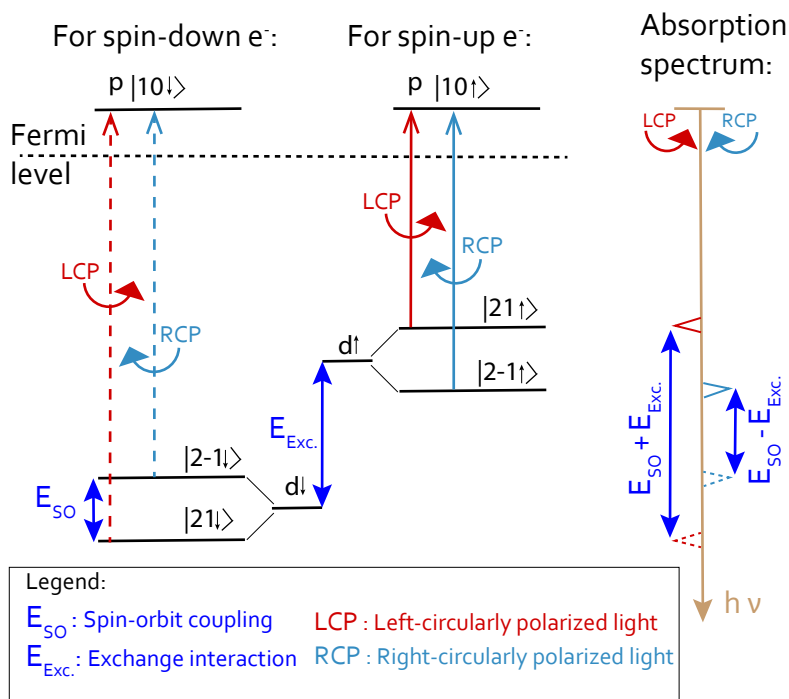
Figure 3.1: Left-hand side: Allowed electron transitions mediated by LCP and RCP light in spin-up and spin-down electrons between the d and p orbitals of a ferromagnet. The levels are named according to the spectroscopic nomenclature. The first number is the orbital (L) (d = 2 and p = 1) and the second is the magnetic sub-levels (m_j). Note that the selection rule dictates that $\Delta m = +1$ and $\Delta m = -1$ for the RCP and LCP light [172]. Right-hand side: The difference in the absorption spectrum for LCP and RCP light. The schematic is modified from the original [173].

3.1.2   Macroscopic observation of MOKE

The macroscopic observation of MOKE is the consequence of a different absorption of RCP and LCP light when both spin-orbit and exchange interaction are present in a material.

This is the case for all the transition metal based ferromagnets in this thesis. Depending on the geometry, which is the magnetization direction of material with respect to the plane of incidence of the probing light, MOKE has different macroscopic outcomes. Figure 3.2 shows the three geometries of polar, longitudinal and transversal MOKE.
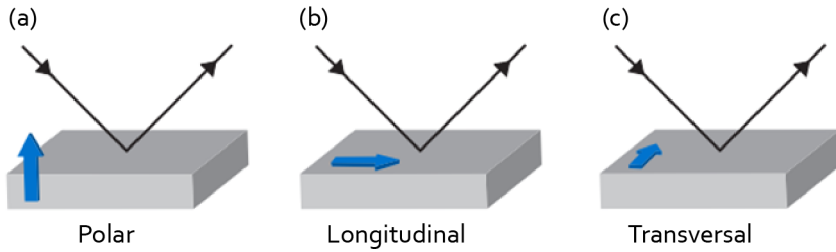
Figure 3.2: (a) Polar, (b) longitudinal and (c) transversal MOKE geometries. The magnetization direction with respect to the plane of incidence is used for the categorization.

In a polar MOKE geometry, initially linearly polarized light that reflects from a perpendicularly magnetized surface attains an elliptical polarization. This elliptical polarization is described by the Kerr rotation (θ) and ellipticity (ε). In this thesis, only the samples with the perpendicular magnetic anisotropy, thus the polar MOKE geometry is used. It is often regarded simply as MOKE in the text. Figure 3.3 (a) depicts the elliptical polarization that the light obtains upon reflection from a magnetized surface. Upon reflection, an amplitude difference occurs between the LCP and the RCP light, which is communicated via the size of the drawn circles. Figure 3.3 (b) visualizes the rotation and ellipticity geometrically.

We can mathematically describe the magneto-optical response of an isotropic material by using a permittivity tensor with off-diagonal elements. The permittivity tensor (ε) relates to the conductivity tensor (σ) by the formula $\varepsilon = 1 + i\frac{4\pi}{\omega}\sigma$, where ω is the angular frequency. Presence of an externally applied magnetic field or permanent magnetization ensures that off-diagonal components of the conductivity tensor, thus the permittivity tensor are non-zero. The presence of off-diagonal components can be intuitively explained as follows. When a magnetic field is present, the conduction electrons that are transported in an orthogonal direction to the field will experience a Lorentz force and be deflected. The off-diagonal elements are the mathematical representation of this action. For the polar MOKE geometry, the permittivity tensor and its non-zero off-diagonal elements are shown

as:

$$\varepsilon = \begin{pmatrix} \varepsilon_{xx} & \varepsilon_{xy} & 0 \\ -\varepsilon_{xy} & \varepsilon_{xx} & 0 \\ 0 & 0 & \varepsilon_{xx,} \end{pmatrix} \tag{3.2}$$

where $\hat{z}$ is the direction perpendicular to the sample surface. Recalling that MOKE stems from a difference in interaction between the RCP and LCP light and the magnetized matter, thus the effective refractive indices of the two polarization states are slightly different from one another, it comes as no coincidence that the eigenvalues of the permittivity tensor are $\varepsilon = \varepsilon_{xx} \pm i\varepsilon_{xy}$, which correspond to the RCP and LCP light. The complex Kerr effect, with its real and imaginary components being Kerr rotation (θ) and ellipticity (ε) (geometrically described in Fig. 3.3 (b)), can be formulated in terms of permittivity tensor elements as [175]:

$$\Phi = \theta + i\varepsilon = \frac{\varepsilon_{xy}}{\sqrt{\varepsilon_{xx}(\varepsilon_{xy} - 1)}}. \tag{3.3}$$

It is important to note that when the magnetization direction is flipped, Kerr rotation and ellipticity that occur in polar geometry change sign while the magnitude of the complex Kerr signal remains the same. Eqn. 3.3, combined with the quantitative observations of the MOKE (Kerr rotation and ellipticity) are used to construct the off-diagonal permittivity tensor elements of the magnetized materials.
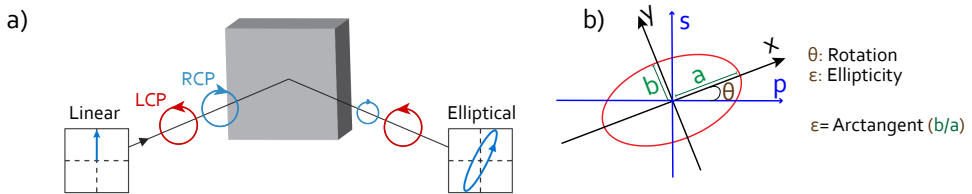
Figure 3.3: (a) Initially linearly polarized light, that is composed of an equal amount of the LCP and the RCP light, reflects off of a perpendicularly magnetized surface. LCP and RCP interact differently with the material (depicted by the difference in reflected circle sizes). As a result, the reflected light attains an elliptical polarization. Modified from [174]. (b) An elliptical polarization state can be defined by rotation (θ) and ellipticity (ε) parameters. The rotated axes of the ellipse are indicated with x and y, while the original axes are shown with s and p.

3.2 Free-space MOKE measurement set-up

MOKE that occurs when light is reflected from a magnetized surface can be measured using a free-space optics set-up. This section describes the working principles of such a set-up and proceeds to a more complex version, the one that is used in the frame of this study.

Let us describe a MOKE set-up in its simplest form and stress how an intrinsically small signal such as MOKE can be detected without using a signal modulation technique, but by using (nearly) crossed polarizers. A source emits the laser light and a first polarizer element P_1 sets the linear polarization state of the light to a certain angle. Then the light reflects off a perpendicularly magnetized sample where the polar MOKE takes place. The reflected light that carries Kerr rotation and ellipticity (θ and ε) in its polarization state then passes through a second polarizer (P_2) which is set at an angle α with respect to the first polarizer. Finally, the light reaches a detector, and its intensity is recorded. The normalized light intensity reaching the detector can be formalized via the Jones formalism [176] as:

$$\frac{I_{det}}{I_0} = R \left(\cos^2(\alpha) + (\varepsilon^2 + \theta^2) \sin^2(\alpha) + \theta \sin(2\alpha) \right), \quad (3.4)$$

where R is the reflectivity of the magnetized sample. Considering the Kerr signal is intrinsically very small, thus disregarding the higher order terms on θ and ε yields:

$$\frac{I_{det}}{I_0} = R \left(\cos^2(\alpha) + \theta \sin(2\alpha) \right). \quad (3.5)$$

Following from Eqn. 3.5, the Kerr rotation is observed at its best when the relative angle α between the two polarizers is nearly crossed (almost orthogonal). This is a simple set-up which yields results albeit with a low signal-to-noise ratio. Additionally, the set-up can only determine the Kerr rotation θ as indicated in Eqn. 3.5. Despite these disadvantages, the (nearly) crossed polarizer configuration is used in the Kerr microscopy set-up, detailed further in Sect. 3.5.1.

In the frame of this study, we used a MOKE measurement set-up that implements a signal modulation technique together with a lock-in amplifier, to achieve a higher signal-to-noise ratio and determine both the Kerr rotation and ellipticity in a single measurement. Let us describe this advanced set-up which is depicted in Fig. 3.4. As a method of signal modulation, a Photo-Elastic Modulator (PEM) is used. A PEM is a voltage controlled crystal that oscillates the light's polarization state between the right- and left-handed polarization

states at a 50 kHZ frequency. A diode laser is used which provides non-polarized light. The first polarizer P_1 is positioned right after it, with its main axis at $45°$ angle with respect to the y-axis. A PEM whose fast axis makes $0°$ angle with respect to the y-axis is placed after the polarizer. A lens is used to focus the polarization modulated light onto a sample holder containing the magnetized sample. The diameter of the laser spot is measured to be 2 μm on the sample surface. After a perpendicular incidence, the reflected light that carries the MOKE in its polarization state is focused on a second polarizer (P_2) whose main axis is $0°$ angle with respect to the y-axis. Passing through the last polarizer, the light is received at an amplified Si detector where its intensity is recorded. Thanks to the communication with the lock-in amplifier, the time dependence of the detected light intensity is matched with the first and the second harmonic oscillations of the PEM and recorded as an AC signal. In addition to time-dependent signal, the component that is independent of time is recorded as a DC signal. As depicted in Fig. 3.4, an electro-magnet (the one with two poles) is included in the set-up that can apply up to 500 mT of magnetic field between its poles, in both directions. Prior to describing how a typical measurement in the free-space MOKE set-up looks like, let us formulate the output obtained from the set-up in this configuration.

The optical components of the set-up, including the sample itself, can be described using Jones matrix formalism. This allows us to formulate the observed results to later fit the unknown parameters such as the Kerr rotation and ellipticity. Table 3.1 lists the matrices corresponding to the various elements in the optical set-up.

Additionally an element that is not listed in Table 3.1, a polarizer oriented at an angle α can be defined using the rotation matrix as:

$$P(\alpha) = R(\alpha) \cdot \begin{pmatrix} 1 & 0 \\ 0 & 0 \end{pmatrix} \cdot R(-\alpha). \tag{3.6}$$

When all the optical components are defined as such, the electric field vector of light that reaches the detector (E_{det}) is calculated by simply multiplying the matrices according to the sequence of interaction as depicted in Fig. 3.4.

$$E_{det} = P(0°) \cdot S \cdot PEM(0°) \cdot E_0(45°), \tag{3.7}$$

Where S indicates the sample matrix. Since the intensity of a field is proportional to its field amplitude squared:

$$I_{det} = E_{det} \cdot E^*{}_{det}, \tag{3.8}$$

the detected intensity is formulated as:

$$I_{det} = I_0 R \left(\frac{1}{2} + \theta \cos\left(B_0 \cos(\omega t)\right) - \varepsilon \sin\left(B_0 \cos(\omega t)\right) \right). \tag{3.9}$$

As briefly mentioned earlier, PEM causes the light's polarization to oscillate between the RCP and LCP states at a certain frequency. The oscillatory phase difference that the PEM causes is described in Eqn. 3.9, where the term B_0 indicates the amplitude of this phase difference (also referred to as the retardance), while the term ω indicates the frequency by which the retardance is oscillating. Trigonometric functions of $B_0 \cos(\omega t)$ can be expanded
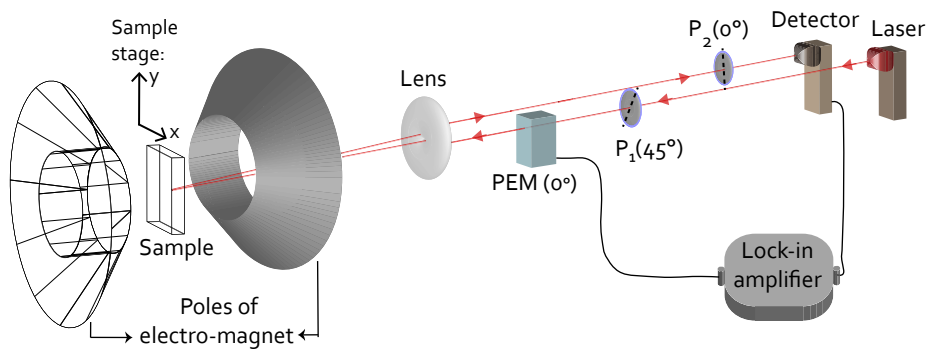
Figure 3.4: Schematic depicting the free-space MOKE measurement set-up. A laser light (λ = 638 nm) is polarized (via P_1) then modulated at 50 kHz (via PEM) and incident on a magnetized sample. The reflected light is filtered with a polarizer (via P_2) and then its intensity is recorded at the detector. In addition to a time-invariable signal, the detector records the first and the second harmonic oscillations of the PEM with a lock-in amplifier. During measurements, electro-magnet poles applied magnetic fields (perpendicular to the sample surface) up to ± 500 mT on demand. The sample stage movement in the xy plane enables monitoring different regions of the sample. This is useful for samples with continuous spatial layer thickness variations (wedge thickness).

Name	Matrix	Remarks
$\mathbf{E}_0$ input field (α)	$\begin{pmatrix} \cos(\alpha) \\ \sin(\alpha) \end{pmatrix}$	α is the angle wrt. p-polarized light's E-field
Sample with MOKE	$\sqrt{R}\begin{pmatrix} 1 & \Phi \\ -\Phi & 1 \end{pmatrix}$	$\Phi = \theta + i\varepsilon$
PEM(0°)	$\begin{pmatrix} 1 & 0 \\ 0 & \cos(B) + i\sin(B) \end{pmatrix}$	$B = B_0\cos(\omega t)$
Rotation(α)	$\begin{pmatrix} \cos(\alpha) & \sin(\alpha) \\ -\sin(\alpha) & \cos(\alpha) \end{pmatrix}$	α is the angle wrt. p-polarized light's E-field

Table 3.1: A table describing the optical components of the free-space MOKE set-up and listing their formulations using Jones matrices. In the first column, the names of the components with additional information on the optical axis orientations are given. In the second column, the matrices that correspond to their functionalites are listed. The third column is reserved for the explanations. Defined within the sample matrix, R and Φ indicate the sample's reflectivity and the complex Kerr signal. Within the PEM matrix, the cosinusoidal dependence B indicates that the polarization of light is modulated with frequency ω as a function of time t where B_0 is the retardance [177].

into harmonic series of the PEM frequency by the relations

$$
\cos\left(B_0\cos(\omega t)\right) = J_0(B_0) + 2\sum_{n=1}^{\infty}(-1)^n J_{2n}(B_0)\cos(2n\omega t),
$$

$$
\sin\left(B_0\cos(\omega t)\right) = 2\sum_{n=0}^{\infty}(-1)^n J_{2n+1}(B_0)\cos((2n+1)\omega t),
$$

(3.10)

for which $J_n(x)$ is the nth order Bessel function of the first kind. Replacing the terms in Eq. 3.9 with these expansions up to the second harmonic degree, the intensity measured by

the detector can be determined in terms of a constant (I_{dc}), the first (I_{1f}) and the second harmonic (I_{2f}) oscillation contributions. The normalized light intensities are

$$\frac{I_{dc}}{I_0} = R\left(\frac{1}{2} + \theta J_0(B_0)\right),$$

$$\frac{I_{1f}}{I_0} = -R\,2\varepsilon J_1(B_0)\cos(\omega t), \tag{3.11}$$

$$\frac{I_{2f}}{I_0} = -R\,2\theta J_2(B_0)\cos(2\omega t).$$

Since the values of Bessel functions at the retardance of B_0 are known, what follows from Eq.s 3.11 is that using a lock-in amplifier and monitoring the $1f$ and $2f$ frequencies, one obtains signal amplitudes that are proportional to Kerr ellipticity (ε) and rotation (θ), respectively. However, it should be stressed that in order to translate signal amplitudes that are detected at different frequencies into a quantitative Kerr signal analysis, calibration coefficients are needed [178]. In the frame of this work, we used a reference sample, grown and measured by our collaborator [179] to determine the calibration coefficients.

3.2.1   MOKE in multi-layered thin-films

In the frame of this thesis, ferromagnetic multi-layered thin-film stacks that combine magnetic and non-magnetic metals are used as the non-volatile memory components. The stacks are formed by sandwiching ferromagnetic Co layer(s) between Pt layers that are non-ferromagnetic (under normal conditions) [180, 181]. MOKE which occurs after reflection from a multi-layered medium is a combination of multiple optical phenomena such as reflection, refraction and magneto-optic effects. A mathematical model suggested by Zak *et al.* [182] is used to account for the magneto-optic contributions of the magnetized layer(s). Using the model, a magneto-optical Voigt constant is assigned to the magnetized layers. By combining the model with a tailored sample-set that has variations in Co and Pt layer thickness, the magneto-optic activity as a function of thickness is probed. Findings of this study which shed light on the effect of the Co/Pt interface on magneto-optic activity are reported in Chapter 4.

Let us describe the model in more detail. Since the total thickness of the contributing layers of a multi-layered thin-film stack is significantly smaller than the wavelength of the probing light, the MOKE from each layer contributes to the overall effect in a cumulative manner. In the model, the cumulative MOKE is analytically described via the layer-

dependent parameters of the refractive index (N), the magneto-optical Voigt constant (Q) and the thin-film thickness (d); as well as the layer-independent parameters of the angle of incidence at the first medium (θ) and the probing light wavelength (λ). A non-magnetic layer is defined simply by assigning $Q = 0$. For the light's propagation within a layer, a medium propagation matrix is defined. For the interface between the two layers, a medium boundary matrix that embeds the boundary conditions is formed. By using the Jones matrix formalism [176] a multi-layered stack is described in terms of matrix multiplications of medium propagation and medium boundaries. The details of this process are described in Appendix A.1.

3.3   Design of integrated photonic devices

This section is dedicated to the design and the mathematical modelling of the integrated magneto-photonic devices. The design process is aimed at delivering magneto-optical reading of a non-volatile memory. As briefly mentioned earlier, a magnetic cladding that is placed on top of a waveguide gives rise to MOKE, which in return causes an intrinsically small mode conversion between the eigenmodes of the waveguide, TE and TM. Depending on the magnetization direction of the cladding (up- or downwards magnetized), the mode conversion occurs with an opposite phase, while the amplitude of the conversion is the same for both magnetization directions. In other words, the phase of the emergent mode encodes the information of the magnetization direction of the cladding, thus its memory state. Correspondingly, we designed a device that yields two different transmitted light outputs depending on the magnetization direction of its built-in memory component. This is achieved by two different designs. The first one that is based on interferometer is described in Chapter 5 while the second one combining a polarization rotator element and polarization-selective (mode-selective) in- and out-couplers is described in Chapter 6.

3.3.1   Design toolbox

In this section we introduce the photonic design tools used in the frame of this work. A commercial software [183] is used for simulating the optical phenomena. Depending on what is the aim of the simulation, different solvers that belong to the same software packet are preferred. The first -and the most complex- solver uses a 3-dimensional (3-D) Finite Difference Time Domain method to solve the time-dependent Maxwell's equations over a

finite grid [184]. In the FDTD method, the electric and magnetic field vector components are calculated over a volume, for consecutive time frames and in a repeated manner; until a steady-state electromagnetic field solution is reached. It allows us to define shapes and optical material properties (including magneto-optic effects) within the computational volume. It includes specialized light sources for integrated photonics. Such sources include monitors that calculate the existing modes in a certain cross-section and allow for injection of the preferred mode(s) onto this section on-demand. Additionally, its various monitors help visualizing if the simulated volume reflects the reality well enough. The results from these monitors include 2-D refractive index maps and 2-D electric and magnetic field distribution maps. Positive notes aside, the FDTD solver has its limitations. Its high memory and computational requirements when simulating relatively small structures, made it harder to afford the standard operations such as parameter sweeps for optimization purposes. For this reason, in the parts of the device that do not require definition of magnetized materials (which is a partial cladding in this work), we used another solver: the Eigen Mode Expansion (EME) [185]. This solver calculates the modes that can exist within a defined cross-section geometry, and projects them onto the modes that exist in different cross-section regions. We used it extensively for the mode-beating visualizations. The last and the simplest solver that is used in the frame of this work is the Finite-Difference Eigenmode (FDE) [186]. We referred to it when solutions regarding mode profiles and mode effective refractive indices are needed.

3.3.2 MOKE in waveguides

This section focuses on the MOKE in waveguide modes. We describe the setting in which the MOKE takes place in waveguides. As mentioned earlier, the desired functionality of magneto-optical memory reading in magneto-photonic devices is built around the MOKE. Therefore, prior to designing magneto-photonic devices, it is important to quantitatively predict the MOKE in waveguides.

Let us describe the waveguide configuration in which the MOKE takes place. Figure 3.5 shows a waveguide section that is equipped with a built-in non-volatile magnetic memory bit, in the form of a multi-layered, ferromagnetic, thin-film top-cladding. The cladding has PMA as shown by the up- and downwards arrows, which means the preferential magnetization orientation lays out-of-plane. In this setting, the MOKE occurs as the confined light in the waveguide interacts with the magnetized top-cladding through the evanescent tail

of the guided mode. The interaction volume is depicted as an exponentially decaying intensity profile, away from the waveguide towards the magnetized top-cladding layer. Unlike the single reflection in free-space MOKE set-up, the setting described in Fig. 3.5 presents a magneto-optic interaction that continues throughout the cladded region. For didactic purposes we simplify the wave-guiding principles and describe the guided mode as a set of wave vector components (k_x and k_z in the figure). Among the two components, only k_z contributes to the polar MOKE. An intuitive reasoning for this is that the polar MOKE occurs only if the projection of the wave vector onto the cladding's magnetization vector is non-zero. This is mathematically described as the perpendicularly magnetized material's off-diagonal permittivity tensor elements. As shown in Eqn. 3.2, the off-diagonal components are present only at positions ε_{xy}. The k_z contribution of the guided mode is determined by the waveguide geometry, specifically its cross-section. To maximize the polar MOKE in waveguides, thickness and width can be engineered. However, one should bear in mind that the wave-vector description is an over-simplification. Changing the waveguide geometry, changes the number of modes and their spatial distributions (optical power distributions) as well. Considering such complexity, we used the commercially available optical simulation software mentioned in Sect. 3.3.1 to calculate the MOKE in waveguides.

In this paragraph we provide details on the settings of the optical simulations. Regarding the values of refractive indices and magneto-optic Voigt constants of all contributing materials, we refer the reader to Chapter 4. In simulations, the magneto-optical phenom-
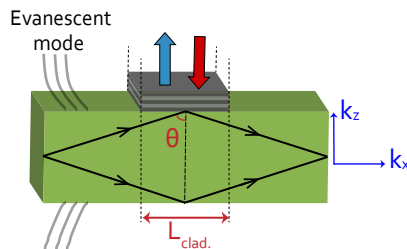
Figure 3.5: Waveguide section with magnetic top-cladding (non-volatile memory). The guided mode is indicated via the wave vectors (k). Evanescent tail of the guided mode is depicted as exponentially decaying optical intensity outside the waveguide core. The waveguiding condition is simplified by the wave vector (arrows inside the waveguide) depiction and total internal reflection condition (angle θ). The vector is separated into components of k_x and k_z to highlight that only the k_z contributes to the polar MOKE.

ena are emulated by defining a grid attribute as communicated in the knowledge base reports [187]. As the boundary condition of the calculation windows, Perfectly Matched Layers (PML) are used to absorb the electromagnetic waves that are incident on them, minimizing reflections. A conformal mesh, whose size is decided by the most critical dimension (thickness of the cladding), is added with 2 nm accuracy. Dedicated optical power inputs are used to inject the guided mode of choice, in most cases the fundamental TE mode. To probe the MOKE in waveguides, we use two types of two-dimensional monitors. The first one monitors the polarization state of the light, irrespective of which guided mode contributes to such a polarization [187]. The second one monitors the mode-specific changes in optical power by calculating mode expansions [185]. The outputs from the former monitor are better represented in the Poincaré sphere format due to their success in providing insightful polarization state evolution plots. The outputs from the latter monitor are used to depict the mode conversion due to the MOKE.

As indicated in earlier sections, the FDTD simulations have high computational and memory requirements, which gets worse when the MOKE is introduced. To help the solver, we reconstructed the magnetized multi-layered thin-film cladding to have larger volume that effectively has the same refractive index. We refer to this larger volume material as the diluted refractive index material and we explained its mathematical formulation including the magneto-optic Voigt constant calculations in Appendix A.2.

3.3.3   Design process

This section describes the design process of the integrated magneto-photonic devices. Prior to describing the design process, it is important to highlight that the design and the fabrication are coupled processes. The ability of realizing a certain structure via nano-fabrication determines the boundaries of the design. The photonic design process starts by defining the desired functionality. In the frame of this thesis, the desired functionality from an integrated photonic device is the all-optical reading of it's built-in magnetic memory. As the next step in the design process, one considers what kind of an engineered response from a device can serve this functionality and what combination of optical components should be chosen to yield such a response. As the works presented in this thesis demonstrate, different component combinations can serve the same functionality. Chapters 5 and 6 present interferometer and partial mode converter devices that that exemplifies this. More details on their designs, such as considerations on the performance and size (the footprint) are

given in respective chapters. Fig. 3.6 summarizes the following steps in the design process
that starts after determination of the optical components.
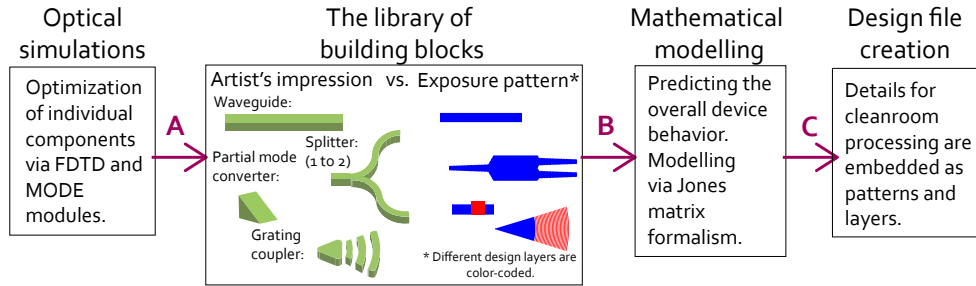
Figure 3.6: A schematic describing the design process. The process starts with optical sim-
ulation of individual components (building blocks). Then, the mask patterns (for exposure)
of each block is decided upon. Later, a mathematical model describing the overall device
behavior is used to predict what would be the output when building blocks are composed
in a certain way. Lastly, a design file containing necessary information for the cleanroom
fabrication is compiled.

As the arrow A indicates the optical simulations (FDTD and MODE) assisted the com-
ponent design. Length parameters of the structures are swept for obtaining better perfor-
mances. The optimized components are collected in the library of building blocks. This is
kept up to date by the collective efforts of the Photonic integration group. More informa-
tion about the library and its uses are presented in the following paragraphs. As indicated
with arrow B in Fig. 3.6, a mathematical model based on Jones matrix formalism is used to
predict the collective functioning of the individual components. Lastly, as indicated with
arrow C, the design process is finalized by preparing a digital design file [188] to be used
during the cleanroom fabrication process. The file is generated by using a Python-based
module called Nazca [189]. The module implements the IMOS library of building blocks
where each component is matched with an exposure pattern and a layer number. The ex-
posure patterns are placed at different layers in the design file depending on the order of
processing (i.e. the order of the e-beam lithography sessions). Prior to concluding this sec-
tion, let us provide more information on the IMOS library of building blocks. The building
blocks used in this work are listed in Table 3.2, together with their respective definitions.

A list of optical components

Name:	Definition:
Waveguides	Confines the light in its core (cross-section of 300 * 400 nm, thickness * width) and guides toward intended locations. Its length is chosen on-demand. By design, only the fundamental TE and TM modes are supported.
Bends	Connect waveguides to one another by curvature sections of a desired angle.
Grating couplers	TE and TM mode-selective focusing grating couplers [135, 136] are available to couple-in and couple-out the light. Their grating's periodicity and fill factor are designed accordingly to match the effective refractive indices of the modes they are selective for.
Splitters	Multi-mode interferometers split the guided light intensity in desired proportions. They function by allowing an area in which multiple modes interfere with one-another. At positions of constructive interference, their branching waveguides are positioned. 1x2, 2x1 and 2x2 splitters are used [134].
Mode converters	Also called polarization converters [141]. In this work, triangular cross-section waveguides are used to partially convert the guided modes (different polarizations) into one-another. The conversion occurs due to propagation in an asymmetric waveguide cross-section whose eigenmodes are tilted with respect to the rectangular waveguide.
Delay lines	These are added propagation path lengths that are formed by curved waveguides arranged in swirling or escargot patterns. The path length parameter is chosen on-demand.
Interfero-meters	In this work, an unbalanced Mach-Zender interferometer is used. It is a combination building block made out of splitters, waveguides, delay lines and mode converters.

Table 3.2: Names and definitions of some of the optical components (building blocks) used in this work. More details on their morphology and the exposure patterns during lithography are depicted in Fig. 3.6. The components are based on the IMOS fabrication platform [190]. The starting material stack and the references to the refractive indices are detailed in Sect. 4.

3.4   Sample fabrication

This section explains the fabrication techniques used for realizing ferromagnetic multi-layered thin-films and magneto-photonic devices.

3.4.1   Magnetron sputter deposition

Sputtering is a physical vapor deposition technique where high purity materials of choice, called targets, are condensed on a substrate in the form of a thin-film. The multi-layered thin-film ferromagnets used in this study are fabricated via the magnetron sputter deposition technique. Thin-films grown with this technique are amorphous up to a critical thickness of approximately 2 nm, which later becomes 'textured polycrystalline'. For ferromagnetic multi-layers studied in this thesis, no annealing step is required. The deposition equipment and the process are depicted in Fig. 3.7. During depositions, the inert gas of Ar with ultra high purity is kept at 10^{-2} mbar pressure inside the chamber. Via the implementation of an anode ring and the setting of the target as a cathode, a high voltage difference is created which causes Ar atoms to ionize into Ar^+ and e^-. As shown with arrows in Fig. 3.7, Ar^+ ions are accelerated towards the target (cathode) and the collisions eject the target atoms from their locations. The ejected atoms are sputtered on to the substrate. As the ejected atoms reach the substrate with enough energy, they settle down at energetically favorable positions, resulting in the highly textured polycrystalline thin-films [191]. A magnet is placed behind the target to increase the rate of the sputtering and to prevent growth rate deviations. The growth rates of the materials Ta, Pt, and Co were 0.564 Å/s, 0.803 Å/s, and 0.420 Å/s, respectively. A previous study conducted in our group has shown that by varying the background gas pressure, the properties such as the growth mode and the surface roughness of the thin-films can be controlled up to a certain degree. This effect is explained by the background gas pressure changing the energy of the incoming atoms during deposition [192].

As demonstrated in Chapter 4, studying multi-layered samples with thickness variations in certain layers offers valuable insights into the interfacial magneto-optic activity. These samples are fabricated with using a wedge mask that shades the substrate surface from a short distance above as shown in Fig. 3.7. This is used to fabricate samples with a thickness variation in the lateral direction. These samples with thickness variations are then measured using the set-up described in Sect. 3.2 using a focused laser spot. As a result, the

dependence of the MOKE on the layer thickness is determined using a single sample, while achieving high resolutions.

3.4.2 Fabrication of photonic devices

This sub-section explains the fabrication of integrated photonic waveguide structures with magnetic thin-film stacks, structured as top-claddings. These devices are a combination of photonic and magnetic components, among which the photonic parts make up the largest portion. In this work we refer to them as magneto-photonic devices. The photonic parts were fabricated by our collaborators [193] in a multi-project wafer run using the Indium Phosphide Membrane On Silicon (IMOS) platform [190]. The process takes place in a cleanroom environment and is accomplished by using multiple Electron Beam Lithography (EBL) steps followed by dry and wet etching of InP. "Dry" refers to gaseous plasma etching while "wet" refers to acid solution etching. The magnetic components, namely the non-volatile memory components were added to the photonic components as waveguide top-claddings with overlay EBL, followed by magnetron sputter deposition and lift-off steps.

In the current study, the photonic components are first processed and then bonded to a Si substrate with a method called pre-bonding. The starting medium for fabrication was an InP substrate carrying an epitaxially-grown multi-layered InP membrane. The thickness of the membrane layers are of great importance since these layers later became the body of
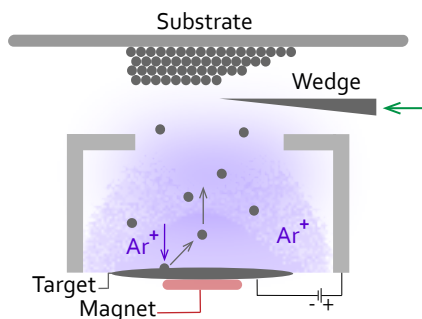
Figure 3.7: A schematic depicting magnetron sputter deposition. An applied voltage partially ionizes the Ar gas. Positively charged Ar ions are accelerated towards the target. Upon collision, the target atoms are removed from their original positions and deposited onto the substrate. A magnet assists the process and ensures uniform deposition rates. A motion controlled wedge mask is shown that is used to control the thickness profile of the sample over a lateral distance.

the photonic components. Recall that these components are listed and briefly introduced in Sect. 3.3.3. Due to a smaller required thickness of the regular components (e.g. the rectangular waveguides) with respect to the triangular cross-section waveguides (that are used for partial mode conversion), an acid etch-back procedure on areas with regular components is done. Etch-stop layers of InGaAs and InGaAsP are included in the multi-layered membrane stack. A summary of the pre-bonding process steps is provided below with Fig. 3.8 demonstrating some of the actions. Additionally a more detailed recipe (numbered steps) is given below.
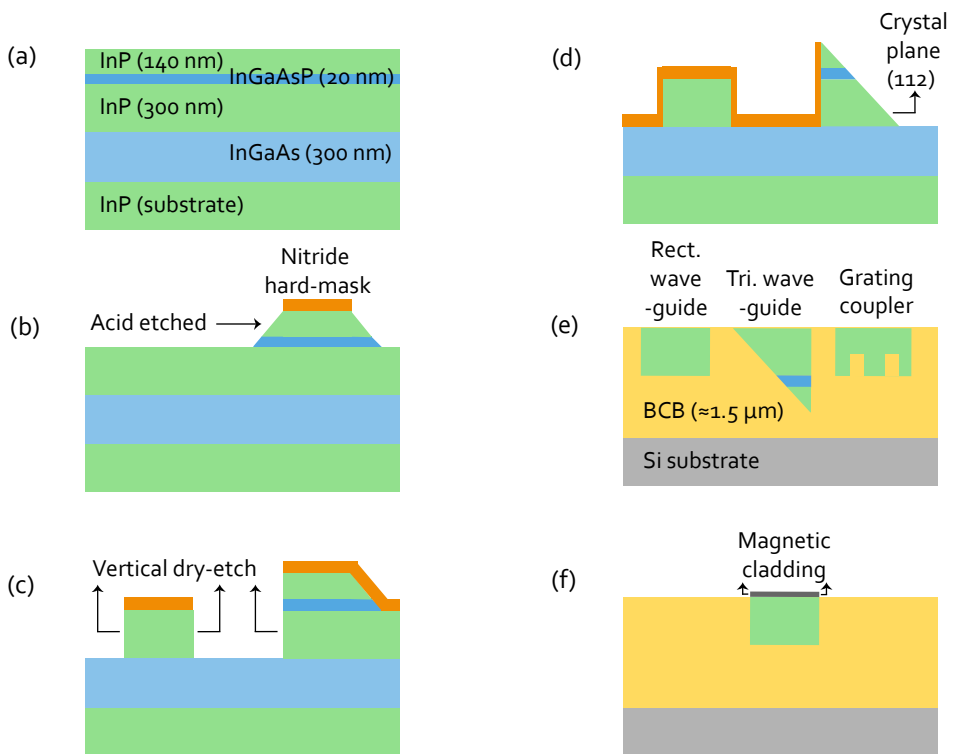
Figure 3.8: Schematic description of the fabrication steps for realizing magneto-photonic devices. (a) Shows the starting stack, (b) depicts the membrane height defining wet-etch, (c) depicts the vertical side-wall etch, (d) shows the wet-etch for the sloped side-walls of triangular waveguides, (e) shows the flipped structures bonded with BCB to a Si substrate and (f) shows the placement of magnetic claddings on waveguide sections.

1) A (100)-oriented InP wafer substrate with the stack order of (subst.)/[A]/[B] where [A] is InGaAs (300 nm) and (B) is InP (300 nm)/ InGaAsP (20 nm)/ InP (140 nm) is chosen as the starting medium. Note that the numbers indicate the growth order on the InP substrate. The first part [A] served as an etch-stop layer to protect the InP wafer and the second [B], formed the photonic components.

2) The first EBL step is dedicated for defining the EBL markers that will be used for the upcoming overlay exposures. The depth of the markers is made larger than 1 μm to provide enough e-beam reflection contrast for automated detection by the lithography equipment. An Inductively Coupled Plasma (ICP) etching is used to create the vertical side-walls.

3) With the second EBL session, high and low thickness membrane regions are determined. 50 nm thick silicon nitride (SiN_x) is deposited on the InP wafer as a hard-mask. On top of it, the positive resist ZEP 520 is spin-coated. Despite the required exposure area being large, the positive resist is adopted due to the superior performance and reproducibility reasons. During the EBL session, the regions of the future devices minus the regions of the triangular waveguides are exposed. Following this, by using Nitride Reactive Ion Etching (RIE) tool, the resist pattern is transferred onto the hard mask. The remaining resist is cleared off by using Polymer RIE equipment. To decrease the membrane thickness in desired areas, a two-step selective (acid) etching is followed. First, an $HCl:H_3PO_4$ (1:4) solution is used to etch back the InP layer. After the top InP is consumed and the etch-stop layer (InGaAsP) is reached, a second acid solution of $H_2SO_4:H_2O_2:H_2O$ (1:1:10) was used to remove the InGaAsP layer. Then the nitride hard-mask is removed by a buffered Hydrofluoric acid (BHF) solution, preparing the wafer for the next steps.

4) This step is dedicated to define the grating couplers that have a different vertical side-wall carvings depth with respect to the waveguides. With an EBL step, the positive resist is transferred to the nitride hard-mask. Upon creating the desired openings in the nitride hard mask, a vertical dry-etch (ICP) is realized. Aiming for 120 nm (and reaching at 127 nm) vertical depth carved into the InP membrane, the nitride mask is cleared off once again.

5) In this step, the vertical side walls of the components (including triangular waveguides) are defined. After the EBL step, the pattern in resist is transferred to the nitride layer and the openings in InP are created. By using ICP dry etching, the vertical etch is completed. The hard-mask is removed.

6) In order to create the sloped side walls of the triangular sections, wet etching with $HCl:H_3PO_4$ (1:4) and $H_2SO_4:H_2O_2:H_2O$ (1:1:10) are followed to etch the InP and InGaAsP membranes, respectively. Since the etching is self-limiting when the denser (112) crystal

plane is reached, a $35°$ angle slope starting from the nitride protected vertical wall and reaching till the InGaAs etch stop layer is created. Afterwards the hard mask is removed with BHF.

7) Following these steps, the structures are prepared for bonding with a Si substrate. This is done by deposition of 100 nm and 400 nm SiO_2 claddings in InP membrane and the Si wafer, respectively. This step helped to increase the adhesion with the bonding agent. The bonding agent is Benzo Cyclo Butene (BCB) with an approximate thickness of 1.5 μm. The InP wafer is bonded to a Si wafer in a way that the structured parts are buried in BCB. Later, the carrier substrate InP and the etch-stop layer are etched away, leaving behind the high refractive index contrast photonic components.

8) The last EBL step is realized to place the magnetic memory components on top of the photonic components. For this lithography step, a bilayer negative resist polymer is used considering the ease of the metal lift-off procedure that would follow. The predefined EBL markers ensured that the memory bits are placed precisely as top claddings on the waveguides, at desired locations. After the EBL session, resist openings are de-scummed by a short oxygen plasma etching. This etching is very mild and does not disturb the non-exposed resist. The importance of the de-scumming step is to ensure a clean crystalline InP surface where metal layer can be grown on top with minimum transferred surface roughness. Following this, the sample is placed in UHV chamber for magnetron sputter deposition of the desired multi-layered stack order. The lift-off procedure involved soaking the sample in acetone overnight. Unlike standard lift-off procedures, a sonic bath is avoided, in this way protecting the integrity of the membrane-based photonic devices.

One of the important aspects to be considered prior to the fabrication was the directionality of the photonic components with respect to the crystalline plane orientation of the InP membrane. Since defining the sloped-wall triangular waveguides relied on the wet etch procedures that self-terminate in certain plane orientations, a maximum angle of $1.5°$ was allowed between the primary flat of a (100)-oriented InP wafer and the light's propagation direction.

3.5 Characterization of integrated photonic devices

3.5.1 Kerr microscopy

In some of the work presented in this thesis, magneto-optical characterization of small area samples with feature sizes of 400 nm is needed. This is not possible using the conventional MOKE set-up described in Sect. 3.2, due to the 2 µm spot size of the probing laser which averages out the nano-scale features. In Kerr microscopy on the other hand, a spatially resolved image can be obtained, similar as in optical microscopy. In this case the light intensity is proportional to the magneto-optic Kerr Effect, as indicated by the Eqn. 3.5. Let us describe the Kerr microscopy used in this work, and explain its functioning principles including how the obtained image's light intensity corresponds to the Kerr amplitude. As depicted in Fig. 3.9, two polarizers that are almost crossed with respect to one another are positioned in the light path of the microscope. As explained in Sect. 3.2, this setting causes the intensity of the reflected light to be proportional to the Kerr effect. A MOKE-mode selecting aperture, located between the light source and the objective, is used to regulate the angle of incidence of light onto the magnetized sample surface. By choosing an angle of incidence that is relatively more perpendicular to the surface, the microscopy set-up is made sensitive to the out-of-plane component of the sample magnetization. In other words, this set-up is tuned for probing the polar MOKE. A magnet coil that is positioned under the sample is used to apply perpendicular external magnetic fields up to 300 mT. By changing the applied magnetic field while recording the changes in optical intensity, magneto-optic effects are measured. Note that the spatial resolution is limited to the diffraction limit as in regular optical microscopy.

3.5.2 Integrated optics transmission set-up

This section describes the optical transmission set-up that is used for the characterization of the magneto-photonic devices. The set-up is built such that the optical transmission through devices can be measured while the magnetization direction of the built-in ferromagnetic memory bits is alternated. The aim of the set-up is to provide experimental evidence on the functioning of the magneto-photonic devices, by determining the difference in the output mode intensities for opposing memory states. The schematics of the set-up is given in Fig. 3.10. An external Tunable Laser Source (TLS) that operates at telecom wavelengths (1460-1565 nm) is coupled into the devices by using a fiber-optic cable. With a microscope, the fiber's position with respect to the mode-selective grating couplers are determined. Movement of fibers is enabled by 3-axis stage that can be positioned with mi-

cron accuracy. Fibers are held by the holders at a 10° angle to the surface normal, which corresponds to the angle that the grating couplers work optimally. A second fiber positioned above the out-coupler directed the transmitted light into an external power meter. An electromagnet served as the sample holder. With that, magnetic fields up to 300 mT can be applied in both positive and negative directions. The field is used to set the magnetization direction of the claddings, thus to set the memory state of the bits. Computer control of the set-up is realized for TLS light input, power measurements and the externally applied magnetic field. The measurements are automated, repeated and processed using scripts which ensures consistent sampling.

This paragraph describes the measurement protocols in greater detail. In the frame of this project, two different methods are used to collect the optical transmission data from the fabricated devices. The first one, called the hysteresis method, is aimed at demonstrating the effect of the magnetization history on the optical transmission. The hysteresis measurement starts by setting the magnetization direction of the built-in memory component (top-cladding) at a certain direction. This is done by applying an external magnetic
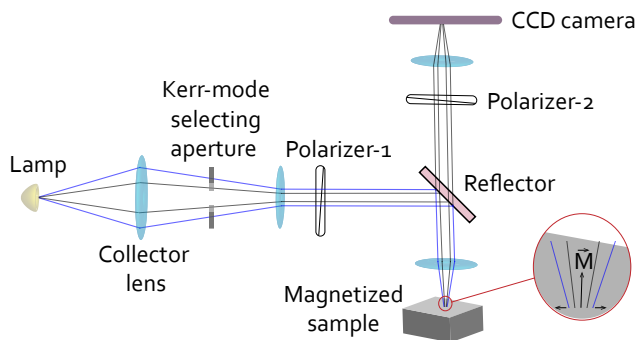
Figure 3.9: Schematic depicting the Kerr microscopy set-up. Light from a randomly polarized, high intensity Mercury arc light source (lamp) is collected by the collector lens. The light path is selected by arranging the size of the Kerr-mode selecting aperture. After the light passes a collimating lens and the first polarizer, it is reflected onto the sample. The reflected light is collected by the objective before passing the second polarizer that acts as an analyzer, i.e. the change in polarization between polarizer 1 and 2 is proportional to the Kerr signal. This is then projected onto a CCD camera allowing for wide field Kerr-Microscopy. The illuminated region of the sample, showed as a zoom-in inset, bordered by black and blue light paths, visualizes the function of the mode-selector aperture on how polar (black) or longitudinal (blue) MOKE-mode is chosen.

field in the desired direction for 0.1 seconds, which is strong and long enough to overcome the coercivity of the cladding. Hereafter, the magnetic field is swept from high to low field magnitudes. When the applied field is decreased to zero, the field changes to the opposite direction. By consequently increasing the field magnitude, a branch of the hysteresis is measured. A complete hysteresis is measured by repeating this process with the starting magnetic field in the opposite direction. To obtain a data-point in the hysteresis, the magnetic field is turned on for 50 ms and the transmitted power is measured 50 ms after turning off the external magnetic field. The reason applied field is switched off prior to measuring and the system is allowed to rest for a short while is the heating effect caused by the running current in the magnetic coil. For interested reader, this problem and its solution is explained in more detail elsewhere [194].

This is repeated at each magnetic field value of the sweep. With this method, the field at which the magnetization direction change occurs is recorded, both for negative and posi-
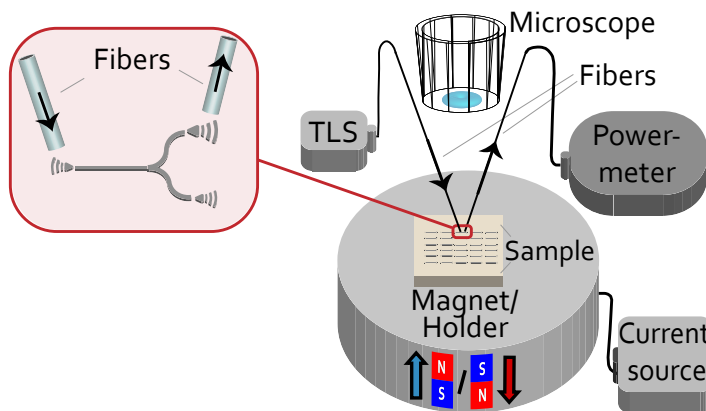
Figure 3.10: A schematic showing the set-up dedicated to measure the optical transmission from integrated photonic devices. The sample holder is an electro-magnet that can apply ± 300 mT perpendicular magnetic field. This is used to set the magnetization direction of the built-in memory component in devices. When the memory is set, the field is removed and the optical transmission measurement starts. The tunable Laser Source (TLS) sends the light (λ = 1550 nm) into the input fiber. As shown on the left-hand side with a zoom-in section, a grating coupler couples the light into the device. After transmission through the device, another grating coupler couples out the light and the output fiber collects it and sends to the power-meter. The microscope is placed on the set-up to allow for the manual alignment of the fibers on top of the grating couplers.

tive directions. Although with this method it is possible to determine the difference in transmission for two magnetization directions, it is time-wise costly to sweep all the field values before obtaining a magnetization direction switch. Therefore, a second method that induces a faster switch is developed. The second measurement method is focused on probing the difference in the light transmission rather than the field at which the magnetization switch is induced. Therefore, the magnetization direction of the cladding (the memory bit) is constantly switched between up- and downwards magnetized states by applying a strong magnetic field that is equal in amplitude and opposite in sign.

Chapter 4

An investigation of the interface and bulk contributions to the magneto-optic activity in Co/Pt multi-layered thin films

We report an experimental study which focuses on the magneto-optic interaction between light and perpendicularly magnetized ferromagnetic thin-film multilayers. Samples containing multiple Co/Pt interfaces are measured via the polar MOKE. Thanks to a continuous Co thickness variation, and single and double Co layered samples, interface and bulk contributions to the magneto-optic activity are separately determined. Kerr signals are recorded as a function of the Co thickness. The results are analyzed via a transfer matrix method that accounts for the standard optical and magneto-optic effects in multi-layered thin-films. Bulk magneto-optic contribution of Co ($Q_{\mathrm{Co,bulk}}$) that is in accordance with literature is consistently determined despite the use of thin-films. Interfacial Co ($Q_{\mathrm{Co,int.}}$) and magnetized Pt (Q_{Pt}) contributions are presented in terms of two models. Interface phenomena of the large spin-orbit coupling between Co and Pt and the proximity induced magnetization in Pt layer are represented in the models. The strength of interfacial magneto-optic activity is interpreted as an indicator of the relative interface quality among the samples [1].

4.1 Introduction

During the 90's, vast amount of research was dedicated to study Co/Pt multilayers with perpendicular magnetic anisotropy (PMA) due to their use in magneto-optic (MO) recording media [73]. Recently, upon demonstration of novel spintronic devices that utilize the physical phenomena at heavy metal/ ferromagnetic metal interfaces [196–201], the research interest has been revived. As evidenced by the commercial product of STT MRAM [202], the fabrication processes of the multi-layered thin-films are compatible with large scale semiconductor production. Therefore, it is expected that innovative devices incorporating the multilayers will reach a technological maturity level required for large scale production, in a relatively short time. As commonly seen in the family of thin-film multilayers with PMA, Co/Pt multilayers demonstrate high chemical stability [73], enhanced MO activity [203] and tunable magnetic properties via adjustments in the fabrication processes [192] which are proven to be crucial for device applications. Considering these properties of Co/Pt multilayers and the demand for novel functionalities provided by integrated photonic devices, Co/Pt thin-film multilayers with PMA were suggested to be implemented on photonic chips for increased functionalities such as integrated photonic memory devices and optical isolators [199]. The suggested functionality relies on the interaction between confined light and a thin-film permanent magnet, which is in the vicinity. This raises an urgency to map the MO properties of Co/Pt thin-film multilayers to simulate, design and engineer novel functionalities for devices.

Assuming non-local effects [204] are not present, the MO interaction between light and the thin-film stack can be simulated for any device configuration and material stack with inputs of MO Voigt constants (Q) of magnetized layers in a multi-layered thin-film stack. The simulation can quantitatively predict the MO interaction in terms of complex Magneto-Optic Kerr Effect (MOKE), namely Kerr rotation and ellipticity. There is a large spread in the previously reported Q_{Co} values of thin-film Co. Apart from differences caused by the crystal structure type [205] and the preferred magnetization orientation, the degree of expression of the interfacial magneto-optic phenomena leads to scattered findings of Q_{Co}. Earlier works that reported the differences due to different strain states [206] and different fabrication techniques [207] of thin films indicate to this direction (see further in Sect. 4.2). We suggest that highlighting the underlying cause can bring clarity to future findings. In a quest to separate the interface and bulk activity, we unambiguously defined the bulk Q constants and assigned interface Q constants. We developed and used two optical

models that account for the MO enhancement at the Co/Pt interface. In these models, the proximity induced magnetization in the Pt layer and the large spin-orbit coupling at the interface were considered separately. The MO contributions from interface-dominated and bulk-dominated Co regions were probed experimentally using a specially designed sample set with a continuous Co thickness variation (wedge) over the samples. A typical sample deposited via DC magnetron sputtering consists of a Ta(4 nm)/ Pt(2 nm)/ Co(0-2 nm)/ Pt(2 nm) stacking, where the Co layer thickness is changed from 0 to 2 nm over a range of 15 mm. Additionally, structural effects at the interface were probed by using single and double Co-layered samples. MO constants of bulk Co ($Q_{Co,bulk}$) were determined which agreed well with literature. Using models, interfacial Co ($Q_{Co,int.}$) and magnetized Pt (Q_{Pt}) contributions were assigned to the samples. Comparing the differences in the obtained $Q_{Co,int.}$ and $Q_{Co,bulk}$ values quantitatively explains the differences in the reported Q_{Co} for thin-films. Additionally, quantitative comparison of the MO properties of Co and Pt at the interface were shown to have direct correlation with the interface quality.

This work is structured in the following way. Sect. 4.2 describes the state-of-the-art by focusing on the physical phenomena that occur on a Co/Pt multilayers with a special interest in Co/Pt interface and presents a review of the literature about previously reported Q_{Co} values (and in very few cases, Q_{Pt} values). It includes methodologies used by previous studies to pinpoint the reasons behind the vastly different MO constant findings of thin-film Co. Sect. 4.3 summarizes the methodology used in this work in three subsections. First, subsect. 4.3.1 describes the specially designed sample set, its preparation and MOKE measurement set-up. Second, subsect. 4.3.2 depicts the models that describe the magnetization profiles of Co and Pt. Third, subsect. 4.3.3 elaborates on the transfer matrix method used for multilayered thin-films to separate MO and optical effects. In Sect. 4.4, the results are presented and discussed. Lastly, in Sect. 4.5 the conclusions are given.
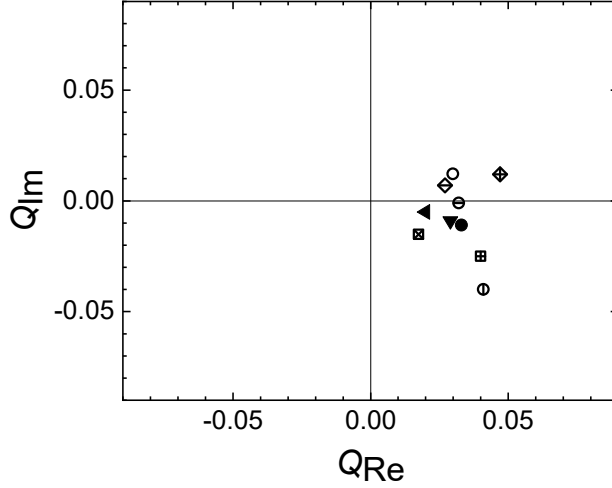
Figure 4.1: An overview of the literature reported complex Q_{Co} values. The values measured at He-Ne laser wavelength (632 nm) are presented. Details about each presented data point can be found in Table 4.1.

Table 4.1: Details of the literature findings in Fig. 1

Symb. & Ref.	Q_{Co}	t_{Co} (nm)	Crys. lattice	Magn. dir.
⊠ [208](Co_3Pt alloy)	0.0174 -0.0151i	>50	fcc-hcp	in-plane
● [207]	0.033 -0.011i	50	-	in-plane
⦶ [207]	0.041 -0.04i	0-0.85	fcc	OOP
⊞ [207]	0.04 -0.025 i	<0.4	fcc	OOP
◀ [209]	0.02 -0.005i	<1	-	OOP
⬦ [210] Co/Pt mult.	0.027 +0.007i	80	-	in-plane
▼ [73]	0.029 -0.009i	>50	fcc	in-plane
⊕ [211]	0.047 + 0.012i	0.5	fcc	OOP
⊖ [212] (Co+Pt alloy)	0.032 -0.001i	>50	-	in-plane
○ [213]	0.0299 + 0.0122i	>50	-	in-plane

4.2   State-of-the-art

In presence of a large spin-orbit interaction, the orbital moment connects the spin moment to the atomic structure of a material. For Co/Pt thin-film multilayers, the hybridization of the Co 3d and Pt 5d orbitals at the interface causes in-plane orbitals to become dominant,

thus the magnetic moment points out-of-plane (oop) [214]. Structural effects at the interface, such as interfacial roughness, intermixing, alloying, strain and dislocations [192, 215–217], are decisive for the strength of the PMA in multilayered thin films. The hybridized orbitals formed at the Co/Pt interface give rise to other physical phenomena as well: a proximity induced magnetization on Pt atoms near the interface [218, 219] and an enhancement of the Co atomic magnetic moment at the interface [220]. Similar to PMA, the strength of proximity induced magnetization is also affected by the structural effects at the Co/Pt interface [181, 221–223]. Experimental results [211, 224] supported by ab-initio calculations [225] showed that the induced magnetization in Pt rapidly decays away from the interface with a decay length of just a few tenths of a nm [226, 227]. Some works reported asymmetries in Pt layer magnetizations among top and bottom interfaces for samples that contain multiple ferromagnetic metal/Pt interfaces [181, 211, 228]. Structural asymmetry between top and bottom interfaces were held responsible for this. In addition, the total thickness of the Pt layer was shown to cause no difference in proximity induced magnetization, provided that there is no structural change at the interface due to the Pt thickness [228, 229].

MOKE indirectly probes the magnetism in a material by monitoring the allowed orbital transitions governed by the spin-orbit interaction. The preferential absorption of left- over right- handed light causes the observed MOKE signal. The signal is sensitive to changes that occur in sub-nanometer scale in electronic orbitals. Thereby, MOKE can offer valuable characterization of Co/Pt multilayers, revealing structural effects at the Co/Pt interface, at sub-nanometer scale. It has been shown that changes in fabrication method [207], as well as changes in deposition conditions of a certain method [230], can be probed by using MOKE.

Table 4.2: Sample names and corresponding material stacks

Sample name	Stack order[2 3]
Double Co on 1 nm of Pt (d1)	SiB/Ta1/Pt1/Co0-2/Pt1/Co0-2/Pt2
Double Co on 2 nm of Pt (d2)	SiB/Ta1/Pt2/Co0-2/Pt2/Co0-2/Pt2
Single Co on 2 nm of Pt (s2)	SiB/Ta1/Pt2/Co0-2/Pt2
Single Co on 3 nm of Pt (s3)	SiB/Ta1/Pt3/Co0-2/Pt3

MOKE is a cumulative effect that results from standard optical and magneto-optical phenomena. When standard optical and magneto-optical effects are separately accounted for via use of a transfer matrix method, the MO constant Q of all magnetized layer(s) can be determined. Figure 4.1 displays the literature reported Q_{Co} obtained by using MO Kerr rotation and ellipticity as inputs in the mentioned method. Insights such as sample thick-

ness, crystal lattice type and magnetization direction of the literature reported values are provided in Table 4.1. There is a large scattering in the reported values especially comparing thin-film and bulk Co (shown with filled symbols). As evident in Fig. 4.1, the Q of Co/Pt bilayers and Co thin-films are larger than that of bulk Co [210]. Previously, the differences in fabrication methods were proposed as the main reason behind the difference [207]. Some works adopted practices to separate the interfacial Co and (sometimes) the magnetized Pt contributions from that of bulk Co. Fiedler *et al.* introduced an excess Kerr rotation and ellipticity signal for each Co/Pt interface and excluded this amount while calculating Q_{Co} [207]. Some studies assigned a MO constant Q to the Pt layer. The magnetization profile in the Pt differed among these studies. Moog *et al.* assumed the whole Pt layer to be magnetized homogeneously [231], while others used a monolayer of homogeneously magnetized Pt layer with the rest being non-magnetic [232, 233]. An *in-situ* MOKE measurement taken during Pt growth on Co showed that the Pt magnetization decays exponentially from the Co/Pt interface [211]. This is found to be in accordance with proximity induced magnetization studies [219]. It is the aim of our work to apply different models to the same experimental data on a specially designed set of samples in order to establish a more unambiguous description.

Table 4.3: Complex refractive indices of materials

Material	Refractive index
Si with native oxide (subst.) [234]	$3.84 + 0.02i$
Ta [4]	$4.31 + 4.26i$
Pt [207]	$2.35 + 4.82i$
Co [207]	$2.57 + 4.14i$

4.3   Methodology

This section describes the sample set used in this study and the method of fabrication, followed by a description of the MOKE set up used for our experiments. Then, we discuss in more detail the magnetization profiles introduced in Sect. 4.3.2. Lastly, we explain the method we used to fit the Q values for the bulk and the interfacial Co, as well as the proximity induced contribution from the Pt.

4.3.1   Sample fabrication and MOKE measurement setup

The sample set used in this work is designed to distinguish the interface and bulk MO contributions. This was achieved by using wedged Co layers varying in thickness from 0 to 2 nm over a lateral extend of 15 mm. Additionally, single and double Co-layered stacks were used for comparison of the interface effects. Names and stack orders of single and double Co-layered samples are reported in Table 4.2. The samples were fabricated via computer-controlled DC magnetron sputtering at room temperature by using high purity (99.99 %) metal targets. This fabrication technique is well-established and was previously shown to result in (111) textured face-centered cubic (fcc) Co [235]. The wedged Co thickness was achieved by a knife-edge shutter which moves over the substrate and shadows it during deposition. The base pressure of the deposition chamber was kept at 10^{-9} mbar to prevent oxidation. During deposition, 10^{-2} mbar Argon (99.9999 % purity) pressure was used. The samples were grown on boron doped silicon substrates with a native oxide layer. Growth rates of the materials Ta, Pt and Co were 0.564 Å/s, 0.803 Å/s and 0.420 Å/s. MOKE measurements were performed using a red laser diode (632 nm wavelength) in a polar MOKE configuration at room temperature. Perpendicular magnetic fields were swept between $\pm$ 500 mT and hysteresis loops were gathered from which the saturation value of the Kerr effect were extracted. To increase sensitivity of Kerr rotation and ellipticity data collection, a photoelastic modulator (PEM) is used together with polarizers. A Si amplified detector detected the light intensity at the fundamental (50 kHz) and the second harmonic (100 kHz) frequency of the PEM, which correspond to Kerr ellipticity and rotation, respectively. Owing to the motor-controlled motion of the sample holder in the setup, wedged samples that have spatial variation of thickness are measured by incremental steps. The approximate FWHM of the focused laser spot was 0.2 mm, which yields a spread of 0.026 nm thickness per data point.

4.3.2   Magnetization profiles in multi-layers

In this section, the two models describing the magnetization profiles of Co and Pt in Co/Pt multi-layered thin-films are presented in more detail. Both models are derived from experimental evidence [211] and theoretical calculations [225] reported in literature. In this work we attempt to resolve which of the two models better represent the reality based on the experimental evidence. In Fig. 4.2, the magnetization profiles corresponding to the two
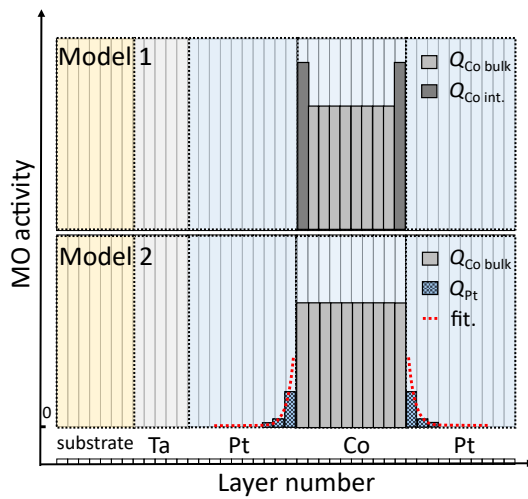
Figure 4.2: Magnetization profiles of multi-layers according to Models 1 and 2. Co and Pt monolayers are assumed to be 0.22 [236] and 0.27 [237] nm thick, respectively. Proximity induced magnetization in Pt is assumed to decay exponentially (red dashed lines) according to the Eqn. 4.1. The models are derived by using experimental and theoretical findings described in Sect. 4.2
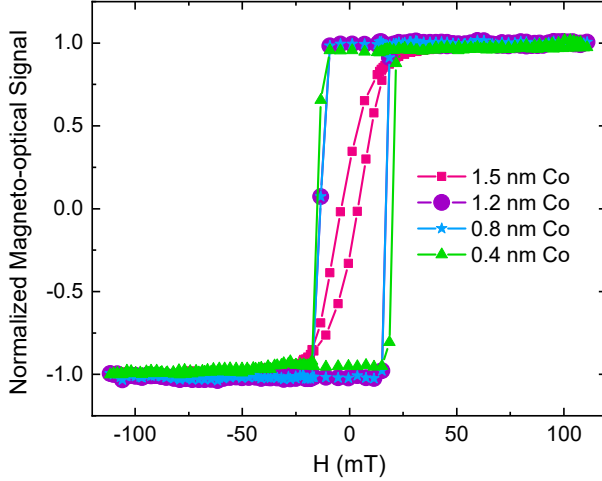
Figure 4.3: Applied magnetic field dependence of the magneto-optic signal obtained from various Co thicknesses of the sample s2. Thicknesses of 1.5 nm, 1.2 nm, 0.8 nm and 0.4 nm of Co are shown where the PMA range of the sample is from 0.4 nm to 1.42 nm. Perpendicular to in-plane transition is seen at 1.5 nm Co. The magneto-optic signals are normalized to the maximum value measured for each Co thickness.

models are sketched. Model 1 assumes that the magnetized regions of the multilayers are confined to the Co layers and the MO activity is enhanced for the first monolayer of Co at the interface with Pt (shown with $Q_{Co,int.}$ while the rest is the bulk value $Q_{Co,bulk}$). Model 2 assumes that the magnetization is homogeneous within the Co layer ($Q_{Co,bulk}$) and the neighboring Pt layers are magnetized symmetrically through proximity induced magnetization, as indicated with Q_{Pt}. As previously reported [211], the magnetization decay in Pt with respect to Pt thickness d_{Pt} is assumed to be:

$$Q_{Pt} = Q_{Ptmax}e^{-\beta(d_{Pt}-0.2)}. \tag{4.1}$$

Only Pt thicknesses above 0.2 nm are considered since a monolayer coverage is reached at this value [237]. The exponential decay constant β is 6.36 nm^{-1}, adopted from the findings of Didrichsen *et al.* monitoring in-situ MOKE. It denotes a high magnetization decay within just a few tenths of nm. $Q_{Pt,max}$ corresponds to the Q value of the monolayer of Pt which is directly adjacent to the Co. Note that as long as the numerical value of the amplitude of β is large, the precise numerical value of it has no significant effect on the resulting $Q_{Pt,max}$ value.

Therefore, we have chosen to work with previously obtained results for easier comparison. If the β amplitude is taken as infinite, which would mean that only the first monolayer of Pt is magnetized, the $Q_{\text{Pt,max}}$ value would increase approximately by 25%.

4.3.3 An optical transfer matrix method for MOKE in multi-layered thin-films

An optical transfer matrix method for determination of MOKE in multi-layered thin-films containing magnetic and non-magnetic layers has been developed by Zak *et al.* [182]. Using this method, the Kerr rotation and ellipticity from a multilayered thin-film with magnetic and non-magnetic layers can be simulated given the inputs of layer thicknesses, refractive indices, MO constant(s) of the magnetized layer(s) and angle of incidence of the incoming light. In this work, the method is used in reverse order and the MO constant(s) of the magnetized layer(s) in multi-layered samples are determined by using the experimental data (Kerr rotation and ellipticity). Assuming Co is the only magnetized layer with homogeneous magnetization resulted in $Q_{\text{Co,eff.}}$ vs. Co thickness behavior where the magneto-optic activity is enhanced at the Co/Pt interface. Therefore, the magnetization profiles described in Sect. 4.3.2 are employed and the MO constants for bulk and interfacial Co, and the magnetized Pt are determined separately. Refractive indices of each layer are given in Table 4.3. Note that the bulk Co and Pt refractive indices [234] differ slightly from the thin-film values that are used in this study.

4.4 Results and discussion

In order to separate bulk and interface contributions in Co/Pt multilayers, we performed MOKE experiments on our specially designed structures. We analyzed them by a transfer matrix method [182], using two different models to extract bulk and interface values for the respective complex Q-values.

A sample set of thin-film multilayers designed to probe the interface and bulk effects separately was used. Measuring them in a polar MOKE set-up, complex MOKE signals were obtained as a function of Co thicknesses. A magnetization state that is saturated and stable is assured for each data point in the indicated PMA window. Fig. 6.4 shows full hysteresis loops of applied H-field versus normalized magneto-optical signals for varying Co
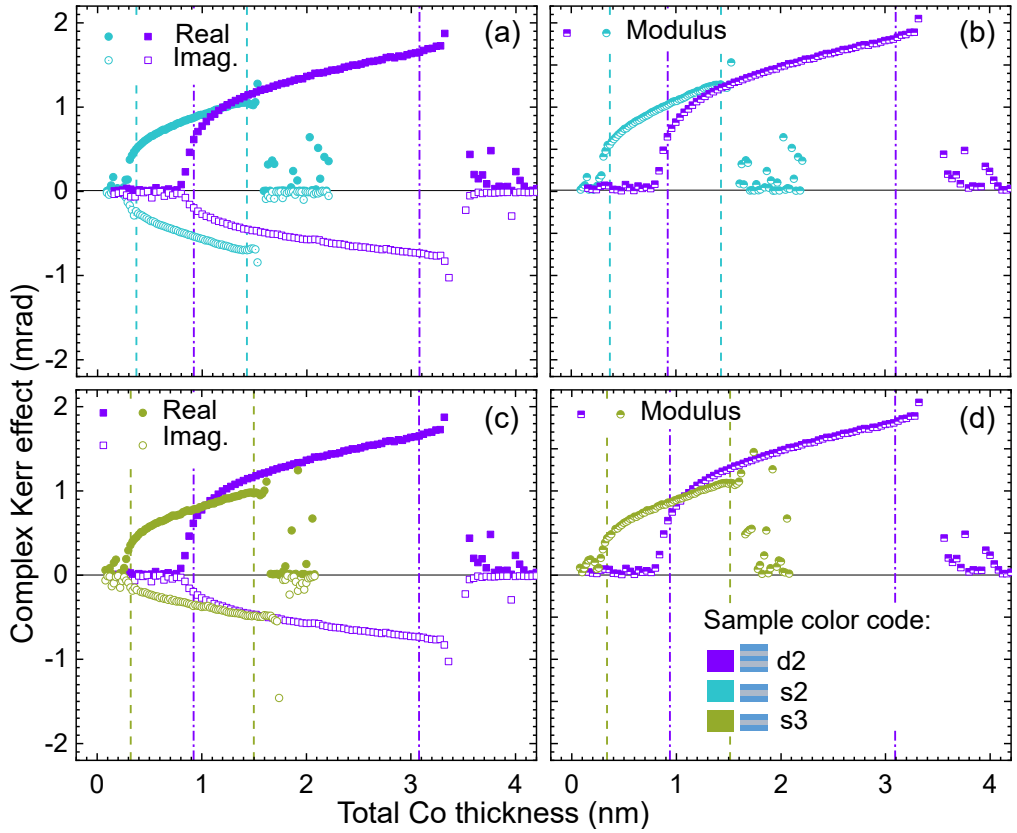
Figure 4.4: Complex polar Magneto-optic Kerr effect vs. total Co thickness (nm) behavior of the samples. **(a)** and **(c)** depict Kerr rotation (θ_K) (real) and ellipticity (ε_K) (imaginary), while **(b)** and **(d)** depict the modulus. The color-coded dashed lines frame the regions where samples show PMA. Sample color-code legend is given in the plot **(d)**. The detailed stack compositions can be found in Table 4.2.
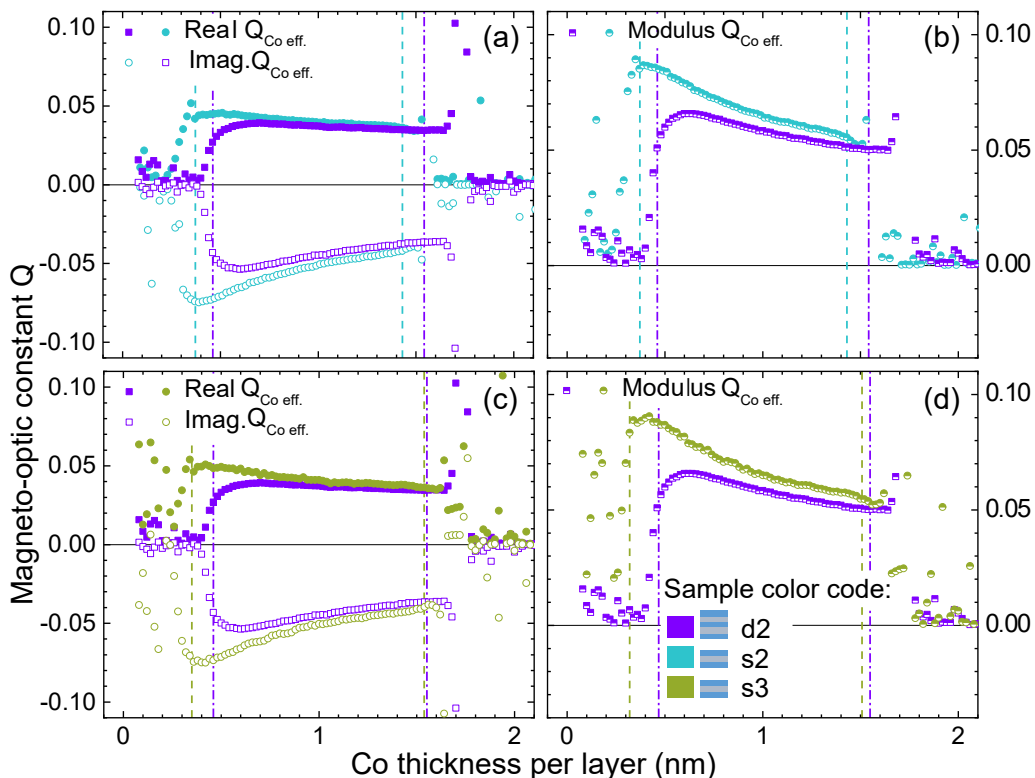
Figure 4.5: Effective Co MO constant ($Q_{Co,eff.}$) vs. Co layer thickness (nm) for different samples. $Q_{Co,eff.}$ values are found by assuming the Co is the only magnetized layer and is magnetized homogeneously. **(a)** and **(c)** show real and imaginary parts of $Q_{Co,eff.}$, while **(b)** and **(d)** depict the modulus. The color-coded dashed lines frame the regions where samples show PMA. Legend for the samples is given in the **(d)**. The detailed stack compositions can be found in Table 4.2.
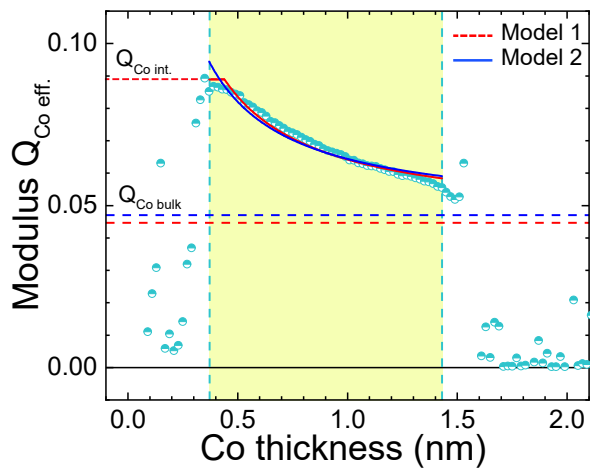
Figure 4.6: The expected behavior of $Q_{\text{Co,eff.}}$ according to the Models 1 and 2, depicted in red (dashed) and blue lines respectively. Experimentally obtained $Q_{\text{Co,eff.}}$ value is shown in half filled light blue circles. The sample chosen for this demonstration is S2 (see Table 4.2 for details). Yellow shaded area indicates the region of PMA. Horizontal blue and red dashed lines indicate interface and bulk contributions from the Co layer named as $Q_{\text{Co,int.}}$ and $Q_{\text{Co,bulk}}$.
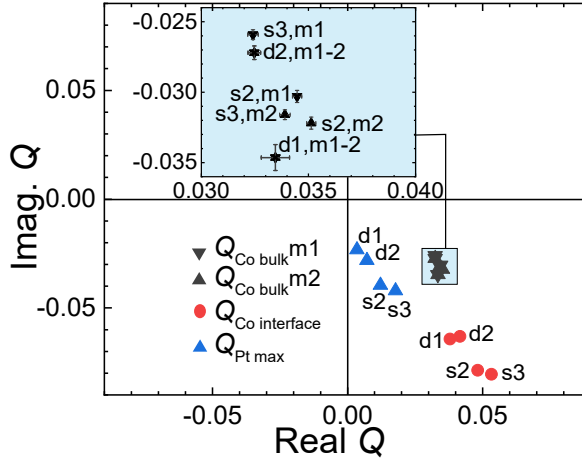
Figure 4.7: Summary of the values obtained by using the models (see Sect. 4.3.2). A zoom-in section is added in blue shaded region to show the error bars obtained from the fitting procedure. Model 1 yields $Q_{Co,bulk}$ and $Q_{Co,int}$, while Model 2 yields $Q_{Co,bulk}$ and $Q_{Pt,max}$. Each data point is labeled with the corresponding sample (s2, s3, d1, d2) and the model (m1, m2). Detailed stack orders of the samples are given in Table 4.2.

thicknesses of sample s2. The saturation ranges shown in Fig. 6.4 were used in our quantitative analysis.

In Fig. 4.4, the evolution of the Kerr signal vs. total Co thickness for the sample set with single (s2, s3) and double (d2) Co layers is shown. On the left column, real and imaginary parts correspond to Kerr rotation and ellipticity, respectively. The regions where samples demonstrate PMA are framed with color-coded vertical dashed lines. The first line indicates the completion of a closed, ferromagnet film, while the second line marks the point where the Co layer becomes too thick to sustain PMA, and the in-plane shape anisotropy takes over. It was seen that, upon reaching approximately 0.3 - 0.5 nm of single-layer Co thickness, i.e. 0.8 - 1.0 nm total Co thickness for the double-layer structure (d2), the sample has developed an OOP magnetization. This thickness corresponds well to the thickness of 2 monolayers of fcc Co oriented (111), which is 0.44 nm [236]. It was observed that upon exceeding ~1.5 nm individual Co layer thicknesses (~3.0 nm total thickness for the double layer), the magnetization turned in-plane. Expectedly, the Kerr rotation and ellipticity, thus the modulus, increase with increasing Co thickness in the PMA region, the region framed between the dashed lines.

The MOKE data shown in Fig. 4.4 were first analyzed with a simplified optical model that does not explicitly account for the Co/Pt interface phenomena. This optical model assumes that only the Co layers are magnetized and their Q values are homogeneous throughout these layers, denoted by $Q_{\mathrm{Co,eff.}}$. The resulting values of $Q_{\mathrm{Co,eff.}}$ are depicted as a function of individual Co layer thickness in Fig. 4.5. For all structures, a maximum is found near the thickness where a ferromagnetic OOP layer has developed at around 0.44 nm and a decrease is observed upon further increase in Co thickness. The strong dependence of the observed $Q_{\mathrm{Co,eff.}}$ as a function of thickness strongly suggests that at least one of the assumptions in the simplified optical model is not valid.

In Fig. 4.5, the thickness at which the maximum $Q_{\mathrm{Co,eff.}}$ is observed corresponds well with two monolayers of fcc (111) orientated Co. Hence, we conjecture that the Co/Pt interface is responsible for the increased MO activity when reducing the Co layer thickness. In order to account for the Co/Pt interface effects and map the MO activity with respect to thickness, the two optical models described in Sect. 4.3.2 were used (see also Fig. 4.2). Model 1 assumed that the Co is the only layer which contributes to the MO activity, and its activity is enhanced at the Co/Pt interface due to large spin-orbit coupling, whereas Model 2 assumed that Pt contributes to the MO activity as well via its induced magnetization due to proximity to the Co layer. As indicated via color-coded regions in Fig. 4.2, Model 1 accounts for $Q_{\mathrm{Co,int}}$ and $Q_{\mathrm{Co,bulk}}$ values separately, whereas Model 2 distinguishes Q_{Pt} and $Q_{\mathrm{Co,bulk}}$ values. We assume the respective Q values being independent of the layer thickness, and the same for each sub-layer / interface.

In Fig. 4.6 a simplified picture of the fitting procedure is shown indicating the asymptotes of $Q_{\mathrm{Co,bulk}}$ for Models 1 and 2 and $Q_{\mathrm{Co,int.}}$ for Model 1. The results obtained by the exemplified fitting procedure are depicted in Fig. 4.7. Each data point is tagged with the sample name and the model (See Table 4.2). The error margins of the fitting procedure are included in the graph, albeit only visible at the blue-shaded zoom-in section. The two models yield slightly different $Q_{\mathrm{Co,bulk}}$ values. The extracted Q_{Pt} and $Q_{\mathrm{Co,int}}$ values were found to be grouped in two clusters of data-points, corresponding to single and double Co-layered samples. These clusters were speculated to be due to the difference in the Co/Pt interface quality. Since addition of each layer contributed to the roughness, the single Co-layered samples were expected to have smaller interface roughness than the double ones. Consequently, the single Co-layered samples showed greater amplitudes of $Q_{\mathrm{Co,int}}$ and $Q_{\mathrm{Pt,max}}$. Works presented in the state-of-the-art section support this conclusion as they mentioned the microscopic ordering at the interface affects the spin-orbit coupling strength and the

degree of proximity induced magnetization in the Pt layer [181, 222]. Additionally, an interface asymmetry between top and bottom Co/Pt interfaces which causes only the bottom Pt layer to be magnetized should be considered as it was previously observed [228]. In this respect it can be argued that the Co layers grown on rougher Pt layers (double-layered Co samples) show more disorder which prevents the induced magnetization in the Pt layer. One can argue that the quantitative comparison of the obtained Q_{Pt} and $Q_{\mathrm{Co,int}}$ values between samples s2 and s3 (as well as d1 and d2) suggests that the thicker Pt layers (in the range of 1-3 nm) contribute to smoother and well-defined Co/Pt interfaces, and increases the amplitude of Q_{Pt} and $Q_{\mathrm{Co,int}}$ for sample s3 (as well as d2). As seen in Fig. 4.5 (b) and (d), the earlier PMA onset and the broader thickness window of PMA in sample s3 with respect to s2 supports the argument that sample s3 has sharper interface. However, further studies on Pt thickness vs. roughness are required before concluding.

Comparing quantitatively, the average bulk Co MO constant $Q_{\mathrm{Co,bulk}}$ of 0.033 - 0.030i is found to be in good agreement with the literature values [207, 208], albeit with a larger amplitude of the imaginary component. This difference was inferred to be due to structural differences between used samples. In literature reported cases, annealed bulk samples (thickness larger than 50 nm) of fcc (111) oriented epitaxial Co with in-plane magnetization were used. Continuing the quantitative comparison with the Pt MO constant, the average $Q_{\mathrm{Pt,max}}$ value of 0.0102 - 0.0333i reported in our work is smaller than what has been reported in literature [211, 231–233]. It should be stressed that a quantitative comparison for Q_{Pt} was not straightforward. To our knowledge, the amount of studies reporting Q_{Pt} values is limited to a few. Additionally, the profile of the induced magnetization in the Pt, decaying away from the interface, differed among the reports. To exemplify, Didrichsen *et al.* used a decaying magnetization in Pt, supported by *in-situ* MOKE. Lee *et al.* [233] and Train *et al.* [232] assumed a homogenous magnetization in Pt that is only present at the first monolayer at the Co/Pt interface. Since thicknesses of the magnetized Pt layers differed among studies, we based the comparison on the integral MO effect. As a result, the Pt layer contribution in our samples are found to be smaller than the literature reports.

It is also interesting to compare the obtained Q_{Co} with Q_{Pt} values and the theoretical (ab-initio) predictions by Reichl *et al.* [225], although the structural differences between the analyzed Co/Pt multilayers of the two works should be kept in mind. More specifically, the ab-initio work simulated Co/Pt layers where Co is epitaxially grown on (111) oriented fcc Pt while the samples used in our study are polycrystalline, textured in the (111) direction. Nevertheless, the strong first-monolayer Q_{Pt} contribution at the Co/Pt interface predicted

by the ab-initio work signaled the importance of a sharp interface for high Q_{Pt}. This is in line with our findings of larger Q_{Pt} contribution in single Co-layered samples where interface roughness is smaller.

Lastly, a discussion on which one of the two models better describe the physical picture at the Co/Pt interface is presented. As seen in Fig. 4.6, the predictions of the two models differ greatly at the region framed between the minimum thickness for exhibiting PMA and the 2 monolayers thickness of Co. We refer to this region as the indicator region. Note that in case the minimum Co thickness required for PMA is thicker than 2 monolayers of fcc (111) Co (0.44 nm), the indicator region lies outside of the extend of PMA, thus an evaluation becomes unreliable. This is the case for samples with double Co layers (d2 and d3) as the increased interface roughness pushed the PMA onset to a greater thickness in these samples. Focusing on a single Co layer sample s2 as seen in Fig. 4.6, at the indicator region (0.37-0.44 nm), Model 1 seems to describe the experimental observation slightly better than Model 2. However, the following points should be considered before concluding. As described in Sect. 4.2, the proximity induced magnetization in the Pt layer requires a certain interface magnetization threshold to be induced as previously shown by Inyang et al. [181]. Therefore, prior to the formation of two complete Co monolayers (0.44 nm), an induced magnetization in the Pt layer may remain absent which yields the observed behavior in Fig. 4.6. Additionally, in the indicator region the ferromagnetic order is being established, thus the thickness dependent electronic effects and thermal activation effects are convoluted. Therefore, we argue that the actual physical picture at the interface is a combination of both models.

4.5 Conclusions

We demonstrated enhancement of the MO activity at Co/Pt interface by using a sample set that is designed to probe the interface effects. We discussed that the vast scattering of Q_{Co} values reported in literature for thin-film Co samples are due to inclusion of interfacial Co and Pt contributions. We assigned interfacial Co ($Q_{Co,int.}$) and magnetized Pt (Q_{Pt}) magneto-optic constants by using models. And consistently determined bulk Co ($Q_{Co,bulk}$) values. Via the methodology described in this work we showed that, even when Co thin-films (2 nm) are used, bulk Co MO constant ($Q_{Co,bulk}$) values that are in good agreement with literature can be obtained. Additionally, we presented a discussion that a quantitative comparison of the resulting $Q_{Co,int.}$ and Q_{Pt} from different stacks can be used to deduce

information regarding the relative interface qualities of these samples. More specifically, this might be of particular interest where more conventional methods like X-Ray Reflectivity (XRR) fail to differentiate samples in terms of interface quality due to lack of contrast. However, it would be worthwhile to conduct studies where XRR and MOKE are quantitatively compared and calibrated before relying on MOKE for interface characterization.

Chapter 5

Design and modelling of a novel integrated photonic device for nano-scale magnetic memory reading

Design and simulations of an integrated photonic device that can optically detect the magnetization direction of its ultra-thin (~12 nm) metal cladding, thus 'reading' the stored magnetic memory, are presented. The device is an unbalanced Mach Zehnder Interferometer (MZI) based on the IMOS platform. The MZI consists of a ferromagnetic thin-film cladding and a delay line in one branch, and a polarization converter in the other. It quantitatively measures the non-reciprocal phase shift caused by the Magneto-Optic Kerr Effect in the guided mode which depends on the memory bit's magnetization direction. The current design is an analytical tool for research exploration of all-optical magnetic memory reading. It has been shown that the device is able to read a nanoscale memory bit (400 × 50 × 12 nm) by using a Kerr rotation as small as $0.2°$, in the presence of a noise ~ 10 dB in terms of signal-to-noise ratio. The device is shown to tolerate performance reductions that can arise during the fabrication[1]

---

[1]This chapter has been published in Journal of Applied Sciences [49].

5.1 Introduction

In the modern world, exponentially increasing generation of data and its handling require novel technologies that perform faster and more energy efficiently. To answer this need, optical components are being used in combination with electronic circuitry to improve the speed and bandwidth of data communication and telecommunication. For example, optical interconnections that were once a conceptual design suggestion [238] are currently being used in commercial products replacing slow and heat-dissipating electrical signal communication channels [239, 240]. Researchers continue to demonstrate the superior performance circuitry achieved through the integration of photonics into electronics [30, 241–243]. Yet, these advances require back-and-forth signal conversion between optical and electrical domains, which happens to be the new bottleneck in data communication and processing. Addressing this problem requires establishing novel functionalities in photonic devices that will enable a seamless conversion. Furthermore, (integrated) photonics is lacking a simple and fast non-volatile memory function. A huge potential is anticipated for future devices that enable direct inter-conversion of data between the photonic and magnetic (memory) domain without any intermediate electronics steps, cutting down on time and energy costs. This study works with existing non-volatile magnetic memory material technology used in electronics: multilayered ferromagnetic thin-film layers. When the multilayered magnetic material is used as memory material, writing bits into the magnetic memory could be facilitated by recent advances in so-called all-optical switching of magnetization [104, 244]. Reading out magnetic bits back into the photonic domain could be achieved via a nonreciprocal magneto-optical process [66, 175, 245], while dynamic, on-the-fly reading of magnetic bits could be facilitated by a racetrack memory concept [57, 244]. In a racetrack memory, magnetic domains (memory bits) move while the material that carries the magnetic domains remain stationary [246, 247]. Previously, domain wall velocities up to 1000 ms^{-1} were demonstrated [248, 249]. It is in this spirit that our research focuses on the functionality of on-chip optical reading of magnetic memory processed as ultrathin magnetic claddings on photonic waveguides. To our best knowledge, this is the first study which explores the possibility of on-chip, all-optical magnetic memory reading functionality.

State-of-the-art non-volatile magnetic memory such as spin-transfer torque magnetic random-access memory (STT-MRAM) relies on ferromagnetic multilayered ultrathin films with perpendicular magnetic anisotropy (PMA), in which the magnetization vector is per-

pendicular to the film plane [250]. Such PMA films turn out to be essential for the advanced schemes used to electrically control the magnetic memory elements, but are also known for their relatively large magneto-optical efficiency. A simple layer stack that hosts all relevant physical mechanisms is Ta(4)/Pt(2)/Co(1)/Pt(2)/Co(1)/Pt(2) where the numbers in parenthesis are the thickness in nm. Bringing this memory component to the proximity of light confined in a waveguide in a photonic device setting gives rise to magneto-optic interactions, specifically the Magneto-optic Kerr Effect (MOKE). MOKE causes a change in the polarization state of light (Kerr rotation and ellipticity), which changes sign when the magnetization direction of the memory component is flipped [66, 175]. In a photonic waveguide context, this gives rise to partial mode conversion between TE and TM modes, which potentially enables reading of the memory bit. However, the MOKE signal is intrinsically small in amplitude, a typical Kerr rotation is around $0.05°$ for films with an in-plane magnetization in free-space optics [207, 209]. In order to increase the efficiency of the mode conversion, we propose the use of PMA magnetic claddings, which have not been seriously addressed yet in a photonic perspective. Such claddings with a perpendicular magnetic orientation are expected to display larger amplitude magneto-optical effects, yet still small quantitatively. This calls for developing novel approaches to amplify the magneto-optical effects while showing the importance of on-chip analytical tools to explore the fundamental mode conversion properties of photonic waveguides with PMA claddings.

To assess the feasibility of using MOKE for on-chip all-optical magnetic memory reading functionality, as well as using it as an analytical tool to quantitatively measure magnetization-induced mode conversion, we investigated specially designed photonic devices whose waveguides are cladded with ultra-thin (12 nm), nano-scale (50 × 400 nm) PMA magnetic memory bits, of the composition mentioned before. By using mathematical models of the designed photonic devices, whose building block performance parameters are chosen according to the InP Membrane on Silicon (IMOS) platform [251], the accuracy of the memory-bit readout, optical loss and tolerance to noise are tested. It has been shown that the device is able to read a nanoscale memory bit (400 × 50 × 12 nm) by using a Kerr rotation as small as $0.2°$, in the presence of a ~ 10 dB noise in terms of signal-to-noise ratio (SNR). This chapter is structured in the following way. In Section 5.2 materials and methods are given. Device designs, magneto-optic simulation, mathematical modelling and data analysis topics are covered. In Section 5.3 the results obtained via the mathematical model are presented for devices with varying degrees of performance parameters. A data analysis technique using Fourier transformation is presented. Lastly, in Section 5.4, the conclusions are given.

5.2   Materials and Methods

In this section, materials and geometries of the parts that contribute to the overall device are explained. In addition, the device concept, optical simulation and mathematical modelling methods are explained in the subsections.

The material which stores the magnetic information (memory bit) is a multi-layered ferromagnetic metal thin-film structure, whose stack order is given in the previous section. These multi-layers display PMA, where the magnetization vector is perpendicular to the film plane [252]. PMA is highlighted due to its relatively large magneto-optical efficiency [253]. The multi-layers are placed on top of the waveguides as the top cladding. The rest of the photonic device is fabricated on InP membranes since the devices are based on the IMOS platform [251]. The waveguides have a cross-section of 300×400 nm (height and width) and the multi-layered top claddings have the dimensions of $400 \times 50 \times 12$ nm (width, length and height).

5.2.1   Optical Simulation and Device Concept

Before describing the optical simulation method to quantify the MOKE in waveguides, a brief overview is given on MOKE and its impact on the light confined in waveguides. Following this, the devcie concept is introduced.

MOKE is a type of magneto-optic interaction that takes place when the light reflects from a magnetized material. In polar configuration, the effect causes a change in the light's polarization state which is quantified by Kerr rotation and ellipticity (in angles). Typically, in the literature, MOKE is reported for single reflections. Comparing a single reflection case with our work, more interaction, thus a larger MOKE are expected in waveguides with magnetized top claddings. To our best knowledge, there is no prior work that quantifies the Kerr rotation in a waveguide setting. Therefore, finite-difference time-domain (FDTD) simulations [254] of the waveguides with top-claddings are conducted to estimate the MOKE in the guided modes. In the simulation, multi-layer cladding material is defined by using the magneto-optic constant obtained from the literature [210]. It is seen that the Kerr effect causes conversion between TE and TM modes in the waveguide, comparable to the polarization rotation in free-space optics. The resulting Kerr rotation (θ), ellipticity (ϕ) and optical loss ($Loss_{clad.}$) values obtained for a single memory bit are listed in Table 5.2. These values are used as inputs for the mathematical model explained in Section 5.2.2.

The device design is done by considering the key enabler of the magnetic memory reading functionality: a change in the sign of the Kerr rotation upon flipping of the magnetization direction of the memory bit (memory bit $'1'$ and $'0'$). Assuming the confined light is initially in TE mode, the Kerr rotation $\pm\theta$ ($\theta \ll 1$) leads to an emergent TM mode whose field amplitude is proportional to $\pm\theta$ (same result for bit 1 and bit 0). Therefore, instead of probing the field amplitude, devices which can probe the phase of the emergent TM mode are explored. Mach-Zehnder Interferometers (MZI) are chosen due their ability to convert the phase difference (between the interfering branches) into intensity difference. Balanced and unbalanced MZI are considered as two candidates for the final design. An unbalanced MZI, which has a defined path length difference between the two branches, is chosen due to the noise related issues that cannot be addressed in a balanced MZI. This is further elaborated when the presented results are discussed in Section 5.3. Since at an initial stage, a device is designed for research and exploration purposes, on-chip light source or detector are not considered. To couple an off-chip laser source and an off-chip detector to the device, mode-selective grating couplers are added to the design.

The device design is shown in Figure 5.1. In this device, TE mode-selective grating coupler is used to couple the light in. Later, a multi-mode interferometer (MMI) is used to split the light equally into two branches. On the upper branch, the TE mode is converted into TM via the polarization converter. The propagation continued (in TM mode) and a delay line is crossed. On the lower branch, the memory bit (magnetic cladding section) caused the TE mode to partially convert into TM mode due to Kerr rotation (θ). The light from the two branches are merged via another MMI. After interference took place, the resulting intensity is picked up via a TM-selective grating coupler.
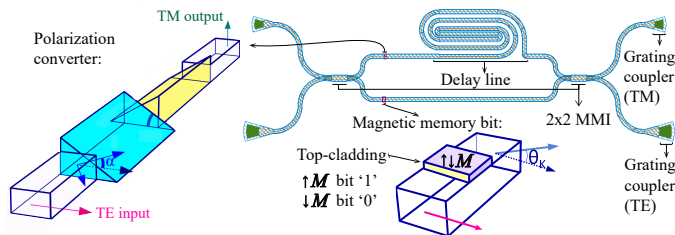
Figure 5.1: An unbalanced MZI. TE and TM mode selective grating couplers are used to couple the light in and out. The polarization converter is taken from [140].

5.2.2   Mathematical Modelling and Fourier Transformation

A mathematical model is built in order to simulate the output light intensity vs. light wavelength for the designed devices. The model uses input parameters that are based on IMOS building block performances [251] and FDTD magneto-optical simulations [254] (see Section 5.2.1). An overview of the model parameters and their brief descriptions are given in Table 5.1. Additionally, reduced-performance devices with and without noise are simulated with the model to compare the magnetic memory reading capabilities of the devices. These parameters—some standard for all devices and some changing according to the performance levels—are summarized in Tables 5.2 and 5.3, respectively.

Using the mathematical model, equations which determine the electric field (E-field) components of TE and TM modes in branches 1 and 2, are obtained. For simplicity, coefficients addressing the losses of mode propagations, grating couplers and magnetic cladding are combined into the terms B_n. For description of other parameters please refer to Table 5.1.

$$
\begin{aligned}
E_{\text{TE},1} &= B_1 \cos(\alpha) \, e^{-i\frac{2\pi}{\lambda} n_{\text{TE}} L_1} \\
E_{\text{TM},1} &= B_2 \sin(\alpha) \, e^{-i\frac{2\pi}{\lambda} n_{\text{TM}}(L_1 - x_{\text{PC}})} \\
E_{\text{TE},2} &= B_3 \cos(\theta) e^{-i\frac{2\pi}{\lambda} n_{\text{TE}} L_2} \\
E_{\text{TM},2} &= B_4 \sin(\theta) e^{-i\left(\frac{2\pi}{\lambda} n_{\text{TM}}(L_2 - x_{\text{clad}}) + \phi\right)}.
\end{aligned}
\tag{5.1}
$$

Table 5.1: Overview of model parameters.

Parameters	Definitions
λ	Wavelength scanned (nm)
$Loss_{wg}$	Waveguide propagation loss (assumed to be the same for TE and TM)
n_{TE}	Effective index of TE mode
n_{TM}	Effective index of TM mode
L_1	Length of the upper branch (μm)
L_2	Length of the lower branch (μm)
x_{PC}	Distance between polarization converter and left-hand side MMI splitter (μm)
$x_{\text{clad.}}$	Distance between memory bit (cladding) and left-hand side MMI splitter (μm)
$Loss_{clad.}$	Loss due to memory bit (cladding)
$Loss_{GC_{\text{TE}\rightarrow\text{TE}}}$	Loss of TE-selective grating coupler for TE mode (dB)
θ	Kerr rotation
ϕ	Kerr ellipticity
α	Angle representing the polarization conversion (degree)
$Loss_{GC_{\text{TM}\rightarrow\text{TM}}}$	Loss of TM-selective grating coupler for TM mode (dB)
$Ext_{GC_{\text{TM}\rightarrow\text{TE}}}$	Extinction ratio of TM-selective grating coupler for TE mode (dB)
Noise	Addition of a Gaussian distribution of random noise to the intensity

It is important to recall that the interference takes place between the modes whose E-fields are parallel planes and the output light intensity (I) from devices can be calculated via $I = \dfrac{|E|^2}{2Z_0}$, where $|E|$ is the total E-field amplitude and Z_0 is the impedance of the vacuum. The presented equations for E-field amplitudes reveal that a wavelength sweep of the input light will result in oscillations in intensity.

Recall that the information regarding the magnetization direction of the cladding (memory bit type) can be retrieved from the sign of the Kerr rotation and ellipticity (θ, ϕ). As seen from the equations above, when TE mode input light is used, information of the memory bit type is visible only in the phase of the TM mode output light. For an output light intensity vs. wavelength plot that is obtained upon interference of both TE and TM modes, two oscillation frequencies, v_{TE} and v_{TM} that correspond to these modes are observed.

$$v_{\text{TE}} = \frac{n_{\text{TEg}}(L_1 - L_2)}{\lambda^2},$$
$$v_{\text{TM}} = \frac{n_{\text{TMg}}(L_1 - L_2 + x_{\text{clad.}} - x_{\text{PC}})}{\lambda^2}. \tag{5.2}$$

n_{TEg} and n_{TMg} in Equation (5.2) indicate group indices of the respective modes. A Fourier transformation can be applied to the resulting output light intensity vs. wavelength data

Table 5.2: Generic parameters that are valid for all devices.

Parameter	Value
λ	1465–1495 nm
$Loss_{wg}$	3 dB/cm
n_{TE}	2.012
n_{TM}	1.809

Parameter	Value
L_1	1386 µm
L_2	462 µm
x_{PC}	200 µm
x_{clad}	100 µm

Parameter	Value
$Loss_{clad.}$	0.13 dB/50 nm
$Loss_{GC_{\text{TE}\rightarrow\text{TE}}}$	1.5 dB
θ	$\pm 0.2^{\circ}$
ϕ	$\pm 0.2^{\circ}$

Table 5.3: Showing parameters that are dependent on the device performance.

Parameter	Standard Device	Reduced Performance	Noise + Reduced Performance
α	90°	45°	45°
$Loss_{GC_{\text{TM}\rightarrow\text{TM}}}$	1.5 dB	7 dB	7 dB
$Ext_{GC_{\text{TM}\rightarrow\text{TE}}}$	50 dB	28 dB	28 dB
Noise	none	none	10.7 dB (SNR)

to separate the TM mode contribution. Thanks to this technique, the amplitude and phase of the TM mode component can be found. In order to separate the TE and TM mode contributions, non-overlapping peaks in the Fourier transform are required. Therefore, at the design stage, it is vital to choose x_{clad} and x_{PC} parameters (see Table 5.1) accordingly.

5.3   Results and Discussion

In order to demonstrate the magnetic memory reading capabilities of our devices, the mathematical model described in Section 5.2.2 was used. As explained in Section 5.2.1, the chosen devices were unbalanced interferometers that contain built-in ferromagnetic memory components as their top claddings. The model predicted the output light intensity vs. wavelength plots of the devices with opposing memory bits (bit '1' and '0'). Later these plots were analyzed by the Fourier transformation technique to determine the memory bit type, thus realize 'reading' of the magnetic information. Recall that since the magneto-optic interaction which enables the determination of the memory bit type is only extractable from the phase of the TM mode (when TE mode is used as input), The Fourier analysis greatly reduces the noise and enhances the sensitivity.

In Figure 5.2, the left column plots present output light intensity vs. wavelength data. Note that plots depict the intensity after a windowing function is applied. The right column plots show the Fourier transformation of the left column in blue color and the phase difference between two memory bit states for each oscillatory component in red color. Figure 5.2a,c,e represent the standard, reduced-performance and noisy reduced-performance devices, respectively. The standard device shown in Figure 5.2a demonstrate a clear $180°$ phase shift between the two signals which correspond to the opposite memory states. The Fourier transformation in Figure 5.2b (right side y-axis) show a single peak which correspond to the TM mode (see Equation (5.2)). The fact that there is only TM mode is thanks to the well-performing TM-selective out-couplers in the standard devices that have a negligible out-coupling of the TE mode. As expected, the phase difference plot in Figure 5.2b (left side y-axis) indicate $180°$ difference at the region which correspond to TM peak. Note that the plots depicting phase difference between two memory states convey meaningful information only at the locations where a correspondent Fourier peak is present. To stress this aspect visually in the graph, the points corresponding to a peak are shown in black, whereas the rest is left grey. In Figure 5.2c, the 'reduced-performance device' is seen. This device has only $45°$ conversion at the polarization converter and the TE-mode couples out from the TM-selective out-coupler (see Table 5.3). Due to coupling out of the TE mode that does not carry information on the memory bit's state, it impossible to observe a $180°$ phase shift in the intensity vs. wavelength plot upon a change in the memory bit type. As expected, Figure 5.2d reveals two Fourier peaks that correspond to TE and TM modes. As seen from the peak intensities, despite the use of TM-selective out-couplers, the TE mode dominates.

Undeterred by the TE mode dominance, the phase difference plot in Figure 5.2e indicates a phase of $180°$ at the position corresponding to the TM peak. The phase shift corresponding to the TE mode reads $0°$. Testing the device design further by addition of a noise as described in Section 5.2.2, Figure 5.2e,f are obtained. The 'noisy and reduced-performance device' demonstrates that, even though the intensity vs. wavelength plot is dominated by noise and mixed modes, it is still possible to determine the magnetic memory type via the Fourier transform technique.

Referring back to Section 5.2.1 and clarifying the reason for the choice of an unbalanced MZI design over a balanced one, as seen in Figure 5.2a, if the device is performing at a fixed wavelength, the change in the light intensity upon changing the memory bit type corresponds to only 0.3% of the total light intensity. This observation indicates that the magnetic memory reading functionality of the device can be obstructed by the noise when operating at a single wavelength. Sweeping of a range of wavelengths accompanied by the Fourier transformation method are the key concepts for eliminating sensitivity to noise and increasing memory reading accuracy. Since the wavelength sweep technique is not successful without the specific frequency oscillations that the added delay line provides, an unbalanced MZI is preferred over a balanced one.

Note that for an ideal device depicted in Figure 5.2a, the difference in light intensity between the two memory states is proportional to the strength of the Kerr rotation. Therefore, if a calibration by using a material with known Kerr rotation and optical loss is done, very small Kerr rotations can be measured quantitatively by using the same design.
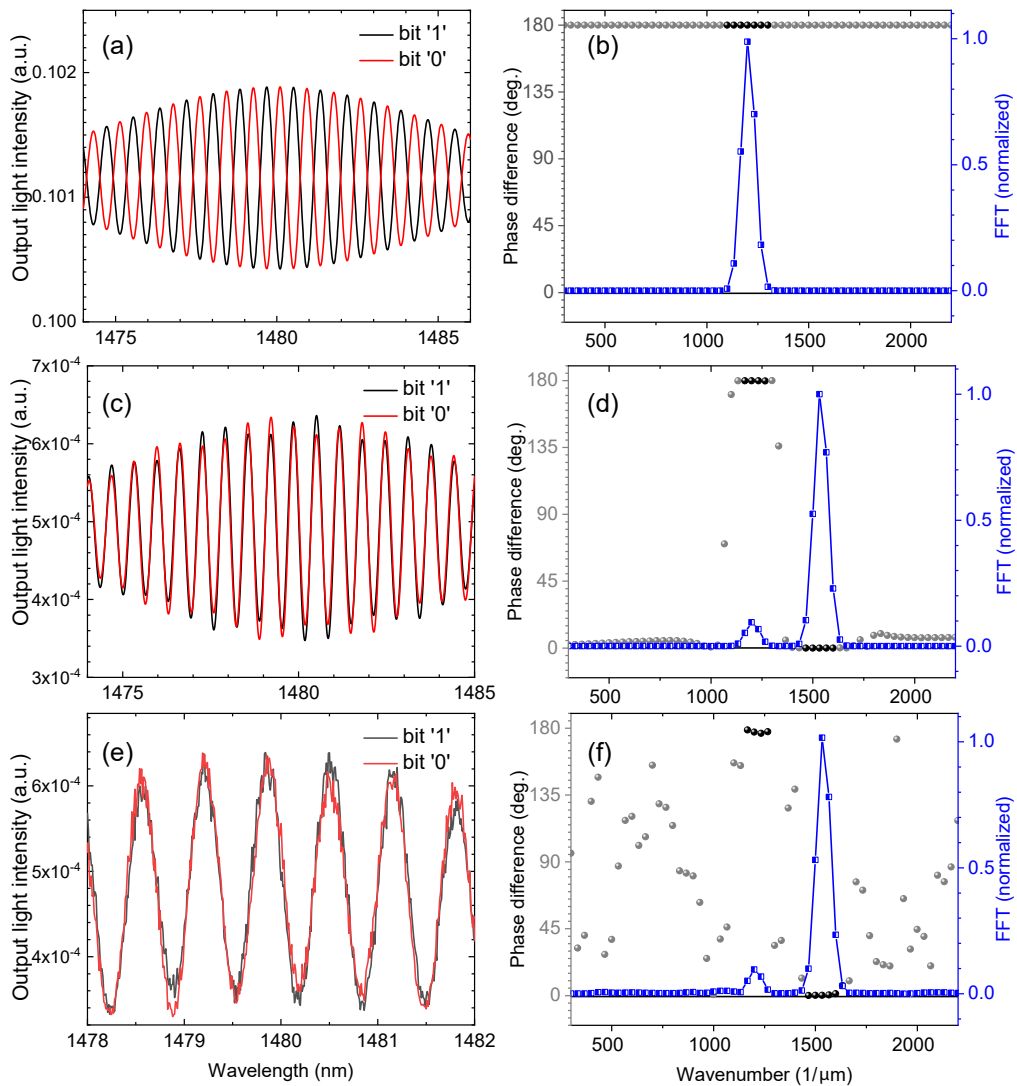
Figure 5.2: (**a,c,e**) Output light intensity vs. wavelength plots for standard, reduced-performance, and noisy reduced-performance devices (see Tables 5.2 and 5.3), The light intensities are shown in arbitrary units and is normalized assuming initial intensity (I_0) is 1. (**b,d,f**) In blue, Fourier transformations of the intensity vs. wavelength plots are shown. The normalization is done assuming the highest intensity Fourier peak has amplitude 1. In black, the phase differences between the memory bit "1" and "0" are shown for each wavenumber. The data-points which correspond to a Fourier peak are shown in black while the rest is shown in grey. This is done for guidance to eye for separation of statistically significant result (black) and fitting procedure noise (grey).

5.4 Conclusions

An integrated photonic device specially designed to perform memory reading functionality is presented. The functionality is achieved through detection of the magnetization direction of an ultra-thin memory bit. The device is shown to operate despite performance reductions in the contributing building blocks and noise levels which correspond to ~10 dB in terms of SNR. Post-processing of the intensity signal via Fourier transformation method stressed that the device is suitable as an analytical tool for research purposes. It is highlighted that the quantitative measurement of very small magneto-optic Kerr rotation ($0.2°$) is possible after a calibration which also considers optical loss.

Chapter 6

An integrated photonic device for on-chip magneto-optical memory reading

This study presents the design, fabrication and experimental demonstration of a magneto-photonic device that delivers non-volatile photonic memory functionality. The aim is to overcome the energy and speed bottleneck of back-and-forth signal conversion between the electronic and optical domains when retrieving information from non-volatile memory. The device combines integrated photonic components based on the IMOS platform and a non-volatile, built-in memory element (ferromagnetic thin-film multilayers) realized as a top-cladding on the photonic waveguides (a post-processing step). We present a design where the phase of the guided light is engineered via two mechanisms: the polar MOKE and the propagation in an asymmetrical cross-section (triangular) waveguide. Thanks to its design, the device yields different mode-specific transmissions depending on the memory state it encodes. We demonstrate the recording of the magnetic hysteresis using the transmitted optical signal, providing direct proof for all optical magnetic memory reading using an integrated photonic chip. Using mathematical model and optical simulations, we support the experimental observations and quantitatively reproduce the Kerr signal amplitudes on-chip. A 1% transmitted power contrast from devices is promising indicating that in a shot noise limited scenario the theoretical bandwidth of memory read-out exceeds 50 Gbits/s [1]

---

[1]Apart from the outlook section, this chapter has been published in Nanophotonics Journal [255].

6.1 Introduction

Our modern-day civilization consumes and generates data at an exponentially increasing rate, demanding an ever-growing computational power and bandwidth. This fuels the technological advancements towards faster, cheaper and more energy efficient operations. As previous research shows [9, 25, 256, 257], incorporating integrated photonics with electronic circuitry offers a drastic performance increase in data-com and tele-com. Yet, new bottlenecks form at points of signal conversion between the electronic and optical domains. For certain operations, the electronic and optical circuitries have varying performance levels, which implies that using conversions between the two domains (electronic and optical) is a requirement for improving the overall system performance. To exemplify, certain applications leverage the faster signal-transfer in the optical domain by using photonic interconnects, while the memory-related tasks such as storage and read/write operations still take place in the electronic domain [258]. Especially in data centers and neural network training operations, for which a frequent non-volatile memory retrieval is required [259], we anticipate a huge potential when using all-optical operations, cutting down on intermediate electronics steps, saving time and energy. To unlock this potential, integrated photonic components that deliver optical memory functionality through various different mechanisms have been suggested [156, 260, 261]. However, photonic memory alternatives are currently outperformed by their electronic counterparts. Considering the high storage density of conventional magnetic non-volatile memories and their well-established wafer-scale production capabilities, we believe that it is a strategical next-step to invest in the field of integrated magneto-photonics. Since light and conventional magnetic memory materials interact magneto-optically [66] and yield a distinct signal depending on the memory state, such materials can be candidates for an optical memory in integrated photonic circuits. Regarding the interaction of light with the magnetic memory materials, there are ongoing efforts on establishing all-optical switching of spintronic memory bits that are based on films with Perpendicular Magnetic Anisotropy (PMA) [104, 199, 262–264]. The reported experimental evidence is mostly based on free-space optics, except one study that proposed all-optical memory writing of non-volatile Magnetic Random-Access Memory (MRAM) in an integrated photonic device setting [110]. Despite these developments, to our knowledge, there is no study focusing on the magneto-optical reading of the magnetic memory using a hybrid integrated photonic device that implements magnetism into the picture. Considering these factors, we aimed to demonstrate a proof-of-principle device that combines the

fields of spintronics and photonics to deliver an on-chip magneto-optical memory reading functionality.

Our proposed magneto-photonic device carries a built-in, non-volatile, nano-scale magnetic memory bit that is applied to its waveguide as a top-cladding. The cladding is a ferromagnetic, multilayered ultrathin-film (total thickness of 12 nm) containing Co/Pt layers with PMA [73]. Our choice for this system is motivated by the aforementioned combination of relatively large magneto-optical effects, the availability of efficient all-optical switching scenarios and PMA magnetic thin film systems being the preferred system in todays spintronics. As to the latter, materials with PMA dominate the non-volatile memory applications, such as spin-transfer torque (STT) MRAM, thanks to their increased memory density and thermal stability [265]. Although state-of-the-art PMA structures have been shown to interact with optical pulses to store information in magnetic memory [264] and are known for their relatively large magneto-optical efficiencies, they have not been explored for optical memory applications yet. The working principle of our magneto-photonic device for delivering the magneto-optical memory reading functionality is the polar Magneto-Optical Kerr Effect (polar MOKE) which takes place when the guided light interacts with the PMA top-cladding [266]. While MOKE by metallic magnetic claddings in longitudinal and transverse configurations has been well investigated [48, 165], the potential for this polar configuration has been overlooked to date.

The fabricated device has its photonic components based on the InP Membrane On Silicon (IMOS) platform [32], where the way of confinement of light within the InP membrane ensures a strong interaction between the light and the magnetic cladding. In this setting, MOKE causes a change in the polarization state of the guided light, which changes sign when the magnetization direction of the memory component is reversed [175]. In a photonic waveguide, this gives rise to a partial mode conversion between the TE and TM modes, where the phase of the emergent mode carries the information about the magnetization direction of the cladding, thus its memory state. More specifically, in the case of a TE mode partially converted into TM mode, the relative phase of the modes will change by π (180°) upon reversal of the magnetization direction. Considering that the information is stored in the phase of the guided light, we propose a novel device design where the change in polarization state is converted to an intensity contrast. Additionally, such a device can be used to quantitatively determine the intrinsically small MOKE [66] when combined with mathematical models. Note that the working principles behind the design described in Chapter 5 and the current device are the same. The latter design is experienced to be more robust against

external influence such as local temperature gradients causing refractive index changes. The advantage of the latter is suspected to be due to the small distance (hundred(s) of nm) between the magnetic and polarization changing components. In such short distances, the external fluctuations cannot impact the phase of light.

This chapter is structured in the following way. In Section 6.2 the methodology is provided, describing the design, mathematical modelling, fabrication and optical characterization of the magneto-photonic devices. Next, in Section 6.3, the experimental evidence demonstrating the proof-of-principle for the magneto-optical memory reading is demonstrated and the on-chip MOKE amplitude is quantitatively determined. Additionally, the optical simulation results are presented and compared with the experimental evidence. In Section 6.4 the conclusions are drawn.

6.2   Methodology

6.2.1   Design and Modelling

A magnetic cladding placed on a waveguide gives rise to the MOKE that is observed as an intrinsically small mode conversion between the eigenmodes (TE and TM) of the waveguide. Depending on the magnetization direction of the cladding (up- or downwards magnetized), the mode conversion occurs with a phase difference of π albeit with the same amplitude. In other words, the phase of the emergent mode encodes the information regarding the magnetization direction of the cladding, thus its memory state. However, since the relative phase is difficult to extract directly, we aim at a design that yields two different transmitted light output intensities depending on the magnetization direction of its cladding.

We present the design in its two formats: a core-module and a stand-alone device. The former solely contains the memory component and a polarization rotator element. Thus, it can provide the magneto-optical memory reading functionality, only when implemented in an integrated photonic environment. The stand-alone device includes the core-module and mode-selective grating couplers to couple light in from an external light source, and couple it out to a detector. It is tailored for proof-of-principle measurements. Figure 6.1 (a) depicts the core-module, while (b) and (c) demonstrate its functioning principles using the Poincaré sphere representation. Depicted in (a) as the top-cladding, the information is stored in a multi-layered, ferromagnetic, thin-film memory material that has Co/Pt bilayers on a Ta seeding layer. The triangular waveguide section acts as a partial polarization
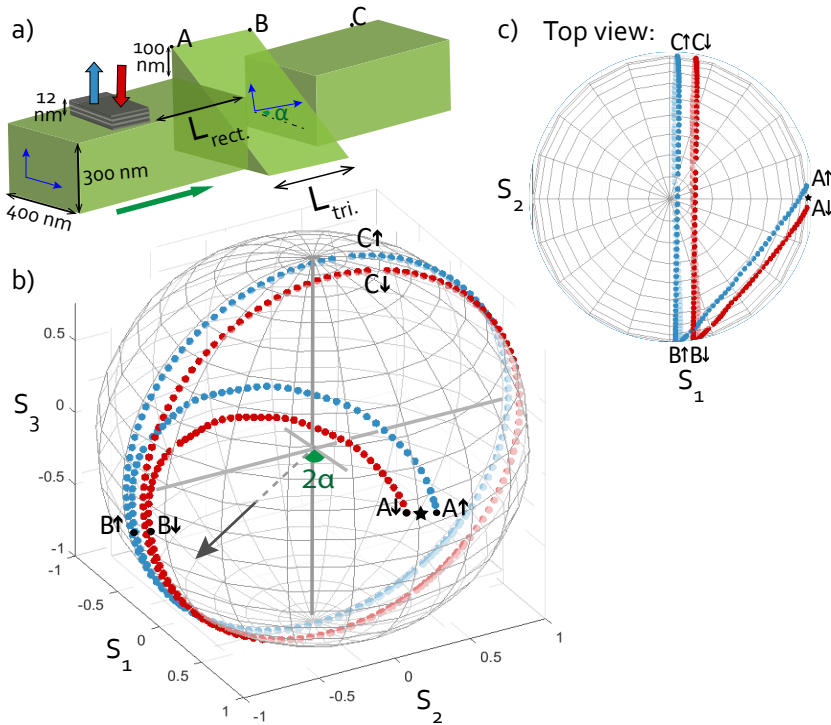
Figure 6.1: **(a)** The core-module of the magneto-photonic device, showing the magnetic memory component (multi-layered top-cladding) and the polarization rotator component (triangular waveguide). The two memory states (magnetization directions) are indicated with the red and blue arrows. The birefringence in the triangular section is indicated with the tilt of its eigenmodes axes by an angle α). **(b, c)** Poincaré sphere [267] representations showing the polarization state evolution throughout the device. Plots are color-coded (blue and red), indicating the magnetization direction of the cladding the light has interacted with (up and down, respectively.). Note that the chosen Kerr amplitude in the plots is for visualization purposes thus does not reflect the experimental results quantitatively.

converter [140], that is referred to in this work as a polarization rotator.

Let us describe the functioning principles of the core-module using the representations in Fig. 6.1 (b, c). Eigenmodes in different sections are referred to as the TE and TM modes of those sections. On the sphere, each point corresponds to a unique polarization state, indicated with the Cartesian co-ordinate system where S indicates the Stokes parameters [268]. The S_1-axis component relates to how much power is in the TE (S_1=1) or TM (S_1 =-1)
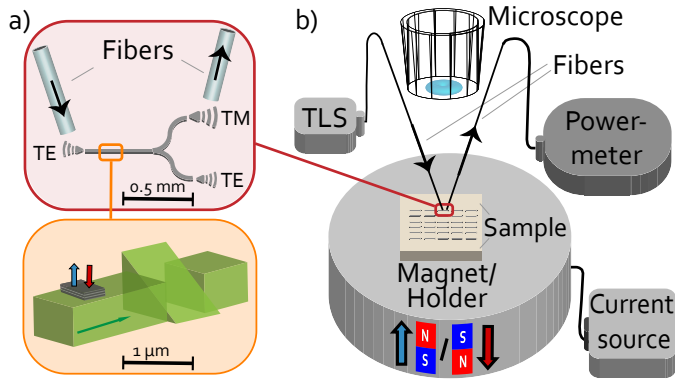
Figure 6.2: **(a)** A schematic of the proof-of-principle type, stand-alone magneto-photonic device. Top: Overall device with mode-selective (TE and TM) grating couplers, waveguides and splitters are shown. Bottom: A zoom-in view of the core-module, showing the memory component (top-cladding) and the polarization rotator (triangular waveguide). **(b)** The optical transmission measurement set-up. A Tunable Laser Source (TLS) sends the light (λ = 1550 nm) through the input fiber. After transmission through the device, the output fiber collects the light and directs it to the optical power meter. The sample holder is an electro-magnet that can apply up to ±300 mT perpendicular magnetic field, setting the magnetization direction of the memory component on-demand. The fibers are not polarization maintaining and are cleaved to enable an easier coupling.

mode. The S_2 and S_3-axes components describe the phase relation between the two modes. If the guided light is a mixture of the two modes, a mode beating occurs during propagation due to the difference of the effective refractive indices (or propagation constants) of the two modes. One period of beating length in a waveguide with cross-section cs is expressed as

$$L_{beat.,\text{cs}} = \frac{\lambda}{|\Delta n_{\text{eff.,cs}}|}, \tag{6.1}$$

where λ is the vacuum wavelength of the light and $\Delta n_{\text{eff.,cs}}$ is the difference in the effective refractive indices between the eigenmodes of that cross-section. As Figs. 6.1 (b, c) show, the TE-mode input (S_1=1, S_2=S_3=0), indicated with a star, propagates undisturbed (no mode-beating) until the region with the magnetic cladding is reached. Here, the MOKE takes place, yielding a small mode conversion described by the Kerr rotation (θ) and ellipticity (ε). Note that the attained complex MOKE signal (Φ) is slightly different for the TE and TM modes due to the difference in interaction between the cladding and the TE and

TM modes. The subscript TX indicates the mode is TE or TM.

$$\Phi_{\text{TX}} = m \left(\theta_{\text{TX}} + i \varepsilon_{\text{TX}} \right). \tag{6.2}$$

In our devices the TE mode is used as input. The up- and downward magnetized claddings are indicated with $m = \pm 1$. The equation reflects the statement that the mode conversion is equal in amplitude but with a phase difference of π for the two memory states. Upon attaining a mixed-mode state due to MOKE, a mode-beating occurs while propagating in the rectangular waveguide section through the length $L_{rect.}$. The beating is omitted in the figure for clarity. The triangular waveguide section has its unique eigenmodes that are tilted by an angle α with respect to the ones in the rectangular section. When the guided light enters the triangular waveguide section at point A (see Figs. 6.1 (b, c)), the modes get projected onto the tilted eigenmodes of this section. The projected states are marked by the points A↑ and A↓. The arrows indicate the magnetization orientation of the cladding thus the memory state and is represented by m=±1 elsewhere. As the mixed-mode travels in this section, the mode beating is observed as circling around the axis which makes an angle of 2α with respect to the S_1-axis (see arch $\overset{\frown}{AB}$). After propagating over a distance $L_{tri.}$, which is chosen to be equal to the half beat length of the triangular section, the states B↑ and B↓ are obtained. Coupling back to the rectangular waveguide, the phase evolution continues as shown by the arch $\overset{\frown}{BC}$. Comparing the initial polarization state (⋆) with the final states (C↑ and C↓) -in terms of TE and TM mode contributions- highlights the working principle of the presented design. Figure 6.1 (b, c) geometrically illustrate that, prior to propagation in the triangular section, the states that correspond to the magneto-optic interaction with the up- and down-magnetized claddings have the same relative power in the TE and TM-modes of the rectangular section (equal S_1 components of A↑ and A↓). After the triangular section, a difference in the relative mode-power is created, i.e. the S_1 components are different for C↑ and C↓. This difference provides the magneto-optical memory reading functionality. The figure provides an intuitive picture that by engineering the rectangular and the triangular section lengths, the mode intensity contrast can be maximized.

The second format of the design, the stand-alone device form, is designed for the proof-of-principle measurements. A mathematical model based on the Jones formalism [176] assisted with the design and the analysis of the experimental observations. Depicted in Fig. 6.2 (a), the device has a TE mode-selective in-coupler and TE and TM mode-selective out-couplers. As seen in Fig. 6.2 (b), the optical fibers connect the couplers to an external

laser and an optical power meter. In the mathematical model that describes this device, the MOKE matrix **M** is defined as

$$\mathbf{M} = \begin{pmatrix} 1 & -\Phi_{\mathrm{TE}} \\ \Phi_{\mathrm{TM}} & 1 \end{pmatrix},$$ (6.3)

where Φ_{TX} is the complex Kerr signal (see Eqn. 6.2) experienced by the TE or TM-mode inputs. We note that the defined MOKE matrix is an over-simplification, only valid when the input is a pure mode and the Kerr signal is small in amplitude (which is always the case). The phase evolution of the light due to propagation in a waveguide with a certain cross-section is indicated with the matrix $\mathbf{P}_{\mathrm{cs}}$.

$$\mathbf{P}_{\mathrm{cs}} = \begin{pmatrix} e^{i\frac{2\pi}{\lambda}n_{\mathrm{a,cs}}L_{\mathrm{cs}}} & 0 \\ 0 & e^{i\frac{2\pi}{\lambda}n_{\mathrm{b,cs}}L_{\mathrm{cs}}} \end{pmatrix},$$ (6.4)

where $n_{\mathrm{a,cs}}$ and $n_{\mathrm{b,cs}}$ are the effective refractive indices of the modes that are defined as the horizontally (in-plane) oriented electric and magnetic fields in that particular cross-section. The waveguide length with the corresponding cross-section is indicated with L_{cs}. To describe the propagation in the triangular section, the axis of interaction is tilted back and forth via the rotation matrix **R**. This tilt is required in order to align the eigenmodes of this section with the axis of interaction. It is formulated as

$$\mathbf{R} = \begin{pmatrix} \cos\alpha & \sin\alpha \\ -\sin\alpha & \cos\alpha \end{pmatrix},$$ (6.5)

where α is the tilt angle. Correspondingly, the resulting mode-specific output electric field $\mathrm{E}_{\mathrm{TX_o}}$ is formulated as

$$\begin{pmatrix} \mathrm{E}_{\mathrm{TE_o}} \\ \mathrm{E}_{\mathrm{TM_o}} \end{pmatrix} = \mathrm{R}(-\alpha) \cdot \mathrm{P}_{tri.} \cdot \mathrm{R}(\alpha) \cdot \mathrm{P}_{rect.} \cdot \mathrm{M} \cdot \begin{pmatrix} \mathrm{E}_{\mathrm{TE_i}} \\ \mathrm{E}_{\mathrm{TM_i}} \end{pmatrix},$$ (6.6)

where $\mathrm{E}_{\mathrm{TX_i}}$ is the input E-field. For the sake of simplicity, in all matrices the optical losses are neglected, but including them would not change the general principle. Since the mode-specific light intensity I_{TX} is proportional to the output light's field amplitude square $|\mathrm{E}_{\mathrm{TX_o}}|^2$,

we calculate the mode-specific intensity contrast (ΔI_{TX}) in units of dB as

$$\Delta I_{TX} = 10 \log_{10} \left(\frac{|E_{TX_o, m=1}|^2}{|E_{TX_o, m=-1}|^2} \right).$$

(6.7)

Equation 6.7 accounts for the difference in transmission when the memory state of the device is changed. Despite the fact that the optical losses are ignored, a quantitative analysis using Eqn. 6.7 is possible since it is in the ratio form.
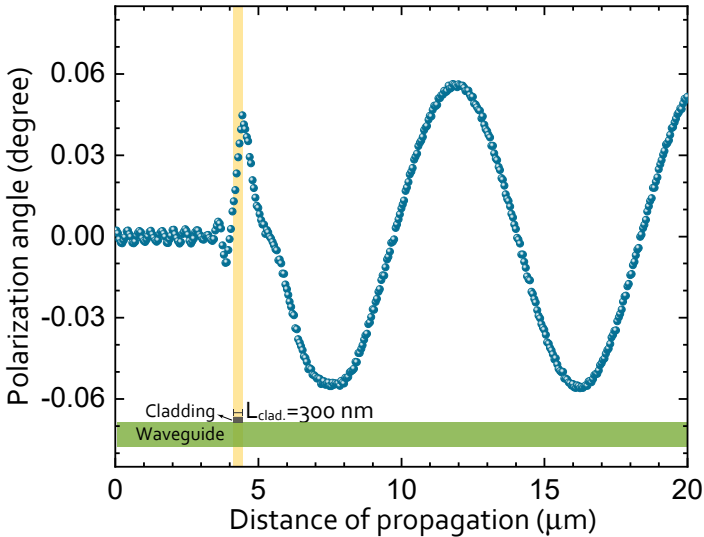
Figure 6.3: Optical simulation (FDTD), showing the polarization evolution of the initially purely TE-polarized input light, as it propagates in the rectangular waveguide section cladded with the memory material. The polarization angle refers to the rotation caused by the MOKE. The region with the magnetic cladding (memory) is shown with the vertical highlighted region. The stack order and the length of the cladding are Ta4/Pt2/Co1/Pt2/Co1/Pt2 (numbers in nm) and 300 nm, respectively. A conformal meshing of 2 nm is used.

Lastly, we present an optical simulation based on the Finite Difference Time Domain (FDTD) method [183, 187, 269] that demonstrates the polarization angle evolution as a function of the propagation distance. The simulation uses material properties, i.e. the refractive indices and the magneto-optical constants that were previously obtained experimentally for this specific material set (see Chapter 4) [195]. Figure 6.3 shows an initially fully TE-polarized input mode that interacts with a 300 nm-long magnetized top-cladding. Ac-

cording to the simulations, the amplitude of the complex MOKE ($|\Phi_{\mathrm{TE}}|$) is $0.06^{\circ} \pm 0.02^{\circ}$. As will be discussed in Sect. 6.3, this is in good agreement with the experimental findings. In Fig. 6.3, the highlighted region indicates the length covered by the cladding. In this region, the Kerr rotation increases cumulatively. The simulation accounts for both forward and backward propagating waves. The Kerr rotation observed within the first μm of propagation after the cladding suggests that there are non-confined (higher order) modes, possibly excited by the cladding, which also show a finite MOKE. Higher order modes reflected (backwards propagating) from the cladding show the same behavior. After these higher-order modes decay, a purely oscillatory polarization (due to MOKE on the primary mode) state is captured by the simulation. The beating periodicity of 8.1 μm indicates an effective index difference ($|\Delta n_{\mathrm{eff.TE}} - \Delta n_{\mathrm{eff.TM}}|$) of 0.19 (see Eqn. 6.1). This value is close to what can be calculated for the specific rectangular InP waveguide of choice, using literature values for the refractive index. In the region prior to the cladding, oscillations in Kerr rotation with higher frequency and lower amplitude are observed. They are attributed to an interference including the reflections from the cladding, which also experience a MOKE.

6.2.2   Fabrication

The magneto-photonic devices are based on the IMOS platform [32]. The devices have varying lengths of rectangular and triangular waveguide sections ($L_{rect.}$ and $L_{tri.}$, respectively), and two magnetic cladding lengths of 300 nm and 600 nm are used (albeit with an equal width of 400 nm, which is the same as the waveguide width).

Briefly describing the fabrication process, the photonic structures are defined with multiple e-beam lithography (EBL) steps, followed by wet- and dry-etching steps of the InP membrane. The etching steps are based on acid solution etching and reactive ion etching via an inductively coupled plasma, respectively. The sloped side-walls of the triangular waveguides are obtained with wet-etching, where the $\overline{11}2$ crystalline planes naturally terminate the etch [270]. The vertical side-walls are realized with dry-etching. The thickness of the triangular and rectangular sections are 460 nm and 300 nm, respectively. For details on the fabrication process, we refer the reader to a previous work [193]. The memory components are applied on top of the waveguides as claddings. To define the area of the memory bit, an additional overlay exposure EBL step is used. After ensuring a clean opening on the InP membrane, the multi-layers are deposited using magnetron sputtering, further explained in [195]. The stack order of the multi-layer is Ta4/Pt2/Co1/Pt2/Co1/Pt2, numbers

indicating the layer thickness in nm. After the metal deposition, a lift-off step is performed to remove the excess metal film from the devices.

Characterization of the photonic components, as described in Appendix A.3, revealed that the effective refractive index differences in rectangular ($\Delta n_{\text{eff.,rect.}}$) and triangular waveguide sections ($\Delta n_{\text{eff.,tri.}}$) are 0.25 and 0.34, respectively; while the angular tilt of the eigenmodes in the triangular section (see α in Fig. 6.1 (a)) is $21°$.

6.2.3   Measurement set-up

Optical transmissions from the stand-alone devices are measured in the set-up depicted in Figure 6.2 (b). Since the magneto-photonic devices are designed to yield different mode-specific outputs for opposing memory states, the set-up is designed to probe the optical transmission while switching the magnetization direction of the memory component. Therefore, the set-up included a fiber coupled laser source ($\lambda = 1550$ nm), an optical power meter and an electromagnet sample holder connected to a current source allowing to apply perpendicular magnetic fields up to 300 mT in up- and downward directions. The applied field is used to set the magnetization direction of the cladding, thus its memory state.

Two different measurement procedures are followed. The first one is aimed at hysteresis measurements, where a strong field is applied in a certain direction at the beginning to set the magnetization direction of the cladding. Then, the magnetic field is incrementally swept towards both directions, and the optical transmission is probed. The second method, the contrast measurement, is focused on probing the difference in the light transmission between the remanent up- and down- states. In this method, the magnetization direction of the cladding (the memory bit) is periodically switched between the up- and downwards magnetized states by applying fields with equal amplitude but opposite sign. The transmitted light intensity is recorded after setting of the magnetization direction. Note that in both procedures, the transmission is measured after removing the externally applied magnetic field. Despite this, the magnetization of the thin-film is preserved due to its non-volatility.

6.3   Results and Discussions

As described earlier, the magneto-optical memory reading functionality is achieved by designing devices that yield different mode-specific transmissions depending on their cladding's memory state. In this section, we present the measurements obtained from

such devices. The model (presented in Sect. 6.2.1) predicted the dependence of the mode-specific transmission contrast on certain device parameters. We provide evidence that this is indeed the case and the MOKE for light confined in waveguides can be quantitatively determined using this model. Lastly, we compare the reported experimental findings with the previously presented optical simulation results (Sect. 6.2.1).
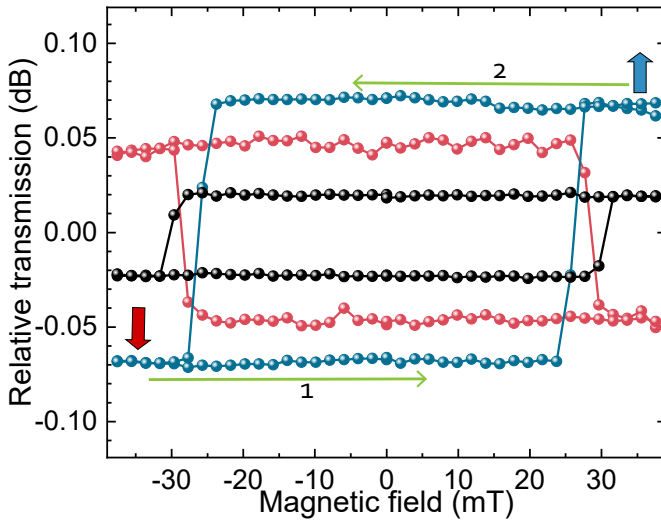
Figure 6.4: Hysteresis behavior observed in the mode-specific transmission as a function of the applied magnetic field when fully TE-mode input light is used. Plots show different magneto-photonic devices (with varying lengths of $L_{rect.}$ and $L_{tri.}$), albeit with the same magnetic cladding length of 600 nm. Prior to the measurements, the memory state of the cladding is set by applying -40 mT field. Then, the magnetic field is swept in the direction and order indicated with the horizontal arrows. The jumps in the relative transmissions (at approximately $\pm$ 30 mT), correspond to the switching of the magnetization direction of the claddings, thus changing of the memory states. The combinations of ($L_{rect.}$, $L_{tri.}$) length parameters in μm are (7.77, 4.3), (7.77, 1.0) and (5.07, 2.2); for blue, red and black data-sets, respectively.

Figure 6.4 shows the relative TE-mode transmission (in units of dB) from three different devices as a function of the applied magnetic field. The signal is normalized with respect to the transmission of the TE-mode when the cladding is not magnetized. The figure shows a clear hysteresis behavior. As mentioned in Sect. 6.2.3, the built-in memory components

(top cladding) of the devices are set to downward magnetized states by applying a magnetic field of -40 mT prior to the measurements. As indicated with horizontal arrows in the figure, the applied field is swept in both directions, creating the depicted loops. The changes in the mode-specific transmission at the coercive fields of approximately ± 30 mT, indicate that the magnetization direction of the built-in memory element is changed. The abruptness of the changes indicates that the claddings have PMA, thus the preferred magnetization orientation lays out-of-plane. This was confirmed using polar MOKE measurements ex-situ, in a free space optics set-up, i.e. with light incident from above. To our knowledge, this is the first time hysteresis behavior is observed on-chip for such a sub-micron magnetic memory element. These experimental findings prove that the magneto-optical memory reading in integrated photonic circuits is possible by using such designs with a reasonable signal-to-noise ratio (SNR). Additionally, Fig. 6.4 demonstrates that the amplitude and the sign of the obtained contrast depend on the length parameters ($L_{rect.}$ and $L_{tri.}$) of the device. This observation is in accordance with the predictions of the model (as can be derived from Eqn. 6.6).

Further evidence to the dependence of the mode-specific contrast on certain device parameters is provided by Figs. 6.5 and 6.6. Here the contrast refers to the difference in the mode-specific transmission (ΔI_{TX}) in units of dB. More specifically, it refers to the difference (between the up- and downwards magnetized cladding) in the output intensity for the same mode (TE or TM). In the figures, the mode-specific contrasts (Eqn. 6.7) are plotted as a function of the rectangular and triangular waveguide section lengths ($L_{rect.}$ and $L_{tri.}$), respectively. The figures depict the experimentally obtained values and the fits to the model predictions with the separate data-points and the dashed/continuous lines, respectively. Figure 6.6 shows an asymptotic behavior for the TM-specific mode contrast as the $L_{tri.}$ approaches to 0 and 4.5 μm. This is a result of the diminishing overall TM-mode transmission from the devices. When the length of the triangular waveguide (polarization rotator) is $L_{tri.}$ = 0 μm or $L_{tri.}$ = $L_{beat.}$, the TM-mode transmission from the devices almost vanishes and thus the relative contrast diverges.

Using the experimental evidence of mode contrasts from devices with varying length parameters, we quantitatively determined the magneto-optical activity in terms of the MOKE amplitude, as it is often the reported figure-of-merit [271]. The amplitude of the complex value is calculated as $\sqrt{\theta_{TX}^2 + \varepsilon_{TX}^2}$. The resulting amplitudes for a large number of devices with different parameters are summarized in Fig. 6.7. The standard deviation amongst the obtained values is indicated with the width of the highlighted region. Results show that

Figure 6.5: Mode-specific transmission contrasts (ΔI_{TX}) obtained from devices with different rectangular waveguide section lengths $L_{rect.}$. The mode contrast (Eqn. 6.7) refers to the difference in dB transmission when the memory state is changed (when the magnetization direction of the cladding is switched). Devices with the magnetic cladding lengths of 300 nm (half-filled points) and 600 nm (filled points) are reported. All devices have a triangular section length $L_{tri.}$ of 1.8 μm. While the data-points are the experimentally obtained values, the lines (dashed or solid) indicate the predictions for a certain MOKE signal (Eqn. 6.7). $L_{rect.}$ refers to the distance between the magnetic cladding and the triangular section (see Fig. 6.1 (a)).

the Kerr amplitude $|\Phi_{\mathrm{TX}}|$ doubles (within the error margin) upon doubling of the cladding length $L_{clad.}$ (300 to 600 nm). The linear dependence of the mode contrast ΔI_{TX} on $L_{clad.}$ is in accordance with the predictions by FDTD simulations (not shown here). The simulations predict that the linear relation holds for $L_{clad.}$ up to the half a beat length in the rectangular waveguide section $L_{beat.,rect.}$. The experimentally obtained MOKE amplitude $|\Phi_{\mathrm{TE}}|$ of $0.09° \pm 0.02°$ for $L_{clad.}=$ 300 nm closely matches with the simulated value of $0.08° \pm 0.02°$ based on previously reported [195] values of (magneto-) optical parameters (see Fig. 6.3). The optical loss was found to scale linearly as well with $L_{clad.}$. In the current configuration, the experimentally obtained loss per 100 nm cladding length is 0.55 dB for the TE mode. This finding is comparable to the simulation results of a different waveguide geometry [41].
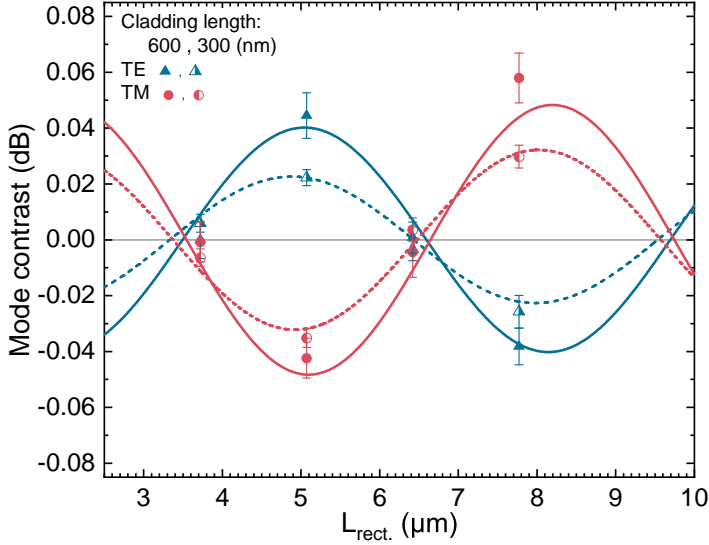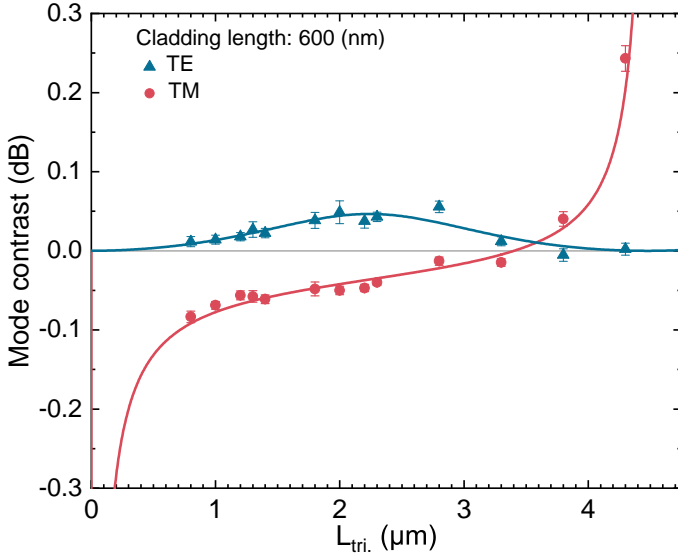
Figure 6.6: Mode-specific transmission contrasts (ΔI_{TX}) obtained from devices with different triangular waveguide section lengths ($L_{tri.}$). The mode contrast refers to the difference in transmission when the memory state is changed (when the magnetization direction of the cladding is switched). All devices have a rectangular waveguide section length $L_{rect.}$ of 5.07 μm, and a cladding length $L_{clad.}$ of 600 nm. The data-points indicate the experimentally obtained values while the solid lines are the predictions for the fitted MOKE signal (Eqn. 6.7).

The same work [41] also discusses the trade-off between loss and signal contrast as a function of the cladding length.

Regarding the noise in the experimental results, the major source of instability is found to be the stochastic movement of the optical fibers over the grating couplers (see Fig. 6.2 (a)). In a future application where the core-module is combined with a built-in laser and detector, the noise from the moving parts would be eliminated, allowing the SNR to improve many orders of magnitude. In order to place such a prospect device on the map with respect to the current technologies, and demonstrate its promises in terms of bandwidth of data read-out, we assumed an ideally stable configuration and perfect (opto-)electronical components, where the device is limited by shot noise. Accordingly, to resolve the 1% contrast that the current device delivers, we calculated the theoretical limit of the maximum data rate to be better than 50 Gbits/s (see Appendix A.4). Assuming that the memory is

implemented in the form of a racetrack memory [199, 272], for which rapidly increasing domain wall velocities have been reported [248, 273], the prospect device competes well with the optical [274] and electrical [275] counterparts that currently offer tens of Gbits/s and few Gbits/s [258], respectively.
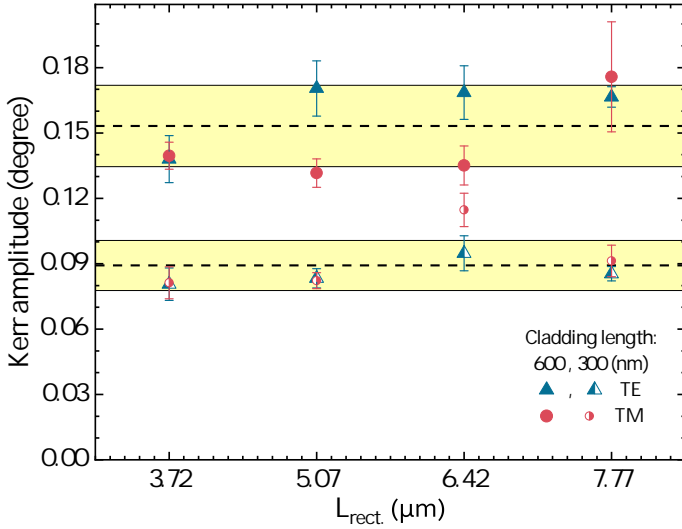
Figure 6.7: Kerr amplitudes (Φ_{TX}) determined from devices with varying propagation lengths in the rectangular waveguide section ($L_{rect.}$). The results from devices with two different cladding lengths ($L_{clad.}$ = 300 nm and 600 nm) are shown. Each data-point is the result of a fitting procedure where 4 devices with varying $L_{tri.}$ are used. The error bars indicate the accuracy of the fits. The dashed horizontal lines show the average Kerr amplitude, while the widths of the highlighted regions indicate the standard deviation of the reported data-points.

6.4   Conclusions

For the first time, we demonstrate magneto-optical reading of a non-volatile magnetic memory in an integrated photonic device setting. This was achieved via the designed hybrid magneto-photonic devices implemented in IMOS. Devices are engineered such that the guided light yields a difference in the mode-specific optical transmission upon changing of the memory state up to 1%. With this, the typical hysteresis behavior observed in

magnetic materials is demonstrated in an on-chip setting. It is highlighted that our photonic memory material of choice having out-of-plane magnetic orientation offers the advantages of enhanced MOKE in this polar configuration and higher memory storage densities. Additionally, the multi-layered ferromagnetic thin-films are well-established for spintronic memory applications and compatible with the PIC-technology.

We developed a mathematical model that describes the transmitted mode intensity in terms of device parameters, and which assisted the design process and helped to interpret the experimental observations. Thanks to the model, the quantitative determination of the MOKE in integrated photonic devices is possible, which enables a quantitative comparison with the optical simulations. The simulations that utilize the magneto-optical constants we previously determined [195], successfully reproduce the experimental observations and provide insights into the MOKE for light confined in waveguides. This is significant, since it validates the determined magneto-optic activity in ultra thin-films and builds confidence on the results from simulations.

As a technological outlook, a theoretical limit of memory read-out bandwidth of tens of Gbits/s is predicted, based on the current device designs. We discussed that establishing a photonic memory that can compete with the electronic counterparts has the potential of drastically improving the data-com and tele-com operations, cutting down on the requirements of back-and-forth electronic to optical signal conversions. Such a device is envisioned to directly generate amplitude modulated photonic bit patterns out of the magnetic memory, avoiding any energy and time consuming high-frequency electronic operations.

Chapter 7

Outlook

We have shown that it is possible to detect the magnetization direction of the magnetic cladding, using dedicated integrated photonic devices. Proof-of-principle experiments show that the built-in magnetic claddings can be utilized as a non-volatile photonic memory. This section is intended to provide the reader with an outlook, including possible improvements and areas of applications.

Whatever application one has in mind, increasing the signal-to-noise ratio of devices is a must. One of the lessons from experimental efforts is that implementation of a built-in laser and on-chip detectors in photonic devices can greatly help reducing the noise that stems from external vibrations. Fortunately, the implementation of built-in lasers and detectors is within the competence of the IMOS platform, and therefore can be implemented in the future. Additionally, increasing the signal contrast and the magneto-optic activity in devices is of great importance. Two routes can be taken for such improvements. The first is for yielding a better contrast when the memory state is switched. To achieve this, the multi-layered stacks in claddings can be engineered. As concluded in Chapter 4, the Co/Pt interface contributes greatly to the overall magneto-optic activity. Properties such as interface roughness and orientation of the crystalline planes at the interface contribute to the resulting signal contrast. The second route for improvement focuses on enhancing the magneto-optic signal. This could be achieved by exploring novel ways such as the use of plasmonics. Simply put, increasing the mode overlap with the magnetic element, i.e., increase the EM field strength inside the magnetic thin film would enhance the resulting magneto-optic signal. Currently, there are ongoing efforts within the research group using

plasmonic effects to enhance the polar MOKE [276].

Drawing an outlook for the potential application areas, let us first focus on the optical memories. Currently, optical memory alternatives are sought after to be used in circuits for photonic computation, more specifically neuromorphic computing [277]. A great potential is anticipated for non-volatile, energy efficient optical memory alternatives. Therefore, the on-chip magneto-optical memory presented in this thesis holds a potential to be used in such photonic computation hardware. Operations required for a neuromorphic computation in photonic circuits can be simplified as realizing a series of matrix multiplications [278], which can be done using interferometers [279]. In such circuitry, we conjecture that the 'weight constants' [277] could be defined by the magneto-optic memory elements, applied directly on the interferometer structures. Apart from the optical memory applications, the on-chip magneto-optic activity detection presented in this Thesis can be used for sensing applications. When combined with the Faraday effect, a magnetic field sensor can be obtained that allows for optical readout, suitable for photonic integration. Furthermore, since the magneto-optic activity in multi-layered thin films is affected by the changes in material properties at the nanoscale [195], a dedicated sensor can be designed for probing depth-sensitive material degradation processes. As this can be done in real-time, sensory data can be used to shed light to unknown degradation mechanisms. Recalling that plasmonics can be used to enhance the magneto-optic interaction at desired 'hot-spots', this can be of help when probing certain desired areas, e.g. to conduct depth sensitive measurements.

Appendices

Appendix A

Appendices

A.1 Mathematical model for MOKE in multilayered thin-films

For the light's propagation within a layer, a medium propagation matrix (D) is defined. For the interface between the two layers, a medium boundary matrix (A), which embeds the boundary conditions, is formed. Via the Jones matrix formalism [176] the multi-layered stack is described in terms of matrix multiplications of the medium propagation and the medium boundaries.

A simple 2-media system where A_1 and A_2 are the boundary matrices of medium 1 and 2 is shown in Equations A.1 and A.2. The terms r_{ss} and r_{pp} are the reflectivity coefficients of s and p-polarized light while t_{ss} and t_{pp} are the transmissivity correspondents. The terms r_{sp} and r_{ps} represent the reflectivity coefficients of the s-polarized light that was initially p-polarized and vice versa.

For s-polarized light:

$$A_1 \cdot \begin{pmatrix} 1 \\ 0 \\ r_{ss} \\ r_{ps} \end{pmatrix} = A_2 \cdot \begin{pmatrix} t_{ss} \\ t_{ps} \\ 0 \\ 0 \end{pmatrix}, \tag{A.1}$$

and for p-polarized light:

$$A_1 \cdot \begin{pmatrix} 0 \\ 1 \\ r_{sp} \\ r_{pp} \end{pmatrix} = A_2 \cdot \begin{pmatrix} t_{sp} \\ t_{pp} \\ 0 \\ 0 \end{pmatrix}. \tag{A.2}$$

A 3-media system is shown in Equations A.3 and A.4 where A_1, A_2 and A_3 are the medium boundary matrices of the corresponding media and $\overline{D}$ is the medium propagation matrix at medium 2.

For s-polarized light:

$$A_1 \cdot \begin{pmatrix} 1 \\ 0 \\ r_{ss} \\ r_{ps} \end{pmatrix} = A_2 \cdot \overline{D} \cdot A_2^{-1} \cdot A_3 \cdot \begin{pmatrix} t_{ss} \\ t_{ps} \\ 0 \\ 0 \end{pmatrix}, \tag{A.3}$$

and for p-polarized light:

$$A_1 \cdot \begin{pmatrix} 0 \\ 1 \\ r_{sp} \\ r_{pp} \end{pmatrix} = A_2 \cdot \overline{D} \cdot A_2^{-1} \cdot A_3 \cdot \begin{pmatrix} t_{sp} \\ t_{pp} \\ 0 \\ 0 \end{pmatrix}. \tag{A.4}$$

Note that the boundary and the propagation matrices (A and $\overline{D}$) are presented in closed-forms since the detailed matrix forms do not convey insightful information. For detail we refer the reader to this work [182].

As indicated earlier, while the multi-layered system is still in the thin-film limit of:

$$\frac{2\pi}{\lambda} \sum d_m \mid N_m \mid \ll 1,$$

the relations are linear in thickness d which leads to the additivity law of Kerr effect. This feature enables the addition of multiple layers, either magnetic or non-magnetic, by replacing the terms $A_2 \cdot \overline{D} \cdot A_2^{-1}$ with $\prod_2^m A_m \cdot \overline{D}_m \cdot A_m^{-1}$.

Collecting reflection coefficients of r_{ss}, r_{pp}, r_{sp} and r_{ps} in one matrix is possible through the following algebraic steps. Collect the terms of propagation and the reflection matrices

in Equations A.3 and A.4, and assign the result to a multiplication matrix to M as:

$$A_1^{-1}.A_2.\overline{D}.A_2^{-1}.A_3 = M.$$

Then, the Equations A.3 and A.4 become:

$$\begin{pmatrix} 0 \\ 1 \\ r_{sp} \\ r_{pp} \end{pmatrix} = M. \begin{pmatrix} t_{sp} \\ t_{pp} \\ 0 \\ 0 \end{pmatrix}, \qquad \begin{pmatrix} 1 \\ 0 \\ r_{ss} \\ r_{ps} \end{pmatrix} = M. \begin{pmatrix} t_{ss} \\ t_{ps} \\ 0 \\ 0 \end{pmatrix}.$$

In this case M is an 8x8 matrix that can be split into 4 block matrices of 2x2 for compactness. The block matrices are named as G, I, H and J are presented in the following form:

$$M = \begin{pmatrix} G & H \\ I & J \end{pmatrix}.$$

Since the s- and p- polarized light are indistinguishable at perpendicular incidence, MOKE is both defined by $\frac{r_{sp}}{r_{pp}}$ and $\frac{r_{ps}}{r_{ss}}$. Therefore, we are interested in the 2x2 matrix section whose components are these reflectivity coefficients. This is achieved by the following matrix operation.

$$\begin{pmatrix} r_{ss} & r_{sp} \\ r_{ps} & r_{pp} \end{pmatrix} = IG^{-1}. \tag{A.5}$$

A.2   An effective permittivity tensor definition for multi-layered magnetic materials

Optical simulations require significantly higher computational power when simulating the MOKE. This load increases further when a finer mesh is required to resolve the thin-film (12 nm) magnetized cladding. We decreased the computational load in optical simulations by re-defining a magnetic cladding volume that is larger than the original, albeit with adjusted material properties that corresponds to reality (within a confidence interval).
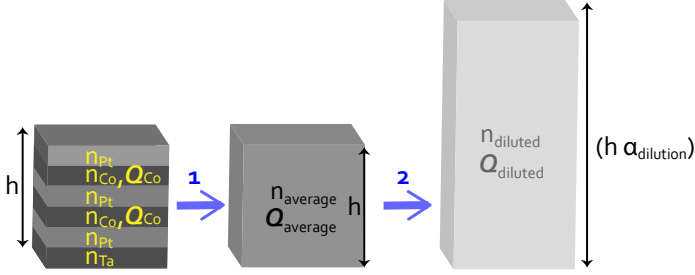
Figure A.1: Re-defining the multi-layered magnetic cladding (memory material) for saving computational power during optical simulations. The thickness is increased by a factor of $\alpha_{dilution}$ while the length and width are kept the same. Material properties of refractive indices (n) and magneto-optic Voigt constants (Q) are re-defined for the new volume, to effectively yield the same macroscopic results.

As shown by the left-most image in Fig. A.1, the multi-layered thin-film cladding is used with a stack order of Ta4/Pt2/Co1/Pt2/Co1/Pt2 (numbers in nm) in this work. We re-defined the material properties of the refractive index and the magneto-optic Voigt constant (Q) such that it will account for an effective layer as shown in the middle part of Fig. A.1. Let us describe the processes that are numbered as '1' and '2' by the arrows in Fig. A.1. In the arrow number 1, we calculated an average refractive index ($n_{average}$) and an average magneto-optic constant ($Q_{average}$) that accounts for the whole volume of the cladding. These are weighted averages of the contributing layers as indicated with the multiplication by the thickness (t_x).

$$n_{average} = \sqrt{\frac{(n_{Pt}^2 - 1)t_{Pt} + (n_{Co}^2 - 1)t_{Co} + (n_{Ta}^2 - 1)t_{Ta}}{t_{total}} + 1} \ . \tag{A.6}$$

The average magneto-optic constant is calculated by assuming the total volume is magnetic. The solution is found by using mathematical model of the MOKE in multi-layers described in Sect. 3.2.1. In the second step of arrow number 2 in Fig. A.1), we increased the volume of the cladding and the determined material properties of the new volume. We name this procedure dilution since the material properties are averaged-out by the surrounding lower refractive index medium. The dilution factor $\alpha_{dilution}$ is defined as

$$\alpha_{dilution} = t_{new\,volume} / t_{old\,volume} \ , \tag{A.7}$$

Then, the diluted refractive index and magneto-optic constant are calculated as

$$n_{diluted} = \sqrt{\frac{n_{average}^2 - 1}{\alpha_{dilution}} + 1} \; , Q_{diluted} = \frac{\frac{Q_{average}}{\alpha_{dilution}} n_{average}}{n_{diluted}^2} \; .$$ (A.8)

In order to depict to what extend the diluted medium approximation corresponds to the original behavior, we utilized an analytical model. Fig. A.2 demonstrates the confidence interval of the mentioned dilution method. For a dilution factor of 2, the vertical axis shows the expected Kerr rotation while the horizontal axis shows the thickness of the modelled film with respect to the wavelength of the probing light (λ). As used in this work, a total film thickness of 12 nm and probing light wavelength of 1550 nm corresponds to the vertical dashed line at Film thickness / λ of $\approx$ 0.008. The model predicts that when the original volume of the magnetic cladding is increased and the refractive index and the magneto-optic constant are 'diluted', a 10 % larger Kerr rotation is estimated. Despite the inexact results the dilution would yield, we concluded that this is a negligible difference considering the benefit of shorter and less power-consuming simulations. Dilution factors of 2 to 4 are utilized.
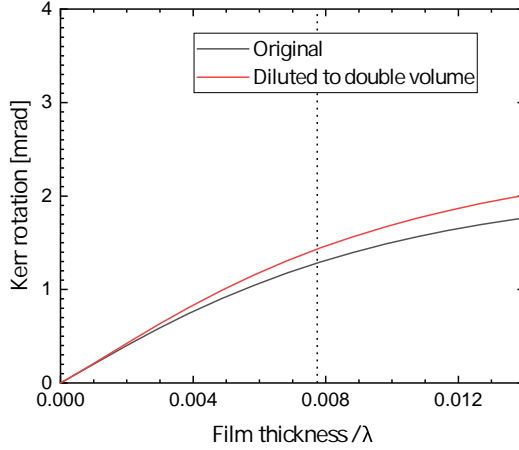
Figure A.2: The schematic shows the modelled behavior of the resulting Kerr rotation for single incidence onto the magnetic cladding surface. An original cladding thickness of 12 nm is used which corresponds to 24 nm thick film when diluted to double its volume. Horizontal axis shows a range of values for Film thickness / λ. For the claddings and the wavelength of light utilized in this work, this corresponds to the vertical dashed line of $\approx$ 0.008.

A.3 Appendix: Characterization of the photonic components

Characterization of the light transmission of the photonic devices has been performed during the fabrication process, more specifically after the fabrication of the photonic structure and before the placement of the magnetic claddings.

The mathematical model predicts that the triangular waveguide section provides a partial mode conversion where the electric fields of TE or TM modes are expressed as

$$\begin{pmatrix} E_{TE_o} \\ E_{TM_o} \end{pmatrix} = R(-\alpha) \cdot P_{tri.} \cdot R(\alpha) \cdot \begin{pmatrix} E_{TE_i} \\ E_{TM_i} \end{pmatrix}. \tag{A.9}$$

The mode intensities are

$$|E_{TM_o}|^2 = \sin(2\alpha)^2 \sin\left(\frac{\pi}{\lambda} \Delta n_{tri.} L_{tri.}\right)^2,$$
$$|E_{TE_o}|^2 = 1 - |E_{TM_o}|^2, \tag{A.10}$$
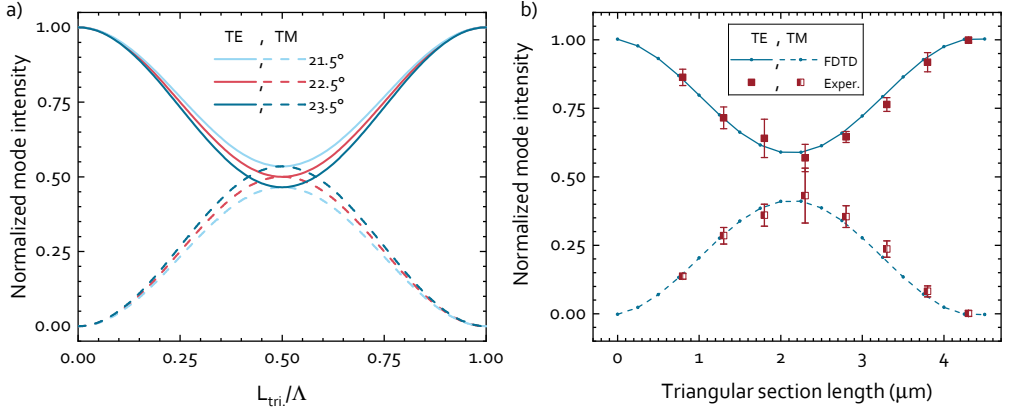
Figure A.3: **(a)** Modelled mode conversion as a function of triangular cross-section waveguide length showing the case for different values of α. Note that the beating length $L_{beat \cdot cs}$ is indicated by Λ. **(b)** FDTD simulation and experimental evidence showing mode conversion as a function of triangular cross-sectioned waveguide length. Error bars are defined by measuring 3 sets of identical devices. Both graphs assume TE mode input.

where $\Delta n_{tri.}$ is the difference between the TE and TM modes effective refractive indices. The mode-specific normalized light intensities from these devices without the magnetic claddings are shown in Figs. A.3 (a) and (b). Fig. A.3 (a) depicts the mathematical model predictions while (b) shows the experimental evidence combined with the FDTD simulations. By using Eqn. A.10 to interpret the data in Fig. A.3 (b), we found $\Delta n_{tri.} = 0.34$ and $\alpha = 21.02°$. Note that the experimental observation of the mode beating behavior in the rectangular section is used for the determination of $\Delta n_{rect.} = 0.25$, which is slightly different than the (FDTD) simulated value (0.19). This is expected to be due to the side-wall roughness that is ignored during the simulations.

A.4 Appendix: Theoretical bandwidth limit of the memory read-out

For a magneto-photonic device using the design presented in this work as a core-module, we calculated the theoretical memory reading bandwidth. We assumed that the device is limited by the shot-noise to calculate the theoretical SNR. Note that shot-noise scenario assumes that there is no loss, meaning all the input power is received back as signal. Using

such an estimation we determined if the proposed memory read-out device is competitive with alternative optical and electrical memory devices. The experimentally obtained Kerr rotation θ_{TX} and phase $\varepsilon_{\mathrm{TX}}$ when $L_{clad.}$ = 600 nm, we calculated the E-field amplitudes at the output of the device. The SNR in this case is given by

$$\mathrm{SNR} = \sqrt{\frac{P_{in}t}{E_{ph}} \frac{\Delta T_{\mathrm{TX_0}}}{T_{average_{\mathrm{TX_0}}}}}, \qquad (A.11)$$

where P_{in} is the input power, E_{ph} is the photon energy at a wavelength of 1550 nm and t is the duration in which the laser is on. Assuming an SNR of 6 would suffice to resolve the signal from the noise; a laser input power of 5 mW revealed the duration t that is required for the measurement to succeed. This time restriction indicates a read-out speed of about 60 Gbits/s. We emphasize that this value is based on our present experimental results and assumes the loss is zero. Further efforts to increase the MO contrast by optimizing the magnetic cladding composition and possible improvements in the photonic design can yield higher theoretical speeds. Such engineering is expected to further boost the MO contrast and, consequently, the theoretically achievable data rates.

Bibliography

[1] Robert R Schaller. Moore's law: past, present and future. *IEEE spectrum*, 34(6):52–59, 1997.

[2] Michael G Raymer. *The silicon web: physics for the Internet age*. CRC Press, 2009.

[3] Fred J Pollack. New microarchitecture challenges in the coming generations of cmos process technologies (keynote address). In *Proceedings of the 32nd annual ACM/IEEE international symposium on Microarchitecture*, page 2, 1999.

[4] Nicola Jones. How to stop data centres from gobbling up the world's electricity. *Nature*, 561(7722):163–167, 2018.

[5] Cisco annual internet report (2018–2023) white paper. `https://www.cisco.com/c/en/us/solutions/collateral/executive-perspectives/annual-internet-report/white-paper-c11-741490.html`. Accessed: 2022-03-06.

[6] Anders SG Andrae and Tomas Edler. On global electricity usage of communication technology: trends to 2030. 6(1):117–157, 2015.

[7] Data centres and data transmission networks. `https://www.iea.org/reports/data-centres-and-data-transmission-networks`. Accessed: 2022-03-06.

[8] K Vahaplar, AM Kalashnikova, AV Kimel, Denise Hinzke, Ulrich Nowak, R Chantrell, A Tsukamoto, A Itoh, A Kirilyuk, and Th Rasing. Ultrafast path for optical magnetization reversal via a strongly nonequilibrium state. *Physical review letters*, 103(11):117201, 2009.

[9] Mauro J Kobrinsky, Bruce A Block, Jun-Fei Zheng, Brandon C Barnett, Edris Mohammed, Miriam Reshotko, Frank Robertson, Scott List, Ian Young, and Kenneth Cadien. On-chip optical interconnects. *Intel Technology Journal*, 8(2), 2004.

[10] Alexey V Kimel and Mo Li. Writing magnetic memory with ultrashort light pulses. *Nature Reviews Materials*, 4(3):189–200, 2019.

[11] Maarten Beens, Mark LM Lalieu, Axel JM Deenen, Rembert A Duine, and Bert Koopmans. Comparing all-optical switching in synthetic-ferrimagnetic multilayers and alloys. *Physical Review B*, 100(22):220409, 2019.

[12] Dmytro Apalkov, Alexey Khvalkovskiy, Steven Watts, Vladimir Nikitin, Xueti Tang, Daniel Lottis, Kiseok Moon, Xiao Luo, Eugene Chen, Adrian Ong, Alexander Driskill-Smith, and Mohamad Krounbi. Spin-transfer torque magnetic random access memory (stt-mram). 9(2), 2013.

[13] Elena Y Vedmedenko, Roland Kenji Kawakami, Denis D Sheka, Pietro Gambardella, Andrei Kirilyuk, Atsufumi Hirohata, Christian Binek, Oksana Chubykalo-Fesenko, Stefano Sanvito, Brian J Kirby, et al. The 2020 magnetism roadmap. *Journal of Physics D: Applied Physics*, 53(45):453001, 2020.

[14] Ginés Lifante. *Integrated photonics: fundamentals*. John Wiley & Sons, 2003.

[15] Theodore H Maiman et al. Stimulated optical radiation in ruby. 1960.

[16] Stewart E Miller. Integrated optics: An introduction. *The Bell System Technical Journal*, 48(7):2059–2069, 1969.

[17] Joseph C Palais. *Fiber optic communications*. Prentice Hall Englewood Cliffs, 1988.

[18] Lars Thylén and Lech Wosinski. Integrated photonics in the 21st century. *Photonics Research*, 2(2):75–81, 2014.

[19] Kaylee D Hakkel, Maurangelo Petruzzella, Fang Ou, Anne van Klinken, Francesco Pagliano, Tianran Liu, Rene PJ van Veldhoven, and Andrea Fiore. Integrated near-infrared spectral sensing. *Nature Communications*, 13(1):1–8, 2022.

[20] Natnicha Koompai, Pichet Limsuwan, Xavier Le Roux, Laurent Vivien, Delphine Marris-Morini, and Papichaya Chaisakul. Theoretical investigation of silicon nitride

waveguides for optical gas sensors in agricultural applications (conference presentation). In *Integrated Photonics Platforms: Fundamental Research, Manufacturing and Applications*, volume 11364, page 113641S. International Society for Optics and Photonics, 2020.

[21] Christopher V Poulton, Ami Yaacobi, David B Cole, Matthew J Byrd, Manan Raval, Diedrik Vermeulen, and Michael R Watts. Coherent solid-state lidar with silicon photonic optical phased arrays. *Optics letters*, 42(20):4091–4094, 2017.

[22] George Simonis. Photonics in homeland and national security. In *Photonic Applications Systems Technologies Conference*, page PTuA2. Optical Society of America, 2004.

[23] Michael Krainak, Mark Stephen, Elisavet Troupaki, Sarah Tedder, Baraquiel Reyna, Jonathan Klamkin, Hongwei Zhao, Bowen Song, Joseph Fridlander, Minh Tran, et al. Integrated photonics for nasa applications. In *Components and Packaging for Laser Systems V*, volume 10899, pages 75–94. SPIE, 2019.

[24] Alberto Politi, Jonathan CF Matthews, Mark G Thompson, and Jeremy L O'Brien. Integrated quantum photonics. *IEEE Journal of Selected Topics in Quantum Electronics*, 15(6):1673–1684, 2009.

[25] Georgios Zervas, Hui Yuan, Arsalan Saljoghei, Qianqiao Chen, and Vaibhawa Mishra. Optically disaggregated data centers with minimal remote memory latency: technologies, architectures, and resource allocation. *Journal of Optical Communications and Networking*, 10(2):A270–A285, 2018.

[26] Weiming Yao. *Towards a high-capacity multi-channel transmitter in generic photonic integration technology*. PhD thesis, Technische Universiteit Eindhoven, 2017.

[27] Meint Smit, Xaveer Leijtens, EAJM Bente, JJGM Van der Tol, HPMM Ambrosius, David Robbins, Mike Wale, Norbert Grote, and Martin Schell. Generic foundry model for inp-based photonics. *IET optoelectronics*, 5(5):187–194, 2011.

[28] John E Bowers and Alan Y Liu. A comparison of four approaches to photonic integration. In *Optical Fiber Communication Conference*, pages M2B–4. Optical Society of America, 2017.

[29] D Liang and JE Bowers. Photonic integration: Si or inp substrates? *Electronics Letters*, 45(12):578–581, 2009.

[30] Meint Smit, Kevin Williams, and Jos Van Der Tol. Past, present, and future of inp-based photonic integration. *APL Photonics*, 4(5):050901, 2019.

[31] L Pavesi, F Piazza, A Rudra, JF Carlin, and M Ilegems. Temperature dependence of the inp band gap from a photoluminescence study. *Physical Review B*, 44(16):9052, 1991.

[32] Jos JGM van der Tol, Yuqing Jiao, Jorn P Van Engelen, Vadim Pogoretskiy, Amir Abbas Kashi, and Kevin Williams. Inp membrane on silicon (imos) photonics. *IEEE Journal of Quantum Electronics*, 56(1):1–7, 2019.

[33] Miquel Rudé, Josselin Pello, Robert E Simpson, Johann Osmond, Gunther Roelkens, Jos JGM van der Tol, and Valerio Pruneri. Optical switching at $1.55\ \mu$ m in silicon racetrack resonators using phase change materials. *Applied Physics Letters*, 103(14):141119, 2013.

[34] Jai Prakash, Achu Chandran, and Ashok M Biradar. Scientific developments of liquid crystal-based optical memory: a review. *Reports on Progress in Physics*, 80(1):016601, 2016.

[35] Kengo Nozaki, Takasumi Tanabe, Akihiko Shinya, Shinji Matsuo, Tomonari Sato, Hideaki Taniyama, and Masaya Notomi. Sub-femtojoule all-optical switching using a photonic-crystal nanocavity. *Nature Photonics*, 4(7):477–483, 2010.

[36] Ya-Fen Hsiao, Pin-Ju Tsai, Hung-Shiue Chen, Sheng-Xiang Lin, Chih-Chiao Hung, Chih-Hsi Lee, Yi-Hsin Chen, Yong-Fan Chen, Ite A. Yu, and Ying-Cheng Chen. Highly efficient coherent optical memory based on electromagnetically induced transparency. *Phys. Rev. Lett.*, 120:183602, May 2018.

[37] Bethanie JH Stadler and Tetsuya Mizumoto. Integrated magneto-optical materials and isolators: a review. *IEEE Photonics Journal*, 6(1):1–15, 2013.

[38] Horst Dötsch, Norbert Bahlmann, Oleksandr Zhuromskyy, Manfred Hammer, Ludger Wilkens, Reinald Gerhardt, Peter Hertel, and Anatoly F Popkov. Applications of magneto-optical waveguides in integrated optics. *JOSA B*, 22(1):240–253, 2005.

[39] DC Hutchings. Prospects for the implementation of magneto-optic elements in optoelectronic integrated circuits: a personal perspective. *Journal of Physics D: Applied Physics*, 36(18):2222, 2003.

[40] PK Tien, RJ Martin, R Wolfe, RC Le Craw, and SL Blank. Switching and modulation of light in magneto-optic waveguides of garnet films. *Applied Physics Letters*, 21(8):394–396, 1972.

[41] Youri van Hees. *Magnetic claddings for photonic integrated circuits*. PhD thesis, Master's thesis, Eindhoven University of Technology, 2018.

[42] Anatoliĭ Konstantinovich Zvezdin and Viacheslav Alekseevich Kotov. *Modern magnetooptics and magnetooptical materials*. CRC Press, 1997.

[43] Y Shoji, K Miura, and T Mizumoto. Optical nonreciprocal devices based on magneto-optical phase shift in silicon photonics. *Journal of Optics*, 18(1):013001, 2015.

[44] Mehmet Cengiz Onbaşlı, Taichi Goto, Dong Hun Kim, Lei Bi, and CA Ross. Integration of magneto-optical cerium-doped yig on silicon nitride films for nonreciprocal photonic devices. In *Frontiers in Optics*, pages FTu1A–4. Optical Society of America, 2012.

[45] M Levy, RM Osgood Jr, R Liu, LE Cross, GS Cargill Iii, A Kumar, and H Bakhru. Fabrication of single-crystal lithium niobate films by crystal ion slicing. *Applied Physics Letters*, 73(16):2293–2295, 1998.

[46] Hideki Yokoi, Takashi Waniishi, Tetsuya Mizumoto, Masafumi Shimizu, Kazumasa Sakurai, Naoki Futakuchi, and Yoshiaki Nakano. Integration of terraced laser diode and garnet crystals by wafer direct bonding. *Japanese Journal of Applied Physics*, 40(5R):3463, 2001.

[47] Rui Ma, Sander Reniers, Yuya Shoji, Tetsuya Mizumoto, Kevin Williams, Yuqing Jiao, and Jos van der Tol. Integrated polarization-independent optical isolators and circulators on an inp membrane on silicon platform. *Optica*, 8(12):1654–1661, 2021.

[48] Mathias Vanwolleghem. *An integrated InP-based Optical Waveguide Isolator Using Ferromagnetic CoFe Contacts*. PhD thesis, Ghent University, 2005.

[49] Figen Ece Demirer, Chris van den Bomen, Reinoud Lavrijsen, Jos JGM van der Tol, and Bert Koopmans. Design and modelling of a novel integrated photonic device for nano-scale magnetic memory reading. *Applied Sciences*, 10(22):8267, 2020.

[50] Mario Reis. *Fundamentals of magnetism*. Elsevier, 2013.

[51] Joachim Stöhr and Hans Christoph Siegmann. Magnetism. *Solid-State Sciences. Springer, Berlin, Heidelberg*, 5:236, 2006.

[52] Ricardo C Sousa and I Lucian Prejbeanu. Non-volatile magnetic random access memories (mram). *Comptes Rendus Physique*, 6(9):1013–1021, 2005.

[53] JT Chang, JF Dillon Jr, and UF Gianola. Magneto-optical variable memory based upon the properties of a transparent ferrimagnetic garnet at its compensation temperature. *Journal of Applied Physics*, 36(3):1110–1111, 1965.

[54] Mario Norberto Baibich, Jean Marc Broto, Albert Fert, F Nguyen Van Dau, Frédéric Petroff, P Etienne, G Creuzet, A Friederich, and J Chazelas. Giant magnetoresistance of (001) fe/(001) cr magnetic superlattices. *Physical review letters*, 61(21):2472, 1988.

[55] Grünberg Binasch, Peter Grünberg, F Saurenbach, and W Zinn. Enhanced magnetoresistance in layered magnetic structures with antiferromagnetic interlayer exchange. *Physical review B*, 39(7):4828, 1989.

[56] W. J. Gallagher and S. S. P. Parkin. Development of the magnetic tunnel junction mram at ibm: From first junctions to a 16-mb mram demonstrator chip. *IBM Journal of Research and Development*, 50(1):5–23, 2006.

[57] Stuart S. P. Parkin, Masamitsu Hayashi, and Luc Thomas. Magnetic Domain-Wall Racetrack Memory. *Science*, 320(5873):190–194, 2008.

[58] Satoru Emori, Uwe Bauer, Sung-Min Ahn, Eduardo Martinez, and Geoffrey SD Beach. Current-driven dynamics of chiral ferromagnetic domain walls. *Nature materials*, 12(7):611–616, 2013.

[59] Kwang-Su Ryu, Luc Thomas, See-Hun Yang, and Stuart Parkin. Chiral spin torque at magnetic domain walls. *Nature nanotechnology*, 8(7):527–533, 2013.

[60] David Osuna Ruiz, O Alejos, Víctor Raposo, and Eduardo Martínez. Current-driven domain wall motion in curved ferrimagnetic strips above and below the angular momentum compensation. *Frontiers in Physics*, page 701, 2021.

[61] David Andrew Roberts. *Efficient Data Center Architectures Using Non-Volatile Memory and Reliability Techniques*. PhD thesis, University of Michigan, 2011.

[62] J Backus. Can functional programming be liberated from the von neumann style. *Communications of the ACM*, 21(8):613–641, 1978.

[63] Intel silicon photonics, moving data with light. `https://www.intel.com/content/www/us/en/architecture-and-technology/silicon-photonics/silicon-photonics-overview.html`. Accessed: 2022-03-06.

[64] Michael Faraday. I. experimental researches in electricity.—nineteenth series. *Philosophical Transactions of the Royal Society of London*, (136):1–20, 1846.

[65] J Clerk Maxwell. On faraday's lines of force. *Transactions of the Cambridge Philosophical Society*, 10:27, 1864.

[66] John Kerr. Xliii. on rotation of the plane of polarization by reflection from the pole of a magnet. *The London, Edinburgh, and Dublin Philosophical Magazine and Journal of Science*, 3(19):321–343, 1877.

[67] A Cotton and H Mouton. Sur les propriétés magnétooptiques des colloides et des liqueurs hétérogenes. *Ann Chim Phys*, 11:145–203, 1907.

[68] W Voigt. Handbuch der elektrizität und des magnetismus, 1920.

[69] HR Hulme. The faraday effect in ferromagnetics. *Proceedings of the Royal Society of London. Series A, Containing Papers of a Mathematical and Physical Character*, 135(826):237–257, 1932.

[70] Petros N Argyres. Theory of the faraday and kerr effects in ferromagnetics. *Physical Review*, 97(2):334, 1955.

[71] KP Belov and AV Pedko. On magnetostriction of gadolinium iron garnets. *Journal of Applied Physics*, 31(5):S55–S57, 1960.

[72] Robert P Hunt. Magneto-optic scattering from thin solid films. *Journal of Applied Physics*, 38(4):1652–1671, 1967.

[73] D Weller, H Brändle, G Gorman, C-J Lin, and H Notarys. Magnetic and magneto-optical properties of cobalt-platinum alloys with perpendicular magnetic anisotropy. *Applied physics letters*, 61(22):2726–2728, 1992.

[74] BM Holmes and DC Hutchings. Demonstration of quasi-phase-matched nonreciprocal polarization rotation in iii-v semiconductor waveguides incorporating magneto-optic upper claddings. *Applied physics letters*, 88(6):061116, 2006.

[75] Hidetoshi Iwamura, Shintaro Hayashi, and Hiroshi Iwasaki. A compact optical isolator using a y3fe5o12 crystal for near infra-red radiation. *Optical and Quantum Electronics*, 10(5):393–398, 1978.

[76] Yuya Shoji, Tetsuya Mizumoto, Hideki Yokoi, I-Wei Hsieh, and Richard M Osgood Jr. Magneto-optical isolator with silicon waveguides fabricated by direct bonding. *Applied physics letters*, 92(7):071117, 2008.

[77] Samir Ghosh, S Keyvavinia, W Van Roy, T Mizumoto, Günther Roelkens, and Roel Baets. Ce: Yig/silicon-on-insulator waveguide optical isolator realized by adhesive bonding. *Optics express*, 20(2):1839–1848, 2012.

[78] Chuck Young. Memory hierarchy. `https://seewhysite.wordpress.com/2019/08/21/memory-hierarchy/`, 2019.

[79] Prashanth Barla, Vinod Kumar Joshi, and Somashekara Bhat. Spintronic devices: a promising alternative to cmos devices. *Journal of Computational Electronics*, 20(2):805–837, 2021.

[80] Jorge Puebla, Junyeon Kim, Kouta Kondou, and Yoshichika Otani. Spintronic devices for energy-efficient data storage and energy harvesting. *Communications Materials*, 1(1):1–9, 2020.

[81] Zongxia Guo, Jialiang Yin, Yue Bai, Daoqian Zhu, Kewen Shi, Gefei Wang, Kaihua Cao, and Weisheng Zhao. Spintronics for energy-efficient computing: An overview and outlook. *Proceedings of the IEEE*, 2021.

[82] SA Wolf, DD Awschalom, RA Buhrman, JM Daughton, von S von Molnár, ML Roukes, A Yu Chtchelkanova, and DM Treger. Spintronics: a spin-based electronics vision for the future. *science*, 294(5546):1488–1495, 2001.

[83] Shinobu Fujita, Hiroki Noguchi, Kazutaka Ikegami, Susumu Takeda, Kumiko Nomura, and Keiko Abe. Novel memory hierarchy with e-stt-mram for near-future applications. In *2017 International Symposium on VLSI Technology, Systems and Application (VLSI-TSA)*, pages 1–2. IEEE, 2017.

[84] Debanjan Polley, Akshay Pattabi, Jyotirmoy Chatterjee, Sucheta Mondal, Kaushalya Jhuria, Hanuman Singh, Jon Gorchon, and Jeffrey Bokor. Progress toward picosecond on-chip magnetic memory. *Applied Physics Letters*, 120(14):140501, 2022.

[85] David J Smith, MR McCartney, CL Platt, and AE Berkowitz. Structural characterization of thin film ferromagnetic tunnel junctions. *Journal of applied physics*, 83(10):5154–5158, 1998.

[86] BN Engel, J Akerman, B Butcher, RW Dave, M DeHerrera, M Durlam, G Grynkewich, J Janesky, SV Pietambaram, ND Rizzo, et al. A 4-mb toggle mram based on a novel bit and switching method. *IEEE Transactions on Magnetics*, 41(1):132–136, 2005.

[87] S Bhatti and R Sbiaa. A. hirohat, h. ohno, s. fukami, sn piramanayagam1, spintronics based random access memory: a review. *Mater. Today*, 20:530, 2017.

[88] Atsufumi Hirohata, Keisuke Yamada, Yoshinobu Nakatani, Ioan-Lucian Prejbeanu, Bernard Diény, Philipp Pirro, and Burkard Hillebrands. Review on spintronics: Principles and device applications. *Journal of Magnetism and Magnetic Materials*, 509:166711, 2020.

[89] Qiming Shao, Peng Li, Luqiao Liu, Hyunsoo Yang, Shunsuke Fukami, Armin Razavi, Hao Wu, Frank Freimuth, Yuriy Mokrousov, Mark D Stiles, et al. Roadmap of spin-orbit torques. *IEEE Transactions on Magnetics*, 2021.

[90] Yevgen Pogoryelov, Manuel Pereiro, Somnath Jana, Ankit Kumar, Serkan Akansel, Mojtaba Ranjbar, Danny Thonig, Daniel Primetzhofer, Peter Svedlindh, Johan Åkerman, et al. Nonreciprocal spin pumping damping in asymmetric magnetic trilayers. *Physical Review B*, 101(5):054401, 2020.

[91] Aurelien Manchon, Hyun Cheol Koo, Junsaku Nitta, SM Frolov, and RA Duine. New perspectives for rashba spin–orbit coupling. *Nature materials*, 14(9):871–882, 2015.

[92] Ioan Mihai Miron, Kevin Garello, Gilles Gaudin, Pierre-Jean Zermatten, Marius V Costache, Stéphane Auffret, Sébastien Bandiera, Bernard Rodmacq, Alain Schuhl,

and Pietro Gambardella. Perpendicular switching of a single ferromagnetic layer induced by in-plane current injection. *Nature*, 476(7359):189–193, 2011.

[93] Kevin Garello, Can Onur Avci, Ioan Mihai Miron, Manuel Baumgartner, Abhijit Ghosh, Stéphane Auffret, Olivier Boulle, Gilles Gaudin, and Pietro Gambardella. Ultrafast magnetization switching by spin-orbit torques. *Applied Physics Letters*, 105(21):212402, 2014.

[94] ERJ Edwards, G Hu, SL Brown, CP D'Emic, MG Gottwald, P Hashemi, H Jung, J Kim, G Lauer, JJ Nowak, et al. Demonstration of narrow switching distributions in sttmram arrays for llc applications at 1x nm node. In *2020 IEEE International Electron Devices Meeting (IEDM)*, pages 24–4. IEEE, 2020.

[95] Kevin Garello, Farrukh Yasin, Hubert Hody, Sebastien Couet, Laurent Souriau, Shamin H Sharifi, Johan Swerts, Robert Carpenter, Siddharth Rao, Wonsub Kim, et al. Manufacturable 300mm platform solution for field-free switching sot-mram. In *2019 Symposium on VLSI Circuits*, pages T194–T195. IEEE, 2019.

[96] Sumio Ikegawa, Frederick B Mancoff, Jason Janesky, and Sanjeev Aggarwal. Magnetoresistive random access memory: Present and future. *IEEE Transactions on Electron Devices*, 67(4):1407–1419, 2020.

[97] Murat Cubukcu, Olivier Boulle, Nikolaï Mikuszeit, Claire Hamelin, Thomas Brächer, Nathalie Lamard, Marie-Claire Cyrille, Liliana Buda-Prejbeanu, Kevin Garello, Ioan Mihai Miron, et al. Ultra-fast perpendicular spin–orbit torque mram. *IEEE Transactions on Magnetics*, 54(4):1–4, 2018.

[98] Manuel Baumgartner, Kevin Garello, Johannes Mendil, Can Onur Avci, Eva Grimaldi, Christoph Murer, Junxiao Feng, Mihai Gabureac, Christian Stamm, Yves Acremann, et al. Spatially and time-resolved magnetization dynamics driven by spin–orbit torques. *Nature nanotechnology*, 12(10):980–986, 2017.

[99] Jungbum Yoon, Seo-Won Lee, Jae Hyun Kwon, Jong Min Lee, Jaesung Son, Xuepeng Qiu, Kyung-Jin Lee, and Hyunsoo Yang. Anomalous spin-orbit torque switching due to field-like torque–assisted domain wall reflection. *Science advances*, 3(4):e1603099, 2017.

[100] Kaushalya Jhuria, Julius Hohlfeld, Akshay Pattabi, Elodie Martin, Aldo Ygnacio Arriola Cordova, Xinping Shi, Roberto Lo Conte, Sébastien Petit-Watelot, Juan Carlos

Rojas-Sanchez, Grégory Malinowski, et al. Spin–orbit torque switching of a ferro-magnet with picosecond electrical pulses. *Nature Electronics*, 3(11):680–686, 2020.

[101] Amal El-Ghazaly, Jon Gorchon, Richard B Wilson, Akshay Pattabi, and Jeffrey Bokor. Progress towards ultrafast spintronics applications. *Journal of Magnetism and Magnetic Materials*, 502:166478, 2020.

[102] Paul M Haney, Hyun-Woo Lee, Kyung-Jin Lee, Aurélien Manchon, and Mark D Stiles. Current induced torques and interfacial spin-orbit coupling: Semiclassical modeling. *Physical Review B*, 87(17):174411, 2013.

[103] Eric Beaurepaire, J-C Merle, A Daunois, and J-Y Bigot. Ultrafast spin dynamics in ferromagnetic nickel. *Physical review letters*, 76(22):4250, 1996.

[104] Claudiu D Stanciu, Fredrik Hansteen, Alexey V Kimel, Andrei Kirilyuk, Arata Tsukamoto, Achioshi Itoh, and Th Rasing. All-optical magnetic recording with circularly polarized light. *Physical review letters*, 99(4):047601, 2007.

[105] LP Pitaevskii. Electric forces in a transparent dispersive medium. *Sov. Phys. JETP*, 12(5):1008–1013, 1961.

[106] JP Van der Ziel, Peter S Pershan, and LD Malmstrom. Optically-induced magnetization resulting from the inverse faraday effect. *Physical review letters*, 15(5):190, 1965.

[107] I Radu, K Vahaplar, C Stamm, T Kachel, N Pontius, HA Dürr, TA Ostler, J Barker, RFL Evans, RW Chantrell, et al. Transient ferromagnetic-like state mediating ultrafast reversal of antiferromagnetically coupled spins. *Nature*, 472(7342):205–208, 2011.

[108] TA Ostler, J Barker, RFL Evans, RW Chantrell, U Atxitia, O Chubykalo-Fesenko, S El Moussaoui, LBPJ Le Guyader, E Mengotti, LJ Heyderman, et al. Ultrafast heating as a sufficient stimulus for magnetization reversal in a ferrimagnet. *Nature communications*, 3(1):1–6, 2012.

[109] AR Khorsand, M Savoini, Andrei Kirilyuk, AV Kimel, A Tsukamoto, A Itoh, and Th Rasing. Role of magnetic circular dichroism in all-optical magnetic recording. *Physical review letters*, 108(12):127205, 2012.

[110] Hanna Becker, Clemens J Krückel, Dries Van Thourhout, and Martijn JR Heck. Out-of-plane focusing grating couplers for silicon photonics integration with optical mram technology. *IEEE Journal of Selected Topics in Quantum Electronics*, 26(2):1–8, 2019.

[111] Bert Koopmans. Ultrafast laser-induced magnetization dynamics. In *Laser Science*, page LSWJ2. Optical Society of America, 2009.

[112] A Eschenlohr. Spin dynamics at interfaces on femtosecond timescales. *Journal of Physics: Condensed Matter*, 33(1):013001, 2020.

[113] Elzbieta K Sobolewska, Johan Pelloux-Prayer, Hanna Becker, Guanqiao Li, Carl S Davies, CJ Krückel, L Avilés Félix, Aurélien Olivier, Ricardo C Sousa, Ioan-Lucian Prejbeanu, et al. Integration platform for optical switching of magnetic elements. In *Active Photonic Platforms XII*, volume 11461, page 114612B. International Society for Optics and Photonics, 2020.

[114] Spice project–developing future memory. `https://www.spice.uni-mainz.de/`. Accessed: 2022-02-09.

[115] JePPIX Roadmap 2021-2025. `http://www.jeppix.eu/2021/03/08/jeppix-roadmap-2021-2025`, 2021.

[116] Wim Bogaerts, Roel Baets, Pieter Dumon, Vincent Wiaux, Stephan Beckx, Dirk Taillaert, Bert Luyssaert, Joris Van Campenhout, Peter Bienstman, and Dries Van Thourhout. Nanophotonic waveguides in silicon-on-insulator fabricated with cmos technology. *Journal of Lightwave Technology*, 23(1):401–412, 2005.

[117] Guoliang Li, Jin Yao, Hiren Thacker, Attila Mekis, Xuezhe Zheng, Ivan Shubin, Ying Luo, Jin-Hyoung Lee, Kannan Raj, John E Cunningham, et al. Ultralow-loss, high-density soi optical waveguide routing for macrochip interconnects. *Optics express*, 20(11):12035–12039, 2012.

[118] Chao Xiang, Warren Jin, Duanni Huang, Minh Anh Tran, Joel Guo, Yating Wan, Weiqiang Xie, Geza Kurczveil, Andrew Netherton, Di Liang, et al. High-performance silicon photonics using heterogeneous integration. *IEEE Journal of Selected Topics in Quantum Electronics*, 2021.

[119] Paramjeet Kaur, Andreas Boes, Guanghui Ren, Thach G Nguyen, Gunther Roelkens, and Arnan Mitchell. Hybrid and heterogeneous photonic integration. *APL Photonics*, 6(6):061102, 2021.

[120] Hongtao Chen, Michael Galili, Peter Verheyen, Peter De Heyn, Guy Lepage, J De Coster, Sadhishkumar Balakrishnan, Philippe Absil, L Oxenlowe, Joris

Van Campenhout, et al. 100-gbps rz data reception in 67-ghz si-contacted germanium waveguide pin photodetectors. *Journal of Lightwave Technology*, 35(4):722–726, 2016.

[121] Srinivasan Ashwyn Srinivasan, Marianna Pantouvaki, Shashank Gupta, Hong Tao Chen, Peter Verheyen, Guy Lepage, Gunther Roelkens, Krishna Saraswat, Dries Van Thourhout, Philippe Absil, et al. 56 gb/s germanium waveguide electro-absorption modulator. *Journal of Lightwave Technology*, 34(2):419–424, 2016.

[122] Bertrand Szelag, Karim Hassan, Laetitia Adelmini, Elodie Ghegin, Philippe Rodriguez, Fabrice Nemouchi, Pierre Brianceau, Elisa Vermande, Antoine Schembri, David Carrara, et al. Hybrid iii–v/silicon technology for laser integration on a 200-mm fully cmos-compatible silicon photonics platform. *IEEE Journal of Selected Topics in Quantum Electronics*, 25(5):1–10, 2019.

[123] Jing Zhang, Bahawal Haq, James O'Callaghan, Angieska Gocalinska, Emanuele Pelucchi, António José Trindade, Brian Corbett, Geert Morthier, and Gunther Roelkens. Transfer-printing-based integration of a iii-v-on-silicon distributed feedback laser. *Optics express*, 26(7):8821–8830, 2018.

[124] Jing Zhang, Grigorij Muliuk, Joan Juvert, Sulakshna Kumari, Jeroen Goyvaerts, Bahawal Haq, Camiel Op de Beeck, Bart Kuyken, Geert Morthier, Dries Van Thourhout, et al. Iii-v-on-si photonic integrated circuits realized using micro-transfer-printing. *APL photonics*, 4(11):110803, 2019.

[125] Yuqing Jiao, Nobuhiko Nishiyama, Jos van der Tol, Jorn van Engelen, Vadim Pogoretskiy, Sander Reniers, Amir Abbas Kashi, Yi Wang, Victor Dolores Calzadilla, Marc Spiegelberg, et al. Inp membrane integrated photonics research. *Semiconductor Science and Technology*, 36(1):013001, 2020.

[126] Yuqing Jiao, Jos van der Tol, Vadim Pogoretskii, Jorn van Engelen, Amir Abbas Kashi, Sander Reniers, Yi Wang, Xinran Zhao, Weiming Yao, Tianran Liu, et al. Indium phosphide membrane nanophotonic integrated circuits on silicon. *physica status solidi (a)*, 217(3):1900606, 2020.

[127] Yuqing Jiao, Josselin Pello, Alonso Millan Mejia, Longfei Shen, Barry Smalbrugge, Erik Jan Geluk, Meint Smit, and Jos van der Tol. Fullerene-assisted electron-beam

lithography for pattern improvement and loss reduction in inp membrane waveguide devices. *Optics letters*, 39(6):1645–1648, 2014.

[128] Jieun Lee, Yasuna Maeda, Yuki Atsumi, Yuta Takino, Nobuhiko Nishiyama, and Sigehisa Arai. Low-loss gainasp wire waveguide on si substrate with benzocyclobutene adhesive wafer bonding for membrane photonic circuits. *Japanese Journal of Applied Physics*, 51(4R):042201, 2012.

[129] Utsav D Dave, Bart Kuyken, François Leo, Simon-Pierre Gorza, Sylvain Combrie, Alfredo De Rossi, Fabrice Raineri, and Gunther Roelkens. Nonlinear properties of dispersion engineered ingap photonic wire waveguides in the telecommunication wavelength range. *Optics express*, 23(4):4650–4657, 2015.

[130] Jorn van Engelen, Sander Reniers, Jeroen Bolk, Kevin Williams, Jos van der Tol, and Yuqing Jiao. Low loss inp membrane photonic integrated circuits enabled by 193-nm deep uv lithography. In *2019 Compound Semiconductor Week (CSW)*, pages 1–2. IEEE, 2019.

[131] Abdul Rahim, Eva Ryckeboer, Ananth Z Subramanian, Stéphane Clemmen, Bart Kuyken, Ashim Dhakal, Ali Raza, Artur Hermans, Muhammad Muneeb, Sören Dhoore, et al. Expanding the silicon photonics portfolio with silicon nitride photonic integrated circuits. *Journal of lightwave technology*, 35(4):639–649, 2017.

[132] Yuqing Jiao, Tjibbe de Vries, Ralph-Stephan Unger, Longfei Shen, Huub Ambrosius, Calin Radu, Michael Arens, Meint Smit, and Jos van der Tol. Vertical and smooth single-step reactive ion etching process for inp membrane waveguides. *Journal of The Electrochemical Society*, 162(8):E90, 2015.

[133] Emil Kleijn, Daniele Melati, Andrea Melloni, Tjibbe de Vries, Meint K Smit, and Xaveer JM Leijtens. Multimode interference couplers with reduced parasitic reflections. *IEEE Photonics Technology Letters*, 26(4):408–410, 2013.

[134] AJ Millan-Mejia, J vd Tol, and M Smit. 1× 2 multimode interference coupler with ultra-low reflections in membrane photonic integrated circuits. In *19th European Conf. on Integrated Optics (ECIO 2017)*, 2017.

[135] Frederik Van Laere, Tom Claes, Jonathan Schrauwen, Stijn Scheerlinck, Wim Bogaerts, Dirk Taillaert, Liam O'Faolain, Dries Van Thourhout, and Roel Baets. Compact

focusing grating couplers for silicon-on-insulator integrated circuits. *IEEE Photonics Technology Letters*, 19(23):1919–1921, 2007.

[136] Li He, Yang Liu, Christophe Galland, Andy Eu-Jin Lim, Guo-Qiang Lo, Tom Baehr-Jones, and Michael Hochberg. A high-efficiency nonuniform grating coupler realized with 248-nm optical lithography. *IEEE Photonics Technology Letters*, 25(14):1358–1361, 2013.

[137] Uzma Khalique. Polarization based integration scheme (polis). 2008.

[138] LM Augustin, R Hanfoug, JJGM Van der Tol, WJM De Laat, and MK Smit. A compact integrated polarization splitter/converter in ingaasp–inp. *IEEE Photonics Technology Letters*, 19(17):1286–1288, 2007.

[139] Abdulaziz E Elfiqi, Ryota Tanomura, Dawei Yu, Warakorn Yanwachirakul, Haifeng Shao, Yuto Suzuki, Takuo Tanemura, and Yoshiaki Nakano. Robust inp/ingaasp polarization rotator based on mode evolution. *IEEE Photonics Technology Letters*, 2022.

[140] Josselin Pello, Jos van der Tol, Shahram Keyvaninia, René van Veldhoven, Huub Ambrosius, Gunther Roelkens, and Meint Smit. High-efficiency ultrasmall polarization converter in inp membrane. *Optics letters*, 37(17):3711–3713, 2012.

[141] Sander Reniers. *Integration of a polarization converter on the active-passive IMOS platform*. PhD thesis, Eindhoven University of Technology, 2022.

[142] IBM. In-memory Computing. `https://www.ibm.com/blogs/research/tag/in-memory-computing/`, 2022.

[143] Carlos Ríos, Nathan Youngblood, Zengguang Cheng, Manuel Le Gallo, Wolfram HP Pernice, C David Wright, Abu Sebastian, and Harish Bhaskaran. In-memory computing on a photonic platform. *Science advances*, 5(2):eaau5759, 2019.

[144] Mark Lalieu. Next generation photonic memory devices are 'light-written', ultrafast and energy efficient. `https://www.tue.nl/en/news-and-events/news-overview/10-01-2019-next-generation-photonic-memory-devices-are-light-written-ultraf` 2019.

[145] AJ Poustie, KJ Blow, and RJ Manning. All-optical regenerative memory for long term data storage. *Optics communications*, 140(4-6):184–186, 1997.

[146] AJ Poustie, AE Kelly, RJ Manning, and KJ Blow. All-optical regenerative memory with full write/read capability. *Optics communications*, 154(5-6):277–281, 1998.

[147] Takasumi Tanabe, Masaya Notomi, Satoshi Mitsugi, Akihiko Shinya, and Eiichi Ku-ramochi. Fast bistable all-optical switch and memory on a silicon photonic crystal on-chip. *Optics letters*, 30(19):2575–2577, 2005.

[148] Kengo Nozaki, Akihiko Shinya, Shinji Matsuo, Yasumasa Suzaki, Toru Segawa, Tomonari Sato, Yoshihiro Kawaguchi, Ryo Takahashi, and Masaya Notomi. Ultralow-power all-optical ram based on nanocavities. *Nature Photonics*, 6(4):248–252, 2012.

[149] Alireza Geravand, Mohammad Danaie, and Saeed Mohammadi. All-optical photonic crystal memory cells based on cavities with a dual-argument hysteresis feature. *Optics Communications*, 430:323–335, 2019.

[150] Liu Liu, Rajesh Kumar, Koen Huybrechts, Thijs Spuesens, Günther Roelkens, Erik-Jan Geluk, Tjibbe De Vries, Philippe Regreny, Dries Van Thourhout, Roel Baets, et al. An ultra-small, low-power, all-optical flip-flop memory on a silicon chip. *Nature Photonics*, 4(3):182–187, 2010.

[151] Chin-Hui Chen, Shinji Matsuo, Kengo Nozaki, Akihiko Shinya, Tomonari Sato, Yoshi-hiro Kawaguchi, Hisashi Sumikura, and Masaya Notomi. All-optical memory based on injection-locking bistability in photonic crystal lasers. *Optics Express*, 19(4):3387–3395, 2011.

[152] Martin T Hill, Harmen JS Dorren, Tjibbe De Vries, Xaveer JM Leijtens, Jan Hendrik Den Besten, Barry Smalbrugge, Yok-Siang Oei, Hans Binsma, Giok-Djan Khoe, and Meint K Smit. A fast low-power optical memory based on coupled micro-ring lasers. *nature*, 432(7014):206–209, 2004.

[153] S Osborne, K Buckley, A Amann, and S O'Brien. All-optical memory based on the injection locking bistability of a two-color laser diode. *Optics express*, 17(8):6293–6300, 2009.

[154] Jun Sakaguchi, Takeo Katayama, and Hitoshi Kawaguchi. All-optical memory operation of 980-nm polarization bistable vcsel for 20-gb/s prbs rz and 40-gb/s nrz data signals. *Optics Express*, 18(12):12362–12370, 2010.

[155] Alexandros Emboras, Ilya Goykhman, Boris Desiatov, Noa Mazurski, Liron Stern, Joseph Shappir, and Uriel Levy. Nanoscale plasmonic memristor with optical readout functionality. *Nano letters*, 13(12):6151–6155, 2013.

[156] Meir Grajower, Noa Mazurski, Joseph Shappir, and Uriel Levy. Non-volatile silicon photonics using nanoscale flash memory technology. *Laser & Photonics Reviews*, 12(4):1700190, 2018.

[157] Matthias Wuttig and Noboru Yamada. Phase-change materials for rewriteable data storage. *Nature materials*, 6(11):824–832, 2007.

[158] VG Karpov, YA Kryukov, IV Karpov, and M Mitra. Field-induced nucleation in phase change memory. *Physical Review B*, 78(5):052201, 2008.

[159] P Fons, H Osawa, AV Kolobov, T Fukaya, M Suzuki, T Uruga, N Kawamura, H Tanida, and J Tominaga. Photoassisted amorphization of the phase-change memory alloy ge 2 sb 2 te 5. *Physical Review B*, 82(4):041203, 2010.

[160] Kotaro Makino, Junji Tominaga, and Muneaki Hase. Ultrafast optical manipulation of atomic arrangements in chalcogenide alloy memory materials. *Optics express*, 19(2):1260–1270, 2011.

[161] AV Kolobov, M Krbal, P Fons, J Tominaga, and T Uruga. Distortion-triggered loss of long-range order in solids with bonding energy hierarchy. *Nature chemistry*, 3(4):311–316, 2011.

[162] Robert E Simpson, Paul Fons, Alexander V Kolobov, Toshio Fukaya, Miloš Krbal, Takanori Yagi, and Junji Tominaga. Interfacial phase-change memory. *Nature nanotechnology*, 6(8):501–505, 2011.

[163] Jianmin Wang, Lei Wang, and Jun Liu. Overview of phase-change materials based photonic devices. *IEEE Access*, 8:121211–121245, 2020.

[164] Karthik Srinivasan and Bethanie JH Stadler. Magneto-optical materials and designs for integrated te-and tm-mode planar waveguide isolators: a review. *Optical Materials Express*, 8(11):3307–3318, 2018.

[165] W Van Parys, Dries Van Thourhout, Roel Baets, B Dagens, J Decobert, O Le Gouezigou, D Make, Reinier Vanheertum, and Liesbet Lagae. Low-loss,

inp-based integrated optical isolators. In *2008 Conference on Lasers and Electro-Optics and 2008 Conference on Quantum Electronics and Laser Science*, pages 1–2. IEEE, 2008.

[166] Hao Tian, Junqiu Liu, Anat Siddharth, Rui Ning Wang, Terence Blésin, Jijun He, Tobias J Kippenberg, and Sunil A Bhave. Magnetic-free silicon nitride integrated optical isolator. *Nature Photonics*, 15(11):828–836, 2021.

[167] Leonardo Del Bino, Jonathan M Silver, Michael TM Woodley, Sarah L Stebbings, Xin Zhao, and Pascal Del'Haye. Microresonator isolators and circulators based on the intrinsic nonreciprocity of the kerr effect. *Optica*, 5(3):279–282, 2018.

[168] Soonwook Kim, Donggyu B Sohn, Christopher W Peterson, and Gaurav Bahl. On-chip optical non-reciprocity through a synthetic hall effect for photons. *APL Photonics*, 6(1):011301, 2021.

[169] PM Oppeneer, T Maurer, J Sticht, and J Kübler. Ab initio calculated magneto-optical kerr effect of ferromagnetic metals: Fe and ni. *Physical Review B*, 45(19):10924, 1992.

[170] Alberto P Guimarães and Alberto Passos Guimaraes. *Principles of nanomagnetism*, volume 7. Springer, 2009.

[171] Baldassare Di Bartolo and RH Silsbee. Optical interactions in solids. *Am. J. Phys*, 37:756–757, 1969.

[172] Hans Kuzmany. *Solid-state spectroscopy: an introduction*. Springer, 2009.

[173] Paulo Vavassori. Magneto-optics lecture notes European School of Magnetism. `http://magnetism.eu/esm/2018/slides/vavassori-slides2.pdf`, 2018.

[174] Adrianus Johannes Schellekens. *Manipulating spins*. PhD thesis, Eindhoven University of Technology, 2014.

[175] Ml Freiser. A survey of magnetooptic effects. *IEEE Transactions on magnetics*, 4(2):152–161, 1968.

[176] R Clark Jones. A new calculus for the treatment of optical systemsv. a more general formulation, and description of another calculus. *JOSA*, 37(2):107–110, 1947.

[177] MLM Lalieu. *Femtomagnetism meets spintronics and magnonics*. PhD thesis, Technische Universiteit Eindhoven, 2019.

[178] Pavel Kabos, Anthony B Kos, and Thomas J Silva. Vectorial second-harmonic magneto-optic kerr effect measurements. *Journal of Applied Physics*, 87(9):5980–5982, 2000.

[179] Fabrication and characterization of magnetic nano-structures by paolo vavassori. https://www.ikerbasque.net/en/paolo-vavassori. Accessed: 2022-02-09.

[180] Richard M Rowan-Robinson, AA Stashkevich, Y Roussigné, M Belmeguenai, S-M Chérif, A Thiaville, TPA Hase, AT Hindmarch, and D Atkinson. The interfacial nature of proximity-induced magnetism and the dzyaloshinskii-moriya interaction at the pt/co interface. *Scientific reports*, 7(1):1–11, 2017.

[181] O Inyang, L Bouchenoire, B Nicholson, M Tokaç, RM Rowan-Robinson, CJ Kinane, and AT Hindmarch. Threshold interface magnetization required to induce magnetic proximity effect. *Physical Review B*, 100(17):174418, 2019.

[182] J Zak, ER Moog, C Liu, and SD Bader. Universal approach to magneto-optics. *Journal of Magnetism and Magnetic Materials*, 89(1-2):107–123, 1990.

[183] Ansys lumerical simulation software for photonics. https://www.ansys.com/products/photonics/fdtd. Accessed: 2022-02-09.

[184] Finite difference time domain simulations. https://www.synopsys.com/glossary/what-is-fdtd.html. Accessed: 2022-02-09.

[185] Lumerical software mode expansion monitors. https://support.lumerical.com/hc/en-us/articles/360034902433-Using-and-understanding-Mode-Expansion-Monitors. Accessed: 2022-02-09.

[186] Lumerical software fde solver. https://support.lumerical.com/hc/en-us/articles/360034917233-MODE-Finite-Difference-Eigenmode-FDE-solver-introducti Accessed: 2022-02-09.

[187] Creating anisotropic optical materials in lumerical software. https://support.lumerical.com/hc/en-us/articles/360034394694-Creating-anisotropic-optical-materials-in-FDTD-and-MODE. Accessed: 2022-02-09.

[188] Klayout software for mask design. `https://www.klayout.de`. Accessed: 2022-02-09.

[189] Nazca photonic ic design framework. `https://nazca-design.org/`. Accessed: 2022-02-09.

[190] Jos JGM van der Tol, Yuqing Jiao, Longfei Shen, Alonso Millan-Mejia, Vadim Pogoret-skii, Jorn P van Engelen, and Meint K Smit. Indium phosphide integrated photonics in membranes. *IEEE Journal of Selected Topics in Quantum Electronics*, 24(1):1–9, 2017.

[191] Juriaan Lucassen, Casper F Schippers, Marcel A Verheijen, Patrizia Fritsch, Erik Jan Geluk, Beatriz Barcones, Rembert A Duine, Sabine Wurmehl, Henk JM Swagten, Bert Koopmans, et al. Extraction of dzyaloshinskii-moriya interaction from propagating spin waves. *Physical Review B*, 101(6):064432, 2020.

[192] Reinoud Lavrijsen, DMF Hartmann, Arno van den Brink, Yuxiang Yin, Beatriz Bar-cones, RA Duine, MA Verheijen, HJM Swagten, and Bert Koopmans. Asymmetric magnetic bubble expansion under in-plane field in pt/co/pt: Effect of interface engi-neering. *Physical review B*, 91(10):104414, 2015.

[193] Sander FG Reniers, Kevin A Williams, Jos JGM van der Tol, and Yuqing Jiao. An accu-rate characterization method for integrated polarization converters. *IEEE Journal of Quantum Electronics*, 57(1):1–6, 2020.

[194] Yngwie Baron. *An integrated magneto-photonic device for magnetic memory reading*. PhD thesis, Master's thesis, Eindhoven University of Technology, 2022.

[195] Figen Ece Demirer, Reinoud Lavrijsen, and Bert Koopmans. An investigation of the interface and bulk contributions to the magneto-optic activity in co/pt multi-layered thin films. *Journal of Applied Physics*, 129(16):163904, 2021.

[196] Jairo Sinova, Dimitrie Culcer, Qian Niu, NA Sinitsyn, T Jungwirth, and Allan H Mac-Donald. Universal intrinsic spin hall effect. *Physical review letters*, 92(12):126603, 2004.

[197] Jairo Sinova, Sergio O Valenzuela, J Wunderlich, CH Back, and T Jungwirth. Spin hall effects. *Reviews of Modern Physics*, 87(4):1213, 2015.

[198] Andrew D. Kent and Daniel C. Worledge. A new spin on magnetic memories. *Nature Nanotechnology*, 10(3):187–191, 2015.

[199] M. L.M. Lalieu, R. Lavrijsen, and B. Koopmans. Integrating all-optical switching with spintronics. *Nature Communications*, 10(1):1–6, 2019.

[200] S. Mangin, D. Ravelosona, J. A. Katine, M. J. Carey, B. D. Terris, and Eric E. Fullerton. Current-induced magnetization reversal in nanopillars with perpendicular anisotropy. *Nature Materials*, 5(3):210–215, 2006.

[201] Frances Hellman, Axel Hoffmann, Yaroslav Tserkovnyak, Geoffrey SD Beach, Eric E Fullerton, Chris Leighton, Allan H MacDonald, Daniel C Ralph, Dario A Arena, Hermann A Dürr, et al. Interface-induced phenomena in magnetism. *Reviews of modern physics*, 89(2):025006, 2017.

[202] Dmytro Apalkov, Alexey Khvalkovskiy, Steven Watts, Vladimir Nikitin, Xueti Tang, Daniel Lottis, Kiseok Moon, Xiao Luo, Eugene Chen, Adrian Ong, et al. Spin-transfer torque magnetic random access memory (stt-mram). *ACM Journal on Emerging Technologies in Computing Systems (JETC)*, 9(2):1–35, 2013.

[203] E. Lišková, M. Veis, Š Višňovský, J. Ferré, A. Mougin, P. Mazalski, A. Maziewski, M. O. Liedke, and J. Fassbender. Effect of Ga + irradiation on the magneto-optic spectra of Pt/Co/Pt sandwiches. *Thin Solid Films*, 520(24):7169–7172, 2012.

[204] Ramon Weber, Carmen Martín Valderrama, Lorenzo Fallarino, and Andreas Berger. Dependence of the magneto-optical signal on the co layer thickness asymmetry in co/pt/co films. *Physical Review B*, 102(21):214434, 2020.

[205] R. Osgood, K. Riggs, Amy E. Johnson, J. Mattson, C. Sowers, and S. Bader. Magneto-optic constants of hcp and fcc Co films. *Physical Review B - Condensed Matter and Materials Physics*, 56(5):2627–2634, 1997.

[206] JA Arregi, JB González-Díaz, O Idigoras, and A Berger. Strain-induced magneto-optical anisotropy in epitaxial hcp co films. *Physical Review B*, 92(18):184405, 2015.

[207] Steffen Fiedler, Holger Stillrich, and Hans Peter Oepen. Magneto-optic properties of electron cyclotron resonance ion beam sputtered and magnetron sputtered Co/Pt multilayers. *Journal of Applied Physics*, 102(8), 2007.

[208] G. R. Harp, D. Weller, T. A. Rabedeau, R. F.C. Farrow, and M. F. Toney. Magneto-optical kerr spectroscopy of a new chemically ordered alloy: Co_3Pt. *Physical Review Letters*, 71(15):2493–2496, 1993.

[209] G S Krinchik and V A Artemjev. Magneto-optic Properties of Nickel, Iron, and Cobalt. 1276(1968), 2010.

[210] R. Atkinson, S. Pahirathan, I. W. Salter, P. J. Grundy, et al. Fundamental optical and magneto-optical constants of CoPt and CoNiPt multilayered films. *Journal of magnetism and magnetic materials*, 162(1):131–138, 1996.

[211] G. Didrichsen, W. R. Hendren, R. Atkinson, R. J. Pollard, and I. W. Salter. *Journal of Magnetism and Magnetic Materials*, 198:558–560, 1999.

[212] GA Prinz, JJ Krebs, DW Forester, and WG Maisch. Magneto-optical characterization of Fe and Co-based alloy films. *Journal of Magnetism and Magnetic Materials*, 15:779–781, 1980.

[213] M. R. Pufall and A. Berger. Studying the reversal mode of the magnetization vector versus applied field angle using generalized magneto-optical ellipsometry. *Journal of Applied Physics*, 87(9):5834–5836, 2000.

[214] H. Ouyang, Y. H. Han, S. C. Lo, C. H. Su, Y. R. Shiu, K. W. Lin, R. D. Desautels, and J. Van Lierop. Tailoring perpendicular magnetic anisotropy in ultrathin Co/Pt multi-layers coupled to nio. *Physical Review B - Condensed Matter and Materials Physics*, 81(22):1–7, 2010.

[215] D. C. Worledge, G. Hu, David W. Abraham, J. Z. Sun, P. L. Trouilloud, J. Nowak, S. Brown, M. C. Gaidis, E. J. O'Sullivan, and R. P. Robertazzi. Spin torque switching of perpendicular Ta|CoFeB|MgO-based magnetic tunnel junctions. *Applied Physics Letters*, 98(2):022501, 2011.

[216] G. A. Bertero and R. Sinclair. Structure-property correlations in Pt/Co multilayers for magneto-optic recording. *Journal of Magnetism and Magnetic Materials*, 134(1):173–184, 1994.

[217] Shouzhong Peng, Weisheng Zhao, Junfeng Qiao, Li Su, Jiaqi Zhou, Hongxin Yang, Qianfan Zhang, Youguang Zhang, Cecile Grezes, Pedram Khalili Amiri, and Kang L. Wang. Giant interfacial perpendicular magnetic anisotropy in MgO/CoFe/capping layer structures. *Applied Physics Letters*, 110(7), 2017.

[218] N Nakajima, T Koide, T Shidara, H Miyauchi, H Fukutani, A Fujimori, K Iio, T Katayama, M Nývlt, and Y Suzuki. Perpendicular magnetic anisotropy caused by

interfacial hybridization via enhanced orbital moment in Co/Pt multilayers: Magnetic circular x-ray dichroism study. *Physical Review Letters*, pages 1–4, 1998.

[219] R. M. Rowan-Robinson, A. A. Stashkevich, Y. Roussigné, M. Belmeguenai, S. M. Chérif, A. Thiaville, T. P.A. Hase, A. T. Hindmarch, and D. Atkinson. The interfacial nature of proximity-induced magnetism and the dzyaloshinskii-moriya interaction at the Pt/Co interface. *Scientific Reports*, 7(1):1–11, 2017.

[220] C. Clavero, L. Martínez, A. García-Martín, J. M. García-Martín, Y. Huttel, N. D. Telling, G. Van Der Laan, A. Cebollada, and G. Armelles. Morphology and capping effects in the magnetic and magneto-optical properties of nanoparticulate Co films. *Physical Review B - Condensed Matter and Materials Physics*, 77(9), 2008.

[221] W. L. Lim, N. Ebrahim-Zadeh, J. C. Owens, H. G.E. Hentschel, and S. Urazhdin. Temperature-dependent proximity magnetism in pt. *Applied Physics Letters*, 102(16), 2013.

[222] Thomas P.A. Hase, Matthew S. Brewer, Unnar B. Arnalds, Martina Ahlberg, Vassilios Kapaklis, Matts Björck, Laurence Bouchenoire, Paul Thompson, Daniel Haskel, Yongseong Choi, Jonathan Lang, Cecilia Sánchez-Hanke, and Björgvin Hjörvarsson. Proximity effects on dimensionality and magnetic ordering in pd/fe/pd trialyers. *Physical Review B - Condensed Matter and Materials Physics*, 90(10):1–6, 2014.

[223] Yuejie Zhang, Xiaofei Yang, Peng Li, and Mingzhong Wu. Strain engineering of magnetic proximity effect and spin-orbit torque in heavy metal/ferromagnet heterostructures. *Journal of Magnetism and Magnetic Materials*, 498(April 2019):166112, 2020.

[224] Yukai An, Lingshen Duan, Tao Liu, Zhonghuan Wu, and Jiwen Liu. Structural and magnetic properties of Pt in Co/Pt multilayers. *Applied Surface Science*, 257(17):7427–7431, 2011.

[225] I. Reichl, J. Zabloudil, R. Hammerling, A. Vernes, L. Szunyogh, and P. Weinberger. Magneto-optical kerr effect in perpendicularly magnetized (Co$_2$ Pt$_6$) in Pt (111) superstructures. *Physical Review B - Condensed Matter and Materials Physics*, 73(5):054402, 2006.

[226] F. Wilhelm, P. Poulopoulos, G. Ceballos, H. Wende, K. Baberschke, P. Srivastava, D. Benea, H. Ebert, M. Angelakeris, N. K. Flevaris, D. Niarchos, A. Rogalev, and N. B.

Brookes. Layer-resolved magnetic moments in Ni/Pt multilayers. *Physical Review Letters*, 85(2):413–416, 2000.

[227] J. Geissler, E. Goering, M. Justen, F. Weigand, G. Schütz, J. Langer, D. Schmitz, H. Maletta, and R. Mattheis. Pt magnetization profile in a Pt/Co bilayer studied by resonant magnetic x-ray reflectometry. *Physical Review B - Condensed Matter and Materials Physics*, 65(2):1–4, 2002.

[228] Ankan Mukhopadhyay, Sarathlal Koyiloth Vayalil, Dominik Graulich, Imran Ahamed, Sonia Francoual, Arti Kashyap, Timo Kuschel, and PS Anil Kumar. Asymmetric modification of the magnetic proximity effect in Pt/Co/Pt trilayers by the insertion of a Ta buffer layer. *Physical Review B*, 102(14):144435, 2020.

[229] T. Kuschel, C. Klewe, J. M. Schmalhorst, F. Bertram, O. Kuschel, T. Schemme, J. Wollschläger, S. Francoual, J. Strempfer, A. Gupta, M. Meinert, G. Götz, D. Meier, and G. Reiss. Static magnetic proximity effect in Pt/NiFe$_2$O$_4$ and Pt/Fe bilayers investigated by x-ray resonant magnetic reflectivity. *Physical Review Letters*, 115(9):097401, 2015.

[230] B. Rellinghaus, D. Weller, M. Q. Tran, and F. Hellman. Growth-induced magnetic anisotropy and clustering in vapor-deposited Co−Pt alloy films. *Physical Review B - Condensed Matter and Materials Physics*, 60(18):12826–12836, 1999.

[231] E. R. Moog, J. Zak, and S. D. Bader. *Journal of Applied Physics*, 69(2):880–885, 1991.

[232] C. Train, P. Beauvillain, V. Mathet, G. Pénissard, and P. Veillet. Spectroscopic polar magneto-optical kerr rotation on Co/Pt interface. *Journal of Applied Physics*, 86(6):3165–3170, 1999.

[233] Y. P. Lee, K. W. Kim, R. Gontarz, and V. Y. Kudryavtsev. Magneto-optical properties of spin-polarized Pt in Co/Pt multilayered films. *IEEE Transactions on Magnetics*, 35(5 PART 1):3088–3090, 1999.

[234] David R Lide. *CRC handbook of chemistry and physics: a ready-reference book of chemical and physical data*. CRC press, 1995.

[235] Juriaan Lucassen, Casper F. Schippers, Marcel A. Verheijen, Patrizia Fritsch, Erik Jan Geluk, Beatriz Barcones, Rembert A. Duine, Sabine Wurmehl, Henk J. M. Swagten,

Bert Koopmans, and Reinoud Lavrijsen. Extraction of dzyaloshinskii-moriya interaction from propagating spin waves. *Phys. Rev. B*, 101:064432, Feb 2020.

[236] E. Lundgren, B. Stanka, M. Schmid, and P. Varga. Thin films of Co on Pt(111): Strain relaxation and growth. *Phys. Rev. B*, 62:2843–2851, Jul 2000.

[237] W. Ranke, M. Ritter, and W. Weiss. Crystal structures and growth mechanism for ultrathin films of ionic compound materials: FeO(111) on Pt(111). *Phys. Rev. B*, 60:1527–1530, Jul 1999.

[238] J Goodmann, F Leonberger, and S Kung. R. athale optical interconnections for vlsi systems proc. *IEEE*, 72:850–866, 1984.

[239] Intel leverages chip might etch photonics future. `https://www.nextplatform.com/2016/08/17/intel-leverages-chip-might-etch-photonics-future/`. Accessed: 2020-11-11.

[240] Record breaking optical chip. `https://www.technologyreview.com/2008/06/25/`. Accessed: 2020-11-11.

[241] Fred Kish, Vikrant Lal, Peter Evans, Scott W Corzine, Mehrdad Ziari, Tim Butrie, Mike Reffle, Huan-Shang Tsai, Andrew Dentai, Jacco Pleumeekers, et al. System-on-chip photonic integrated circuits. *IEEE Journal of Selected Topics in Quantum Electronics*, 24(1):1–20, 2017.

[242] Chen Sun, Mark T Wade, Yunsup Lee, Jason S Orcutt, Luca Alloatti, Michael S Georgas, Andrew S Waterman, Jeffrey M Shainline, Rimas R Avizienis, Sen Lin, et al. Single-chip microprocessor that communicates directly using light. *Nature*, 528(7583):534–538, 2015.

[243] Amir H Atabaki, Sajjad Moazeni, Fabio Pavanello, Hayk Gevorgyan, Jelena Notaros, Luca Alloatti, Mark T Wade, Chen Sun, Seth A Kruger, Huaiyu Meng, et al. Integrating photonics with silicon nanoelectronics for the next generation of systems on a chip. *Nature*, 556(7701):349–354, 2018.

[244] MLM Lalieu, MJG Peeters, SRR Haenen, R Lavrijsen, and B Koopmans. Deterministic all-optical switching of synthetic ferrimagnets using single femtosecond laser pulses. *Physical review B*, 96(22):220411, 2017.

[245] YLW van Hees, JJGM van der Tol, B Koopmans, and R Lavrijsen. Periodically modulated ferromagnetic waveguide claddings with perpendicular magnetic anisotropy for enhanced mode conversion. *IEEE Photonics Proceedings*, 2017.

[246] Kwang-Su Ryu, Luc Thomas, See-Hun Yang, and Stuart SP Parkin. Current induced tilting of domain walls in high velocity motion along perpendicularly magnetized micron-sized co/ni/co racetracks. *Applied Physics Express*, 5(9):093006, 2012.

[247] See-Hun Yang, Kwang-Su Ryu, and Stuart Parkin. Domain-wall velocities of up to 750 m s- 1 driven by exchange-coupling torque in synthetic antiferromagnets. *Nature nanotechnology*, 10(3):221–226, 2015.

[248] Lucas Caretta, Maxwell Mann, Felix Büttner, Kohei Ueda, Bastian Pfau, Christian M Günther, Piet Hessing, Alexandra Churikova, Christopher Klose, Michael Schneider, et al. Fast current-driven domain walls and small skyrmions in a compensated ferrimagnet. *Nature nanotechnology*, 13(12):1154–1160, 2018.

[249] JH Franken, HJM Swagten, and Bert Koopmans. Shift registers based on magnetic domain wall ratchets with perpendicular anisotropy. *Nature nanotechnology*, 7(8):499–503, 2012.

[250] Mengxing Wang, Yue Zhang, Xiaoxuan Zhao, and Weisheng Zhao. Tunnel junction with perpendicular magnetic anisotropy: Status and challenges. *Micromachines*, 6(8):1023–1045, 2015.

[251] J. J. G. M. van der Tol, Y. Jiao, J. P. Van Engelen, V. Pogoretskiy, A. A. Kashi, and K. Williams. Inp membrane on silicon (imos) photonics. *IEEE Journal of Quantum Electronics*, 56(1):1–7, 2020.

[252] R. Lavrijsen, D. M. F. Hartmann, A. van den Brink, Y. Yin, B. Barcones, R. A. Duine, M. A. Verheijen, H. J. M. Swagten, and B. Koopmans. Asymmetric magnetic bubble expansion under in-plane field in pt/co/pt: Effect of interface engineering. *Phys. Rev. B*, 91:104414, Mar 2015.

[253] Štefan Višňovskỳ, Eva Jakubisová Lišková, Miroslav Nỳvlt, and Ramanathan Krishnan. Origin of magneto-optic enhancement in copt alloys and co/pt multilayers. *Applied Physics Letters*, 100(23):232409, 2012.

[254] Lumerical solutions. `https://www.lumerical.com/products/`. Accessed: 2020-10-29.

[255] Figen Ece Demirer, Yngwie Baron, Sander Reniers, Dzmitry Pustakhod, Reinoud Lavrijsen, Jos van der Tol, and Bert Koopmans. An integrated photonic device for on-chip magneto-optical memory reading. *Nanophotonics*, 2022.

[256] Ajay Joshi, Christopher Batten, Yong-Jin Kwon, Scott Beamer, Imran Shamim, Krste Asanovic, and Vladimir Stojanovic. Silicon-photonic clos networks for global on-chip communication. In *2009 3rd ACM/IEEE International Symposium on Networks-on-Chip*, pages 124–133. IEEE, 2009.

[257] George Kurian, Jason E Miller, James Psota, Jonathan Eastep, Jifeng Liu, Jurgen Michel, Lionel C Kimerling, and Anant Agarwal. Atac: A 1000-core cache-coherent processor with on-chip optical network. In *2010 19th International Conference on Parallel Architectures and Compilation Techniques (PACT)*, pages 477–488. IEEE, 2010.

[258] Scott Beamer, Chen Sun, Yong-Jin Kwon, Ajay Joshi, Christopher Batten, Vladimir Stojanović, and Krste Asanović. Re-architecting dram memory systems with monolithically integrated silicon photonics. *ACM SIGARCH Computer Architecture News*, 38(3):129–140, 2010.

[259] Ziyi Zhu, Giuseppe Di Guglielmo, Qixiang Cheng, Madeleine Glick, Jihye Kwon, Hang Guan, Luca P Carloni, and Keren Bergman. Photonic switched optically connected memory: An approach to address memory challenges in deep learning. *Journal of Lightwave Technology*, 38(10):2815–2825, 2020.

[260] Apostolos Tsakyridis, Theoni Alexoudi, Amalia Miliou, Nikos Pleros, and Christos Vagionas. 10 gb/s optical random access memory (ram) cell. *Optics letters*, 44(7):1821–1824, 2019.

[261] Xuan Li, Nathan Youngblood, Carlos Ríos, Zengguang Cheng, C David Wright, Wolfram HP Pernice, and Harish Bhaskaran. Fast and reliable storage using a 5 bit, non-volatile photonic memory cell. *Optica*, 6(1):1–6, 2019.

[262] Jun-Yang Chen, Li He, Jian-Ping Wang, and Mo Li. All-optical switching of magnetic tunnel junctions with single subpicosecond laser pulses. *Physical Review Applied*, 7(2):021001, 2017.

[263] L Avilés-Félix, Aurélien Olivier, Guanqiao Li, Carl S Davies, Laura Álvaro-Gómez, Miguel Rubio-Roy, Stéphane Auffret, Andrei Kirilyuk, AV Kimel, Th Rasing, et al. Single-shot all-optical switching of magnetization in tb/co multilayer-based electrodes. *Scientific reports*, 10(1):1–8, 2020.

[264] Luding Wang, Houyi Cheng, Pingzhi Li, Yang Liu, Youri LW van Hees, Reinoud Lavrijsen, Xiaoyang Lin, Kaihua Cao, Bert Koopmans, and Weisheng Zhao. Picosecond switching of optomagnetic tunnel junctions. *arXiv preprint arXiv:2011.03612*, 2020.

[265] Rachid Sbiaa, H Meng, and SN Piramanayagam. Materials with perpendicular magnetic anisotropy for magnetic random access memory. *physica status solidi (RRL)– Rapid Research Letters*, 5(12):413–419, 2011.

[266] Nicola A Spaldin. *Magnetic materials: fundamentals and applications*. Cambridge university press, 2010.

[267] RS Woodward. Poincaré's cours de physique mathématique: Théorie du potentiel newtonien. par h. poincaré. rédigées par édouard leroy et georges vincent. paris, georges carré et c. naud. 1899. 8vo. pp. 366.; cinématique et mécanismes, potentiel et mécanique des fluides. par h. poincaré. rédigé par a. guillet. paris, georges carré et c. naud. 1898. 8vo. pp. 385. *Science*, 10(242):213–217, 1899.

[268] George Gabriel Stokes. On the composition and resolution of streams of polarized light from different sources. *Transactions of the Cambridge Philosophical Society*, 9:399, 1851.

[269] Finite difference time domain simulations. `https://www.synopsys.com/glossary/what-is-fdtd.html`. Accessed: 2022-02-09.

[270] Sadao Adachi and Hitoshi Kawaguchi. Chemical etching characteristics of (001) inp. *Journal of The Electrochemical Society*, 128(6):1342, 1981.

[271] Wolfgang Kuch, Rudolf Schäfer, Peter Fischer, and Franz Ulrich Hillebrecht. *Magnetic microscopy of layered structures*. Springer, 2015.

[272] Stuart S. P. Parkin, Masamitsu Hayashi, and Luc Thomas. Magnetic domain-wall racetrack memory. *Science*, 320(5873):190–194, 2008.

[273] Sambit Ghosh, Taro Komori, Ali Hallal, Jose Pena Garcia, Toshiki Gushi, Taku Hirose, Haruka Mitarai, Hanako Okuno, Jan Vogel, Mairbek Chshiev, et al. Current-driven domain wall dynamics in ferrimagnetic nickel-doped mn4n films: Very large domain wall velocities and reversal of motion direction across the magnetic compensation point. *Nano Letters*, 21(6):2580–2587, 2021.

[274] Haechang Lee, Kun-Yung Ken Chang, Jung-Hoon Chun, Ting Wu, Yohan Frans, Brian Leibowitz, Nhat Nguyen, T. J. Chin, Kambiz Kaviani, Jie Shen, Xudong Shi, Wendemagegnehu T. Beyene, Simon Li, Reza Navid, Marko Aleksic, Fred S. Lee, Fredy Quan, Jared Zerbe, Rich Perego, and Fariborz Assaderaghi. A 16 gb/s/link, 64 gb/s bidirectional asymmetric memory interface. *IEEE Journal of Solid-State Circuits*, 44(4):1235–1247, 2009.

[275] Mihai Dragos Rotaru and Li Kangrong. Electrical design challenges in high bandwidth memory and advanced interface bus interfaces on hd-fowlp technology. In *2021 IEEE 71st Electronic Components and Technology Conference (ECTC)*, pages 334–339, 2021.

[276] Hamed Pezeshki et al. Optically reading and writing nanoscale magnetic bits in an integrated platform using magneto-plasmonic effects. *Under preparation*, –(-):–, -.

[277] Bhavin J Shastri, Alexander N Tait, Thomas Ferreira de Lima, Wolfram HP Pernice, Harish Bhaskaran, C David Wright, and Paul R Prucnal. Photonics for artificial intelligence and neuromorphic computing. *Nature Photonics*, 15(2):102–114, 2021.

[278] Pascal Stark, Folkert Horst, Roger Dangel, Jonas Weiss, and Bert Jan Offrein. Opportunities for integrated photonic neural networks. *Nanophotonics*, 9(13):4221–4232, 2020.

[279] Hailong Zhou, Jianji Dong, Junwei Cheng, Wenchan Dong, Chaoran Huang, Yichen Shen, Qiming Zhang, Min Gu, Chao Qian, Hongsheng Chen, et al. Photonic matrix multiplication lights up photonic accelerator and beyond. *Light: Science & Applications*, 11(1):1–21, 2022.

Publications

Demirer, F. E., van den Bomen, C., Lavrijsen, R., van der Tol, J. J., & Koopmans, B, Design and modelling of a novel integrated photonic device for nano-scale magnetic memory reading, Applied Sciences, 10(22), 8267 (2020).

Demirer, F. E., Lavrijsen, R., & Koopmans, B., An investigation of the interface and bulk contributions to the magneto-optic activity in Co/Pt multi-layered thin films, Journal of Applied Physics, 129(16), 163904 (2021).

Demirer, F. E., Baron, Y., Reniers, S., Pustakhod, D., Lavrijsen, R., van der Tol, J., & Koopmans, B., An integrated photonic device for on-chip magneto-optical memory reading, Nanophotonics, 11(14), 3319-3329 (2022).

Conference contribution

Demirer, F. E., Reniers, S., Lavrijsen, R., van der Tol, J., & Koopmans, B., Magneto-photonic on-chip device for all-optical reading of magnetic memory, Conference on Lasers and Electro-Optics Europe and European Quantum Electronics Conference (CLEO/Europe-EQEC). Institute of Electrical and Electronics Engineers, 1 p. 9541558 (2021)

Not included in this thesis

Pezeshki, H., Demirer, F. E. et al., Optically reading and writing nanoscale magnetic bits in an integrated platform using magneto-plasmonic effects, Under preparation

Acknowledgements

For a tree to grow, there needs to be an ecosystem. Here, I will do my best to honor all the contributors of the ecosystem that this work grew in.

Firstly, I would like to thank my supervisors. Bert Koopmans, thanks for being convinced that I would be a good candidate for this project! Throughout the years, this trust you granted me formed the base where I stand and shed light for the way forward. I am also thankful you are a patient and kind person. Dear Jos van der Tol, I had the honor to be one of your last students. Your sharp mind being on my side, I did not need to doubt about the direction. I also adored your approach to life with a cup of herbal tea and good humor.

I also express my gratitude to the committee members, prof.dr.ir. G.M.W. Kroesen, dr.ir. R. Lavrijsen, prof.dr. A. Fiore, prof.dr. A.I. Kirilyuk, prof.dr.ir. S. van Dijken, prof.dr. B. Dagens and dr. Y. Jiao. Special thanks to Andrea for his detailed review, to Yuqing for improvement suggestions and to Prof. Beatriz Dagens for her attention to details.

I always felt the advantages of being raised in Turkey. It gave me the grit and shaped by attitude towards life for being agile in thinking and acting. How lucky I was to have all those very good teachers, from very early on, till the later stages. I want to thank specifically to my chemistry teacher Dilek Hoca and my materials science professor Cleva Hoca. Strong characters these two ladies have, gave me the freedom to show mine.

Sevgili ailem, canim annem Arzu, babam Fuat ve kardesim Ege. Sizler gibi bir aileye sahip oldugum icin o kadar sansliyim ki! Annem, ozverili, kivrak zekali, sempatik ve is bitirici annem. Babam, butun evrenin gidisatini gormus ve dunyaya geri donmus kadar bilge ve sakin babam. Hep kendisi olan, akilli ve akli bir karis havada kardesim Ege. Sizin desteginizi hep arkamda hissettim. Bu yuzden buyuk ve korkutucu gorunen adimlari atmak benim icin hic de zor olmadi. Mesafeler uzak olsa da kalplerimiz hep yakin. Her gecen gun sizin ozelliklerinizi kendimde kesfetmek ne kadar guzel! Aklimda akliniz yazili. Iyi ki varsiniz.

I want to thank Karin, Gerrie and Bert for creating a family environment in FNA. And for all the technical support and gezellig coffee breaks, my thanks to Jeroen. The deepest conversations during tea breaks were made with Oleg, thanks for that. Special thanks to

Yngwie for being so bright and being on my team. In the category of office-mates we have two winners: Marcos for being a strong character with vocal and constructive attitude. A great out-loud thinker and influencer. Dear Marcos, I recall days I was high on caffeine while working and you made me jump out of my seat with sudden reactions in the middle of silence times, it makes me smile thinking of it. And Adrien, thanks for all good times and thanks for taking the title of the hot-blooded in the room from me with great meritocracy. Proceeding to others, Marielle, thanks for simply being yourself, being out there, and showing active and engaging attitude towards challenges. Also, thanks for showing how to think like a go-getter! Ani! Thanks for reminding me how a strong desire to succeed flows through our veins and become reality (after hours of hard work). Thanks to Tunc for the support and the good times. Thanks to Mark L. for being so understanding and caring, showing good leadership. Thanks to Fanny, Juriaan, Mark P., Casper, Tom, Youri, Maarten, Thomas, Luding, Michal, Jianing, Pingzhi and Hamed.

Thanks to the PhI group for being so welcoming and diverse, I felt like part of a family. Thank you Florian for simply being yourself, showing curiosity, reminding me there is so much to explore, try and play in life. Thank you Dima for radiating your talent out, supporting, teaching, being so strong. Thanks Vadim for simply being yourself, without excuses. Thanks to Jorn for being so kind and collaborative. Thanks to Sander for allowing me to unlock my dreams! Your talent and hard work in executing work inspired me. Thanks to all great people of PhI that I recall with a huge smile, Bary, Erik Jan, Jolande, Weiming, Rastko, Marija, Yuqing, Erwin, Amir, Ozan, Marc.

Thanks to my friends who keep my heart warm during the hardest times. Thanks Juanacim for designing the thesis cover with love. Thanks to all the Familyship. Especially the doctors who paved the way: my sister Ni, grit, humor, intelligence; my brother Matty, faith, hardwork and family; Ana, strength, determination and freedom! For Ewa for her wisdom and for Petra for her courage, smile and attitude.

Comes the part where I acknowledge my partner in life, Daniele. Who showed me there is hope, in me, in the world. Gave me strength to just keep on swimming. Best thing found on the campus of Eindhoven University. I feel grateful for the life events that made our paths cross one another. May our discussions about the nature and reality be going further on. Grazie mille per tutti!

Biography

Figen Ece Demirer was born in February 3rd, 1992 in Bartın, Turkiye. After finishing high school in 2010 at Adem Tolunay Anadolu Lisesi in Antalya (Turkiye), she studied Materials Science and Nanoengineering at the Sabancı University in Istanbul with an Excellence Scholarship. She obtained her Bachelor of Science degree in 2015, after completing the project "Luminescence Converters for Organic Solar Cells" under the supervision of dr. Cleva Ow-Yang. In addition to the major in materials science, she was awarded with the minor in chemistry.

Ece continued her studies at the University of Twente (the Netherlands) with the UTS scholarship and obtained her Master of Science degree in 2017. In her graduation project, she experimentally studied the Charge Transfer at Complex Oxide Interfaces in Inorganic Materials Science group, under the supervision of dr. Gertjan Koster.

After obtaining her Master's degree, Ece started with a PhD project in the group Physics of Nanostructures at the Eindhoven University of Technology, shifting her focus to implementation of magnetic memory components combined with integrated photonic applications. The main results of this PhD project are presented in this thesis.

Summary

 Detecting the magnetization direction of a medium by probing its interaction with light is at the base of this Thesis. Such a task holds great technological potential when the light is confined in a material. The research conducted during this project is performed at the fruitful interface of the two fields: nano-magnetism and integrated photonics. The project aims to provide a novel functionality to integrated photonic devices, namely a magneto-photonic device with functionality of all-optical reading of non-volatile magnetic memories. A huge potential is anticipated when using all-optical operations in applications where a frequent non-volatile memory retrieval is required, cutting down on intermediate electronics steps, saving time and energy. Findings shown in this Thesis pave the way towards integrated photonic devices for energy efficient data communication between the traditional non-volatile memory components and the optical communication channels.

The integrated magneto-photonic devices demonstrated in this Thesis are composed of photonic waveguides and built-in ferro-magnetic memories that are applied as top-claddings to certain regions of the waveguides. Polar Magneto-Optic Kerr Effect (MOKE) which occurs upon interaction of guided light and perpendicularly magnetized cladding is used to determine the magnetization direction, thus determine the memory state. For light confined in waveguides, polar MOKE manifests itself as a partial mode conversion between transverse-electric (TE) and transverse-magnetic (TM) modes, albeit with intrinsically small amplitudes. In this Thesis, the challenge of transforming this small effect into a useful signal is successfully demonstrated, providing the proof-of-principle for integrated optical magnetic memory reading. Additionally, multi-layered thin-film magnetic memory materials are studied to map the magneto-optical properties of the interface and bulk regions.

In Chapter 1, the concepts relevant to this project are introduced including the integrated photonics, spintronics and magneto-optics. Chapter 2 describes the state-of-the-art in spintronic memories and integrated photonics with a special focus on optical memories. An overview is presented after introducing the memory hierarchy in computers, placing the work into context.

In Chapter 3, the methodology of this work is presented, detailing experimental, analytical and fabrication aspects. Additionally, the design toolbox used for integrated photonics is introduced. In terms of sample fabrication, Indium phosphide Membrane On Silicon (IMOS) platform for integrated photonics and the magnetron sputtering for thin-film cladding realization are described. Lastly, the integrated optical set-up that is used to characterize the

magneto-photonic devices is introduced.

Chapter 4 is dedicated to the investigation of magneto-optical properties of the memory materials utilized in this work. These materials are multilayered thin-films made of Cobalt (Co) layers sandwiched between Platinum (Pt) layers and demonstrate perpendicular magnetic anisotropy (PMA). Studying sample sets with continuous thickness variations, enhancement of the magneto-optic activity at the Co/Pt interface is detected. Interpreting the experimental evidence using mathematical models, the bulk and interface magneto-optic Voigt constants are determined. At later stages of the project, these findings are then used as input for more complex optical simulations of the designed magneto-photonic devices using Finite Difference Time Domain (FDTD) method. Additionally, benefiting from the insights gained in this chapter, memory materials with higher magneto-optic efficiency are obtained while maintaining the PMA.

Chapter 5 presents the design and modelling of a magneto-photonic device that delivers non-volatile photonic memory functionality. The device is an unbalanced Mach-Zender interferometer and is designed to be sensitive to the changes in the light's polarization state. One arm of the interferometer carries the memory component (as cladding) while the other accommodates a delay line (additional waveguide length) and a polarization converter section. Thanks to its design, the device detects the intrinsically small MOKE, which occur after the light's interaction with the memory component, thus memory reading is realized. A high sensitivity in devices is ensured using a phase-sensitive Fourier transformation technique. Interference fringes that occur in the transmitted light intensity as a function of light's wavelength are interpreted in terms of their frequency and phase. When locked at a certain frequency, the phase of interference fringes yields information regarding the magnetization direction in claddings, thus enables reading of the photonic memory.

Chapter 6 presents the design, fabrication and experimental demonstration of a magneto-photonic device that delivers non-volatile photonic memory functionality. The design is based on an asymmetric cross-section waveguide (as polarization converter) connected to a thin-film (magnetic) cladded waveguide and delivers phase engineering. Both components manipulate the phase of light, albeit due to the MOKE, the latter does it in a non-reciprocal manner with respect to the magnetization direction of the memory component. As a result, the device encodes the memory information and yields different mode-specific transmissions depending on the memory state. Transmitted light versus applied magnetic field obtained from the devices show a typical hysteresis behavior of a ferromagnet. The resulting squared hysteresis loops provide direct evidence for magneto-optical memory reading,

which to our knowledge observed for the first time using an integrated photonic device and PMA memory components. We conjecture that when racetrack memory is implemented, the current 1% transmitted power contrast leads to the theoretical bandwidth of 50 Gbits/s memory read-out speed in a shot noise limited scenario. The last part of the chapter is dedicated to scientific and technological outlook of the presented work, stressing potential application areas.